Synthesis of Superconducting Nb_3Sn Thin Film Heterostructures for the Study of High-Energy RF Physics

By

Christopher S. Sundahl

A dissertation submitted in partial fulfillment of

the requirements for the degree of

Doctor of Philosophy

(Materials Science & Engineering)

at the

UNIVERSITY OF WISCONSIN – MADISON

2019

Date of final oral examination: 12/13/2018

The dissertation is approved by the following members of the Final Oral Committee:

Chang-Beom Eom, Professor, Materials Science & Engineering
Alexander V. Gurevich, Professor, Physics
Robert F. McDermott, Professor, Physics
Mark Rzchowski, Professor, Physics
Xudong Wang, Professor, Materials Science & Engineering

Abstract

Radio-frequency (RF) particle accelerator cavities are one of the industrial and research applications in which superconductivity, still an underexplored phenomenon, has been broadly adopted. Niobium (Nb) cavities are ubiquitous in accelerator facilities, and research to improve their reliability and quality are ongoing. However, Nb technology is reaching fundamental material limitations, and new systems must be explored to continue improvement. In this thesis, we investigate a thin film structure that has been proposed to dramatically increase both the efficiency and maximum accelerating gradient achievable in these applications.

First, we discuss the reasoning behind our choice of Nb_3Sn/Al_2O_3 for the exploration of these properties and the challenges involved in growing these materials. We show that the challenges of processing Nb_3Sn can be overcome with a high-temperature growth method and that there is a growth window where the stoichiometry of the Nb_3Sn films is self-regulating.

Second, we scale growth up to wafer-scale films and heterostructures, and confirm the structure and quality using cross-sectional TEM. RF measurements were conducted in cavity geometry at low RF fields on wafers of Nb_3Sn and Nb_3Sn/Al_2O_3. The results of these measurements are encouraging, showing that the Nb_3Sn has very low surface resistance, and compares well to a bulk Nb sample measured in the same cavity. The multilayer sample had a higher quality factor than the single-layer film, confirming that the Al_2O_3 layer contributes very little to surface resistance.

The development of this system makes it possible to explore the effects of film morphology and heterostructure geometry on the quench field, and to study the physics of the superconductor-insulator-superconductor structure under high frequencies and magnetic fields.

Acknowledgments

Five years goes by very quickly, but upon looking back, I am startled by the number of people I encountered who have been meaningful to my time here.

Firstly, I'd like to thank my advisor Chang-Beom Eom for giving me the opportunity to study under him. His mentorship and financial support has made the last few years of my intellectual and personal growth possible. Our collaborator Alexander Gurevich's guidance and insight was critical to the conceptualization and direction of the project, and helped shape my expertise in RF superconductivity. I'd like to recognize the other members of my committee, Robert McDermott, Mark Rzchowski, and Xudong Wang, who provided helpful discussion on the physics, instrumentation, and growth processes.

My fellow lab mates in the Oxide Lab made coming in to work something I would look forward to each day. We have built a strong positive work environment, and our lively (and sometimes loud) discussions about science are something I enjoyed immensely about working here. I extend my thanks to everyone who worked with me during my time here, as each person was responsible for teaching me a good number of things. I'd like to specifically recognize Tony Edgeton, Neil Campbell, and Patrick Strohbeen (though he worked in the next lab over) for always responding strongly to my prompts for clarification on physics, or thermodynamics, or whatever I needed help on at the time; Jon Schad, for helping me with software and lab equipment and eventually setting up a way for me to monitor my equipment from home; Jong-Hoon Kang for going through the whole degree with me and making time spent here fun; Jacob Patzner and Shane Lindemann for accompanying me on coffee and lunch outings, even when they didn't really want to; and Jacob Podkaminer and David Harris for offering their thoughts and advice on post-doctoral work.

Outside of the lab, the community at Pres House played a central role in keeping me grounded and engaged outside of work. It could sometimes be brutal to wake up early to make the weekly Coffee Tours, but I'd always do it. Thanks to Mark and Erica for keeping up with my life and being involved, and to all the folks who would take the time to catch up with me every week and make space for meaningful time spent together.

I had the support of my family the entire time I was here, and I don't want to take it for granted. Thanks to my parents and my sister Rina, who encouraged me to continue working and finish my degree so that I could come home. Their many visits to Wisconsin broke up the year into smaller, more manageable chunks and helped me stay productive.

Finally, I'd like to acknowledge my wife Liz, who was the first to hear about new developments in the lab and in my life and helped me through all of it. My time here would have been very different and much more difficult without her. Being away from family and home was hard for both of us, but it has made a world of difference that she came out here with me.

Contents

List of Figures

CHAPTER 1

Introduction

1.1 Particle accelerators

Particle accelerators are synonymous with high-energy physics, and most people with a passing interest in science have heard of CERN and the LHC. Accelerator cavities are the component tasked with bringing the charged particles in question to the required velocity for high-energy work. In the LHC, these particles are collided with one another. In some materials-science related research, these components can accelerate electrons, which then can be manipulated with electric and magnetic fields to generate high-energy x-rays.

The basic layout of an accelerator cavity is shown in Figure 1-1. Typically, the cavity is excited with an electromagnetic wave such that the electric field of a standing wave points along the cavity axis, and the magnetic field forms loops perpendicular to this direction [1]. The electrical and magnetic components of this wave are shown in Figure 1-1b.

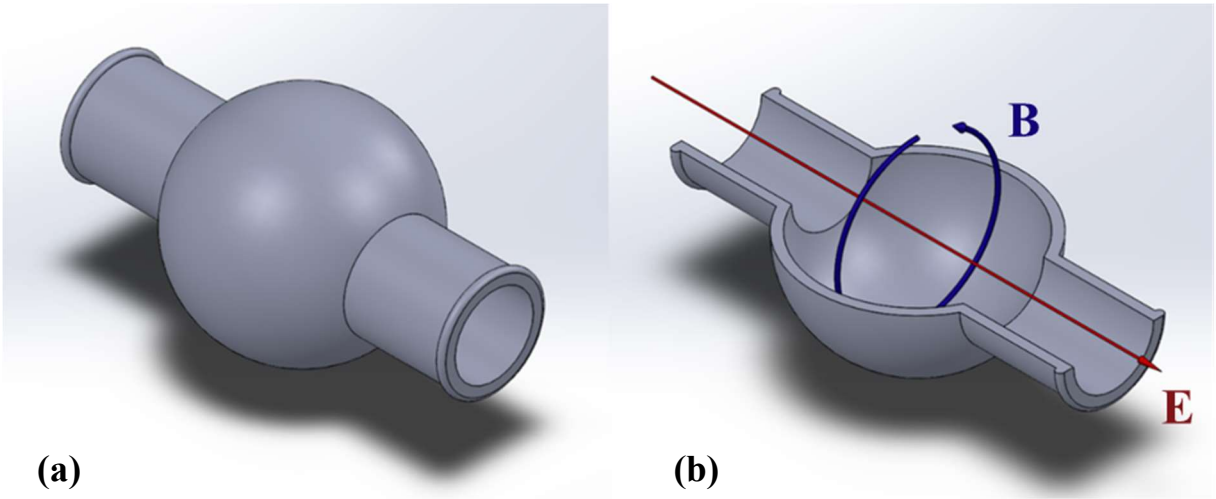

Figure 1-1: (a) schematic of the shape of a RF accelerator cavity, and (b) a cutaway of this cavity showing electric field direction (red) and magnetic loop direction (blue)

The average accelerating field experienced by a charged particle passing through the cavity, E_{acc}, is an important figure of merit in evaluating these cavities. In general, a higher E_{acc} is desired, since this means that fewer cavities are required to reach high particle energies, and power efficiency is maximized.

The quality factor Q_0 is another figure of merit relating to the efficiency of these chambers, expressed as $Q_0 = \omega_0 E_{stored}/P_{diss}$, where ω_0 is the operating frequency, E_{stored} is the energy stored in the standing wave in the cavity, and P_{diss} is the power dissipated by the cavity per cycle. Higher Q_0 mean cavities that require less power input to maintain their E_{acc}. When made from standard electrical materials such as Cu, cavities operate with a Q_0 of 10^4~10^5 and cannot be operated continuously due to the dissipation of large amounts of energy at high fields and high frequencies [2–4]. Because of the heat evolved from P_{diss}, these cavities must be cooled, usually with water.

In order to improve on these properties, it is necessary to turn to materials with lower resistivity, which in turn reduce P_{diss}. This is indeed where the industry has moved, with cavities manufactured from superconductors, which have zero resistivity at DC fields.

1.2 Superconductivity

Discovered over a century ago when mercury was cooled in liquid helium[5], superconductivity encompasses far more than zero resistivity. Though they do exhibit this feature below their critical temperature T_c, they are also defined by their perfect diamagnetism. When magnetic field is applied to a superconductor, it generates a field pointing in the opposite direction such that the magnetic field inside of the superconductor is zero. This is known as the Meissner effect. However, magnetic field does not simply drop to zero at the surface of the superconductor; there is a length scale associated with the drop-off in magnetic field, known as the penetration depth λ (Figure 1-2). It is in this region λ from the surface that the charge carriers in the

superconductor interact with external field, and because of this, this region is of great interest for resonating cavities made of superconductors.

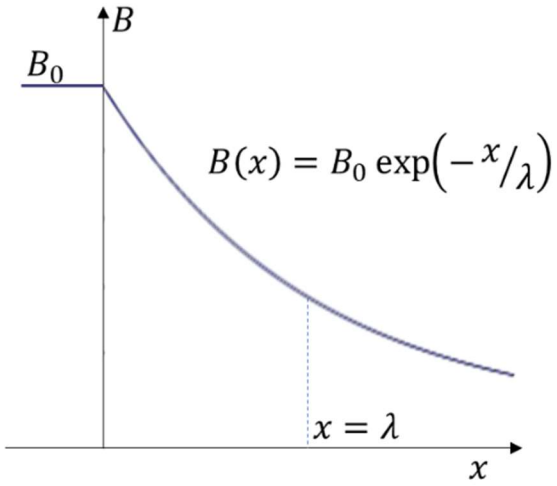

Figure 1-2: decay of the magnitude of a magnetic field. B_0 describes the constant intensity outside of the superconductor, and it decays exponentially with depth x.

In the BCS model of superconductivity, below T_c electrons near the Fermi lever condense into Cooper pairs, which have integer spin and hence behave like bosons, falling to the lowest energy level [6]. This opens a gap in the density of states, as shown in Figure 1-3a. However, at any temperature T > 0 K, a proportion of the electrons are thermally excited such that the superconductor hosts both Cooper pairs and unpaired electrons, or quasiparticles. Their total population is described by

$$n_{qp}(T) = 2N_0\sqrt{2\pi k_B T \Delta(T)}\exp[-\Delta(T)/k_B T] \qquad \text{[Eqn. 1]}$$

as visualized in Figure 1-3b for some temperature $0 < T < T_c$ [7]. Within the region described by λ, both Cooper pairs and quasiparticles interact with externally applied fields.

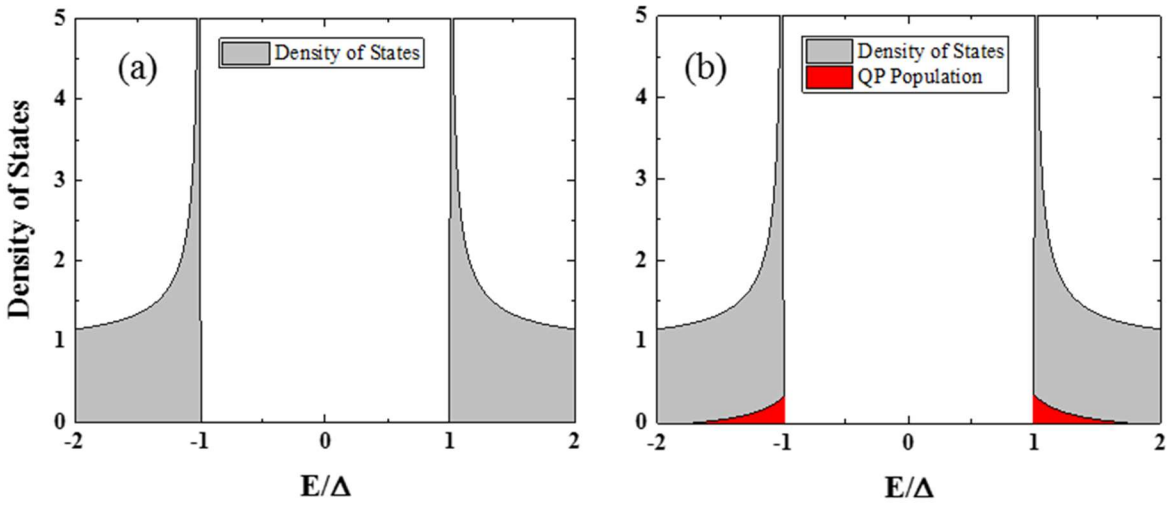

Figure 1-3: Density of states in a superconductor. (a) Ideally, the states below the gap are full, and above the gap are unoccupied. (b) at T > 0, some proportion of the pairs are broken by thermal energy, leaving a population of unpaired electrons and holes ("quasiparticles").

The presence of both of these states in the superconductor makes it useful to picture the electrical response of superconductors in terms of a two-fluid model[8]: a dissipative quasiparticle fluid flowing in parallel with a non-dissipative supercurrent, as shown in a circuit diagram in Figure 1-4. The superfluid Cooper pairs do not scatter and hence have no dissipative component, but have a large inductance due to their momentum.

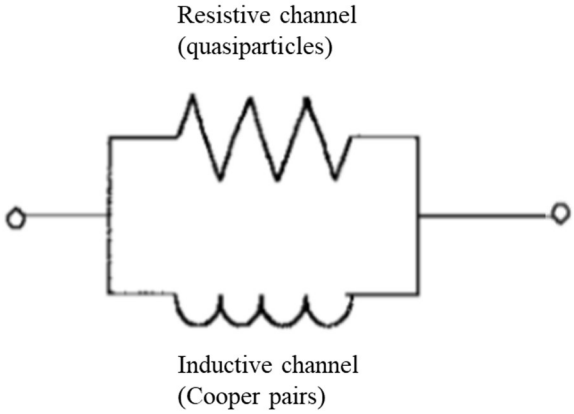

Figure 1-4: Simple conceptual model of the surface region of a superconductor as parallel inductive and resistive channels.

Under DC excitation, the non-dissipative fluid shorts out the dissipative channel, leading to zero resistance. However, under AC fields, the dissipative channel becomes active, since momentum of the Cooper pairs must be reversed during each cycle (the inductance forces current through the resistor). The resistance arising from this mechanism at the surface of the superconductor, the surface resistance R_s, is described as

$$R_s = \frac{A\omega^2}{T}\exp\left(-\frac{\Delta(T)}{k_B T}\right) + R_i \qquad \text{[Eqn. 2]}$$

where ω is the angular frequency of the cavity, $\Delta(T)$ is the temperature-dependent superconducting gap size, k_B is the Boltzmann constant and T_c is the superconducting transition temperature [9]. A is a fitting parameter that describes departure from ideal superconducting behavior due to extrinsic factors such as grain boundaries and mean free path. The first term describes the surface resistance caused by quasiparticles described by BCS theory, and the second term R_i is a largely temperature-independent residual surface resistance caused by factors other than the superconducting state.

P_{diss} can be calculated from R_s as

$$P_{diss} = \frac{1}{2}R_s \int_S |\mathbf{H}|^2 \, ds \qquad \text{[Eqn. 3]}$$

where **H** is the external magnetic field at the cavity surface. In order to minimize P_{diss}, it is critical to maintain low R_s. In Eqn. 2, this means maximizing the gap size $\Delta(T)$ and minimizing the temperature T since the exponential term dominates at low T.

The behavior described above only applies for superconductors in the Meissner state, where magnetic fields are expelled from the interior of the superconductor. At high enough fields, this assumption no longer holds true. In Type-I superconductors, when the external magnetic field exceeds a critical magnetic field B_c, the superconducting phase is destroyed, and the sample reverts

to a normal conductor. Values for B_c are much lower than the fields required to operate SRF cavities, making these materials impractical for these applications.

Type-II superconductors, in contrast, have two distinct critical magnetic fields: the lower, B_{c1}, and the upper, B_{c2}. At B_{c1}, magnetic flux lines penetrate into the bulk of the superconductor, as shown in Figure 1-5. They pass through a normal-conducting tunnel of material with diameter ξ, the coherence length of the superconductor. The flux line is surrounded by a supercurrent that keeps it contained, known as a vortex. Between the normal conducting core and the bulk of the superconductor, the magnetic field decays with characteristic length λ, as with the superconductor-vacuum interface. Type-II superconductors are defined by the ratio $\kappa = \lambda/\xi > 1$; this ratio dictates that it is energetically favorable to form these vortices than for the superconducting state to be destroyed altogether, as with Type-I superconductors.

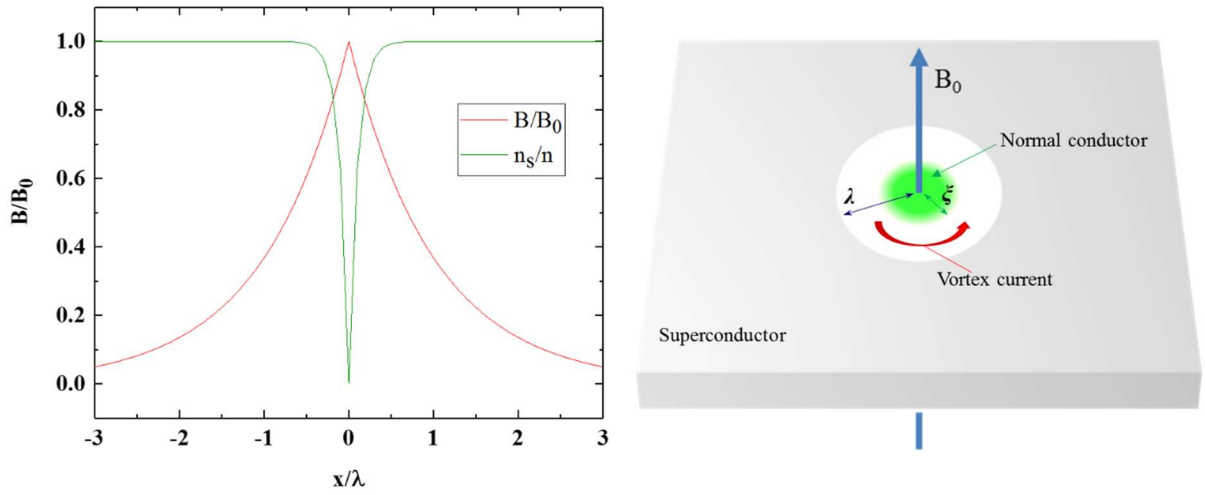

Figure 1-5: Schematic of a Type-II superconductor above B_{c1}. Magnetic flux is confined to the core of a normal-conducting filament, and decays exponentially into the superconductor.

When there are vortices inside of the superconductor in an SRF cavity, several problems arise. Most prominently, a part of the cavity is no longer superconducting. These normal-

conducting portions dissipate energy as heat, and the Cooper pairs must re-condense and be broken again at a rate on the order of GHz as the field sign reverses, a process which also evolves heat. This heat leads to the overall temperature around these vortices rising, which leads to even more surface resistance and power dissipation, resulting in a thermal runaway and cavity quench as the quality factor of the cavity drops dramatically. In order to avoid these problems, cavities must operate such that the field at the surface does not cause vortex currents. This way, magnetic field is confined to the surface layer of the cavity, and vortices do not penetrate into the bulk to cause cavity quench.

However, B_{c1} is not the only consideration for vortex penetration. In the cavity geometry, where the magnetic field is always parallel to the surface, though it may be thermodynamically favorable for a vortex to exist within the bulk, the boundary conditions imposed by the surface give rise to an energy barrier, preventing vortices from nucleating [10]. In theory, this barrier can prevent flux entry up to the superheating field B_s, which can be shown for strongly Type-II materials to be proportional to the thermodynamic critical field $H_s \propto H_c$ [11]. Depending on the purity of the sample and the presence of defects at the surface, the field of actual flux penetration lies somewhere between B_{c1} and B_s. Currently, the state-of-the art material that satisfies these properties is niobium (Nb).

1.3 Nb cavities

With a ratio of $\lambda/\xi = 1.02$ and a T_c of 9.2 K, Nb is the highest-T_c elemental superconductor, and on the cusp between Type-I and Type-II superconductors [12]. It also has the highest B_{c1} and B_s among the elemental superconductors, satisfying both the low-R_s (large Δ) and high-field (high B_{c1}) requirements for a high-performance SRF cavity. For this reason, it has been the most heavily studied SRF material, with the most advanced cavities able to operate at E_{acc} of 48 MV/m and peak

fields around 200 mT, with Q_0 around $2x10^{10}$. Recent studies include surface treatments such as annealing and polishing that can decrease the number of defects, and thus increase B_{c1}.

In a relatively recent discovery, Nb SRF cavities were annealed in N_2 atmosphere at high temperatures [13–17]. When the surface is etched and polished to remove defects, these cavities have dramatically increased Q over cavities that do not receive the N_2 treatment, as shown in Figure 1-6. They exhibit an anomalous rise in Q with applied field up to a peak, after which Q decays normally, until cavity quench occurs at a field lower than the untreated cavities. The origins of this behavior are still under investigation. The trade-off is that, due to the impurities in the surface, vortex penetration can occur locally at a lower field than in pure Nb, leading to a cavity quench at lower E_{acc}.

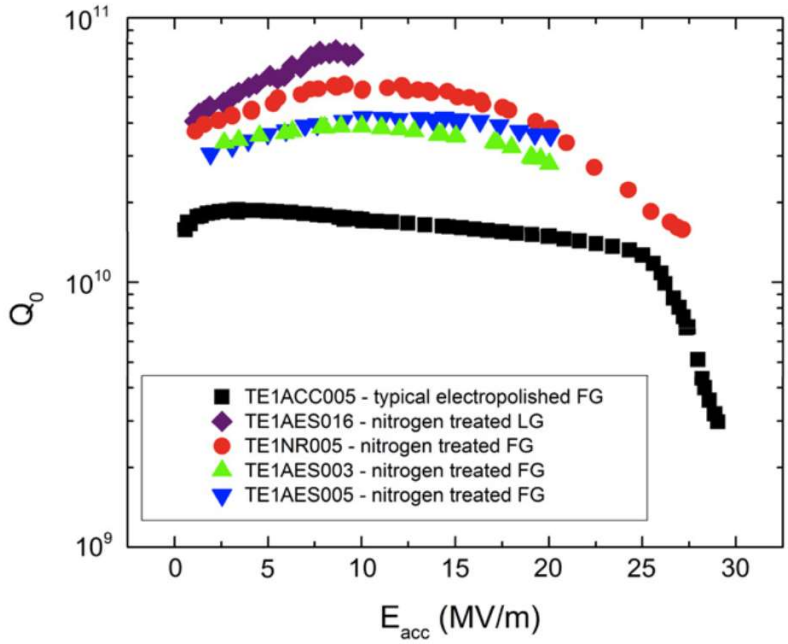

Figure 1-6: Quality factor in Nb cavities treated in nitrogen shows dramatic improvement over bare Nb (black squares), but quenches at lower fields. Reproduced from [14].

After decades of research, Nb SRF cavities are now coming up against fundamental material limitations. The best Nb cavities can reach peak magnetic fields inside the cavity of 200

mT, which approaches the field at which the screening current in the Nb reaches the depairing density J_c. J_c is a fundamental property of the superconductor, at which superconductivity is abruptly destroyed. This leaves little room for improvement and diminishing returns for further research into Nb cavities, leading some to pursue research in different directions. These include making the cavity from, or coating the cavity in, another material, which has been met with some success. Another proposal is to layer the cavity in alternating dielectric and superconductor layers, manipulating the thermodynamics of vortex penetration to increase B_{c1}[18]. This proposal is explored in the following section.

1.4 SIS multilayer physics

Although B_{c1} for bulk superconductors is a nearly fixed value, in thin films B_{c1} can vary based on the direction in which the external field is applied. When the field is applied perpendicular to a thin film, B_{c1} is lower than in the bulk. However, when the field is applied parallel to the surface of a film with thickness $d < \lambda$, vortex currents caused by magnetic flux penetration becomes thermodynamically unfavorable[19]. This raises the B_{c1} in these situations, which theoretically follows the trend

$$B_{c1} = \frac{2\varphi_0}{\pi d^2}\left(\ln\frac{d}{1.07\xi}\right) \qquad \text{[Eqn. 4]}$$

These thermodynamics can increase B_{c1} up to the superheating field B_s, where the Meissner current becomes unstable. Taking advantage of this property, it was proposed that thin layers of superconductor with thickness $d < \lambda$ could be layered onto bulk Nb cavities, separated from the bulk by a thin dielectric layer to isolate it and ensure the thermodynamic conditions are met. These thin films can screen higher fields than the bulk can withstand, raising the peak field B_{pk} at which the cavity can operate. The layering could be expanded to include multiple superconductor (S) and

insulator (I) layers to screen much higher fields, as shown in Figure 1-7; because the films are thinner than λ, the total field screened by a single layer is necessarily somewhat small (less that $e^{-1} \approx 0.37$).

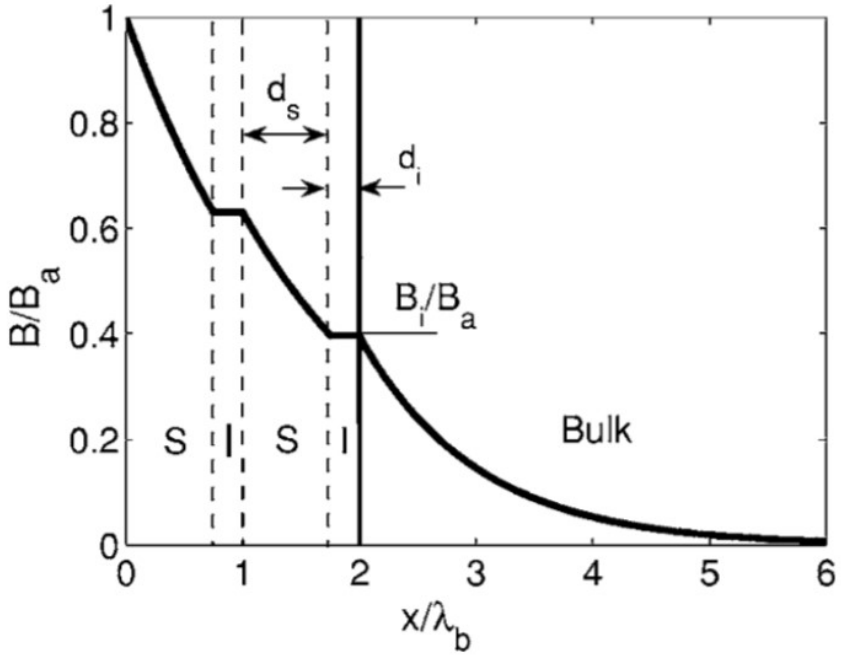

Figure 1-7: The proposed SIS multilayer structure, which screens out external magnetic fields that are higher than B_{c1} of the bulk. Reproduced from [18].

The thin film need not be limited to Nb. By virtue of being a thin layer, some of the material limitations imposed for the cavity do not apply. For example, the cavity itself must have high thermal conductivity in order to transfer heat from dissipation at the inside surface into the helium bath. This restriction is lifted for very thin films, as these do not contribute significantly to the rate of heat transfer. Similarly, thin films deposition processes allow much more flexibility in materials selection than the machining processes used in fabricating bulk cavities.

Table 1-1: Various superconducting materials and their critical parameters.

Material	T_c (K)	H_c (T)	H_{c1} (mT)	H_{c2} (T)	λ (nm)	Δ (meV)
Nb	9.2	0.2	170	0.4	40	1.5
Nb_3Sn	18	0.5	40	30	85	3.1
NbN	16.2	0.23	20	15	200	2.6
MgB_2	40	0.32	20-60	3.5-60	140	2.3; 7.1

Some of the relevant materials parameters for candidate coating materials are shown in Table 1-1. Theoretically, the B_{c1} of these coatings can be increased as high as $B_{sh} \sim B_c$; in Nb_3Sn, this means a potential improvement by a factor of 2 in the operating field of cavities. In addition to possibly improving B_{c1}, selecting a different material for the coating can mean a higher Δ, which according to Equation 2, leads to a lower temperature-dependent contribution to the BCS R_s.

There has been some debate on the maximum field that could theoretically be screened by thin films on bulk superconducting cavities. Some have contended that the SIS structure actually reduces the barrier to vortex penetration to zero, defeating the purpose entirely [20]. On the other hand, it has been shown using analysis of the depairing instability of Meissner currents that, due to counterflow currents induced by the bulk Nb in the films, B_{pk} at the surface of the SIS structure in the cavity geometry can actually exceed the superheating field B_{sh} for the optimal film thickness [21].

A number of researchers have grown SIS multilayers of various materials, such as NbN/MgO and MgB_2/Al_2O_3 [22–24]. However, measurement of the important quantities for these films (quench field B_{quench}) is difficult without scaling up to a full coating on the interior of a cavity.

Magnetic field must be applied parallel to the film surface, which requires a measurement system with fine adjustability of the direction of the field. Misalignment results in a nonzero component of the magnetic field perpendicular to the surface, which can penetrate into the film and cause the sample to quench at much lower fields than would be achievable in truly parallel field. Many of the measurements are conducted with DC fields, which can significantly affect the thermodynamics of the environment. One detailed study on the RF response of a $MgB_2/Al_2O_3/Nb$ sample was conducted in a RF cavity in 2012 [24]. This study concluded that thin MgB_2 films were successful in raising B_{c1} to 210 mT from the bulk value of 46 mT in DC measurements. However, the quench field B_{quench} under RF fields was 42 mT, when it was expected to be > 90 mT. It was found that the quench was thermal, caused by high surface resistances caused by inter-diffusion of elements during the coating process. To date, the quench field of a SIS multilayer has not been measured under RF fields to be higher than in the bulk. With access to the same in-cavity RF measurement technique, it is possible to measure films and multilayers grown in our lab, test the SIS hypothesis, and learn more about the physics of this geometry.

1.5 Nb_3Sn as a candidate material

Nb_3Sn was the material chosen for this project. Nb_3Sn has a T_c of 18 K and a gap of $2\Delta \sim 6$ meV, minimizing the exponential contribution to R_s and introducing the possibility of operating SRF cavities at temperatures attainable in closed-cycle cryogenic refrigeration systems. As mentioned above, B_c of Nb_3Sn is approximately twice that of Nb, which raises the ceiling on the accelerating field at which SRF cavities can be operated by approximately the same factor. Nb_3Sn is a very well-studied material for DC high-current superconducting wires. It crystallizes in the A15 structure, as shown in Figure 1-8, with Sn atoms occupying BCC sites and Nb atoms forming chains along the faces.

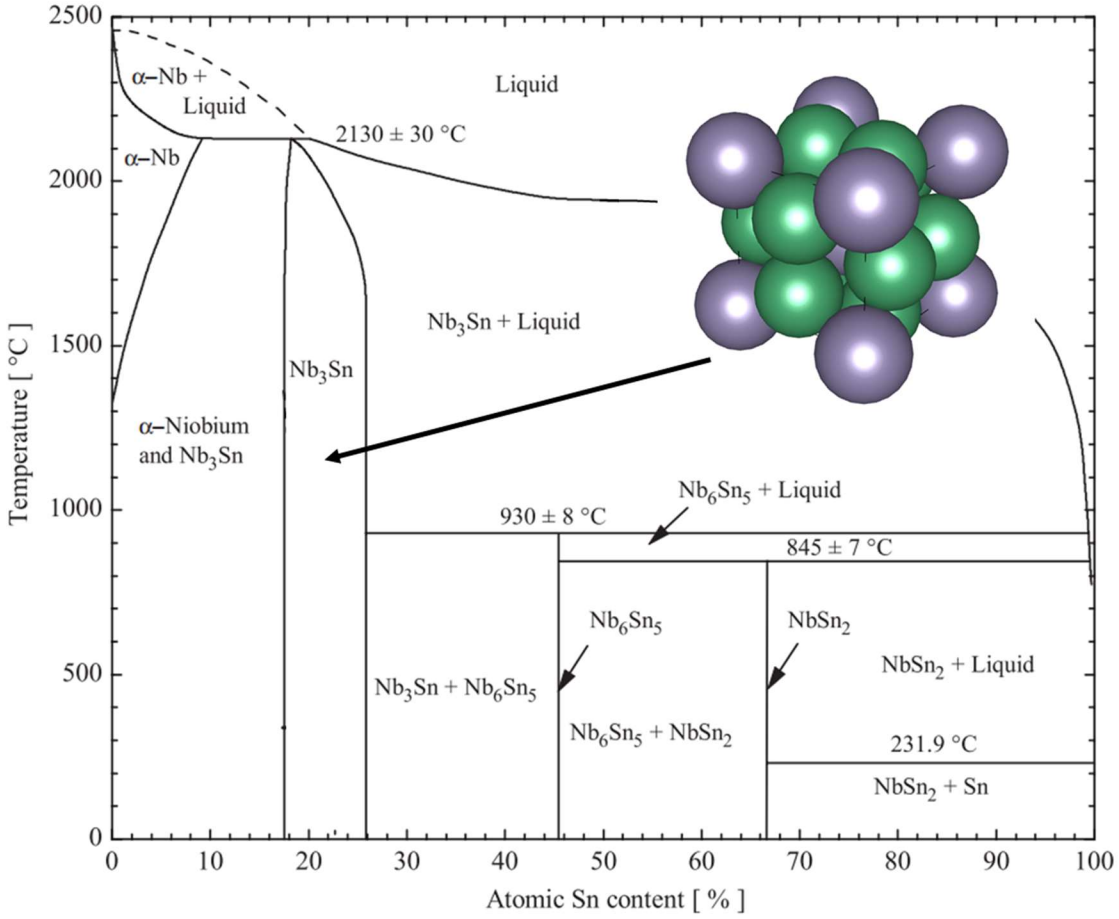

Figure 1-8: Phase diagram of the Nb-Sn system. Crystal structure of Nb_3Sn is shown in upper right.

Figure 1-8 also shows the Nb-Sn phase diagram. Nb_3Sn is stable over the compositional range 18-25% Sn, where off-stoichiometry is accommodated by substitutional Nb_{Sn} defects. At temperatures above 930 ˚C, the phase diagram is dominated by a region of solid Nb_3Sn + Sn(*l*), where other intermetallic phases (Nb_6Sn_5 and $NbSn_2$) are unstable. While both of these compounds are superconducting, their T_c are much lower than Nb_3Sn. As such, they contribute disproportionally to R_s under RF conditions, and they are highly undesirable in these applications. In order to grow high-quality Nb_3Sn films, it will be necessary to conduct deposition at these very high temperatures.

In some studies, this Nb_3Sn + Sn(*l*) phase region has been leveraged to produce stoichiometric Nb_3Sn films by providing excess Sn at high temperatures to re-evaporate excess Sn from the film surface during growth [25,26,27]. This was successful in producing films with good R_s as measured by calorimetry, and it is the growth method that was eventually employed in producing multilayers for this project.

CHAPTER 2

Past Growth Methods for Nb_3Sn Films

This section describes some of the configurations and processes used to grow Nb_3Sn films, and the superconducting properties of these films. The shortcomings of these methods and the necessary improvements are explored.

2.1 Single-Target Method

The first approach taken in preparing these samples was to sputter the films onto heated Al_2O_3 substrates from a single stoichiometric Nb_3Sn target (Figure 2-1).

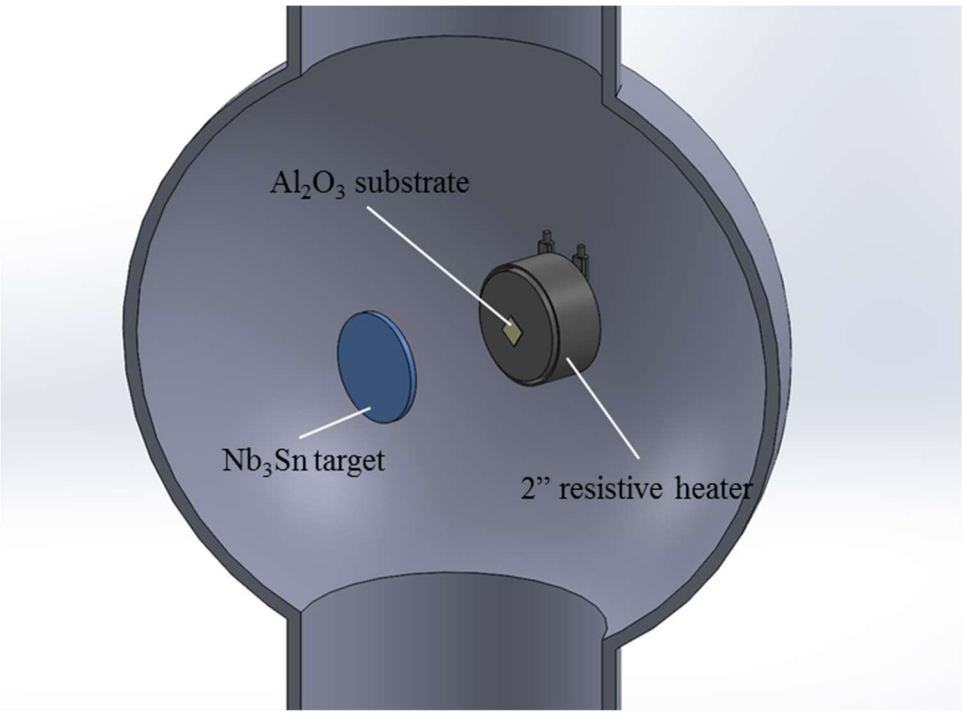

Figure 2-1: Schematic of growth chamber layout for films sputtered from a single stoichiometric Nb3Sn target.

This is a method that has been utilized in a number of past studies, and results in films with T_c generally lower than the bulk 18 K [28,29]. The study by Wu et al. shows some dependence of Sn composition on sputtering pressure, but this appears to be the extent of control over stoichiometry

in single-target configuration. Andreone et al. measured single-target sputtered films for their microwave R_s and other RF properties using meander-line resonators. They produce R_s of 2 μΩ and Q of $5x10^4$ at 4.2 K and very low applied fields at 1.3 GHz [30]. Figures of R_s and Q from that study are reproduced in Figure 2-2.

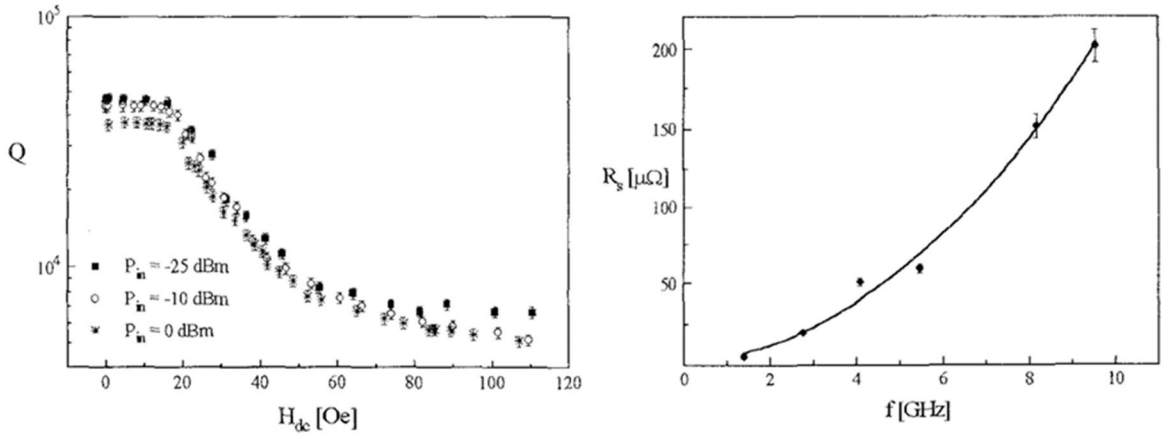

Figure 2-2: Plots of Q_0 and R_s for sputtered Nb3Sn meander-line resonators grown by Andreone et al. Reproduced from [30].

This method has the advantage of being simple, and it was the first one undertaken in this study. A R-plane Al_2O_3 substrate was mounted with silver paint on to a resistive MeiVac 2" heater; Nb_3Sn was sputtered from a stoichiometric 2" target prepared though powder methods by Toshima Inc. The chamber was evacuated to base pressure of $2.0*10^{-7}$ torr before being backfilled with Ar to pressures of 2-40 mtorr. The magnetron was power-regulated, with sputtering power varied between 25-200 W. Substrate temperature was set in the range of 800-950 ˚C.

These films were often not superconducting, or had T_c well below 18 K. Some sample transitions are shown in Figure 2-3. This behavior was not fully investigated, but it was inferred that this method resulted in films that were both Sn deficient and inhomogeneous. Since the target began at 25% Sn, films could only be grown with composition <25% Sn (though Wu claims otherwise in [29], stoichiometry control through pressure was not pursued).

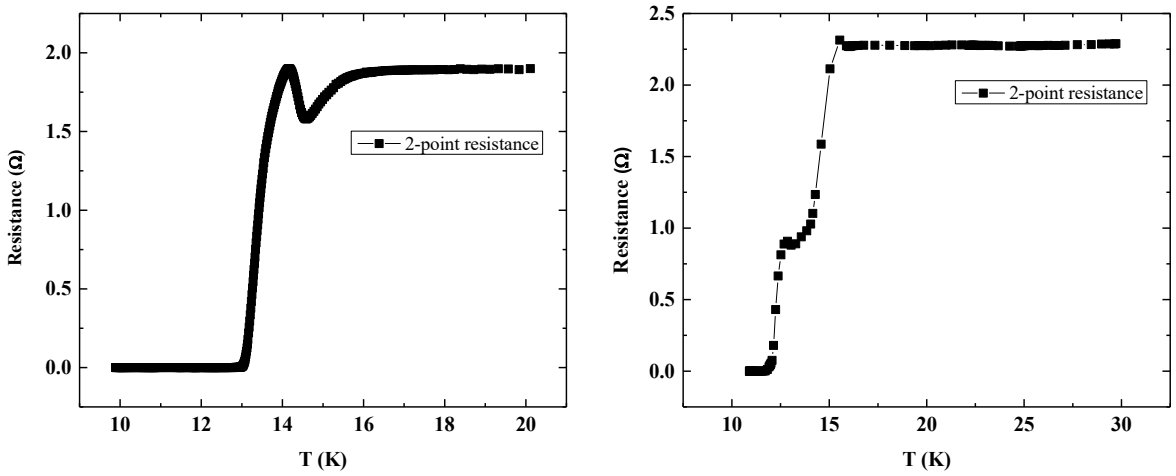

Figure 2-3: Resistance vs. Temperature for some films grown by the single-target method. Transitions are not smooth, and T_c is depressed.

2.2 Stack deposition and annealing

When it became clear that sputtering from a single stoichiometric target would always result in Sn deficiency or poor crystalline quality, the next approach was to control Nb and Sn individually, such that Sn could be provided to the films in excess. Initially, this was approached by depositing Nb and Sn in alternating layers and annealing the stack in vacuum.

At least two studies have gone this route in the past, including one in which the process was applied to a RF cavity. In 1985 a group studied Nb_3Sn films prepared by annealing stacks of Nb and Sn at high temperatures [31]. The multilayer periodicity varied from 75 to 300 Å, spanning the range of periodicities used in our approach, with total film thicknesses at 500 nm, far thicker than the target for our project (50-100 nm). To see the effects of stoichiometry on the superconducting films, Nb:Sn ratios in the unannealed stacks ranged from 2.7:1 to 4.6:1. Using in-situ XRD during annealing, Vandenberg et al. showed that Nb_3Sn phase formation begins at 520 °C, and Nb_6Sn_5 persists in the films at detectable levels up to 800 °C. T_c in the annealed films were best for films annealed above 750 °C, and the highest T_c was at 17.45 K for a film annealed at

850 °C, with a nominal Nb:Sn ratio of 2.7:1. Annealing at higher temperatures did not seem to affect the superconducting properties strongly. RF properties of these films were not reported, but the data on T_c was taken as a valuable starting point.

In 2009, another group produced a similar study [32], in which stacks of Nb and Sn were deposited at room temperature, and then annealed at high temperatures for 3 hours at temperatures between 600 and 930 °C. Nb:Sn ratio was controlled by manipulating the ratio of the sputtering current during deposition; this is different from the Vandenberg study in that the nominal composition before annealing is not known. The best films produced by this process had a T_c of 17.9 K and transitions as narrow as 0.02 K, though these transition curves are not shown. Interestingly, T_c rises with increasing Nb flux, rather than decreasing as one might expect with lower Sn content. XRD shows Nb_3Sn is the only phase present after annealing at 930 °C. When this process was applied to 6 GHz Nb cavities, the Q_0 was measured as high as $4x10^6$. The bare Nb cavities that were measured with a Q_0 of 10^7, indicating that the Nb_3Sn films in this study had higher surface resistance than the bare cavity. This could be an indication of incomplete coverage, inhomogeneity in the film, poor stoichiometry control, or a high defect density, all of which would affect overall surface resistance.

Adapting this approach to create 50 nm-thick Nb_3Sn films, the earlier single-target approach was modified to include two magnetron guns, one for Nb and the other for Sn. These are set at right angles to one another. The substrate can rotate between the two, allowing for alternating deposition and annealing without breaking vacuum. A schematic of this setup can be found in Figure 2-4.

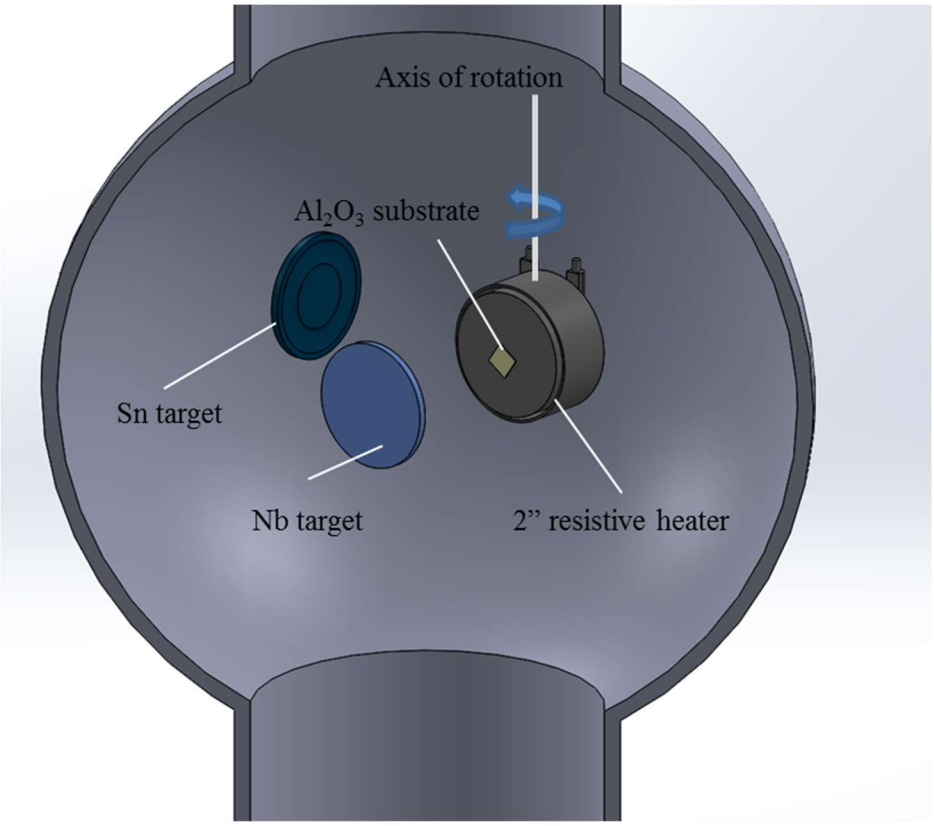

Figure 2-4: Schematic of growth chamber configuration for Nb/Sn multilayer annealing growth. Heater can be rotated to face either Nb or Sn target.

In order to have a stoichiometric ratio of Nb to Sn, it is necessary that the ratio of thicknesses of Nb to Sn films be 2:1. Layer periodicity was set to 33 nm, and later to 9 nm. A schematic of these multilayers is in Figure 2-5. Nb was always the last film to be deposited in order to create a barrier to Sn loss during annealing. These were annealed at temperatures ranging from 850 to 950 °C for 15-120 minutes to produce the Nb_3Sn film.

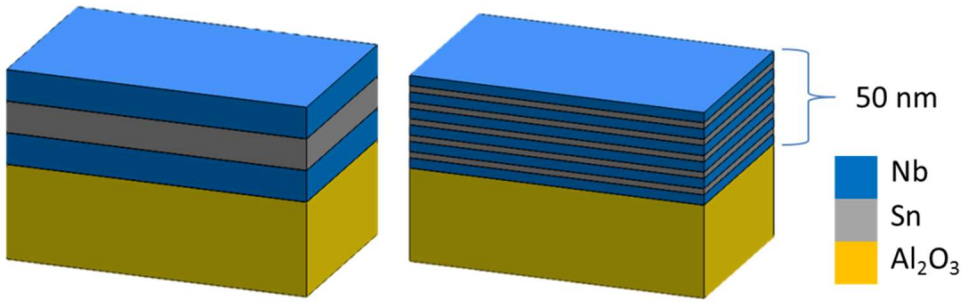

Figure 2-5: Nb and Sn layered stacks, which were annealed to produce Nb_3Sn films. Total thickness of the stacks was targeted at 50 nm. Samples with 3 total layers and 11 total layers were tested.

In order to ensure correct layer thicknesses, thicker films were first deposited and measured by a profilometer. Their thicknesses were divided by deposition time to calculate a deposition rate. This worked well on Nb films, which were very smooth. However, as Sn films were very rough, it was difficult to measure an accurate deposition rate. An AFM image of a thick Sn film is shown in Figure 2-6. RMS roughness is 85 nm, making any profilometry measurement somewhat inaccurate; nonetheless, a nominal rate was calculated, and this was used for the first set of films. More Sn was added to the Sn layers to gauge the effect of nominal excess on film properties. Sn excess ranged from 5% to 100%.

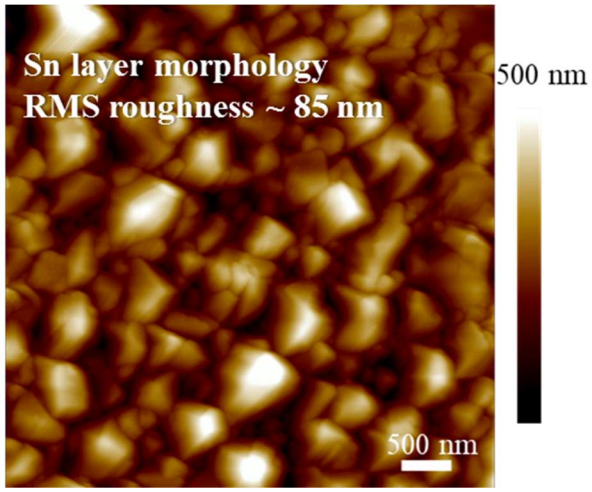

Figure 2-6: AFM image of sputtered Sn. If this is representative of Sn films in the stacks, the amount of Sn available to the Nb layers may vary considerably across the film.

This resulted in films with much higher T_c and sharper ΔT_c than those produced with the single-target method. WDS measurements were also performed on these samples; energy spectra of emitted X-rays were fitted using the estimated thickness of the samples to extract Nb:Sn ratios. T_c and ΔT_c of these samples are plotted against these Nb:Sn ratios in Figure 2-7. Samples which incorporated extra thickness into the Sn layers are labeled. There are no clear correlations to be made: nominal Sn excess does not correlate well with Nb:Sn ratio extracted by WDS, and neither one has a strong correlation with T_c.

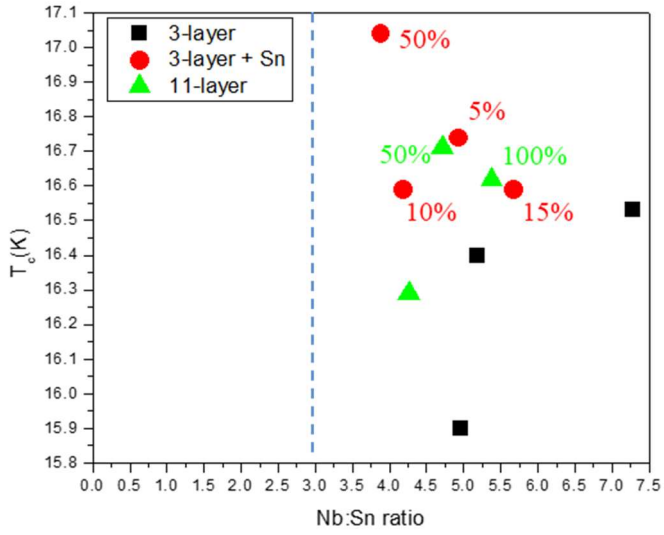

Figure 2-7: T_c of annealed stacks, plotted against the Nb:Sn ratio extracted from WDS. Nominal Sn excesses are labeled next to their respective data points.

Some films had Nb:Sn ratio as high as 7 (12.5 % Sn), which should put these films outside of the single-phase Nb_3Sn region, which extends from 18-25% Sn. However, these films had T_c of 15-16 K, which reflects a Sn composition closer to 23% according to [33]. This suggests extreme inhomogeneity in the films, with a Sn-rich path being measured in the DC measurements. Considering the roughness of the Sn layer, it is possible that regions with thicker Sn before annealing became Sn-rich areas in the final film, giving rise to a strong compositional gradient locally.

CHAPTER 3

Co-sputtered Epitaxial Nb_3Sn Films

Another method was needed which could independently control Nb and Sn rates and reach high growth temperatures. The inconsistency and potential inhomogeneity of the films grown using single-target sputtering and stack annealing were addressed by adjusting the geometry to allow co-sputtering of Nb and Sn. Rather than relying on ex-situ profilometry to calculate growth rates, a quartz crystal monitor from Inficon Co. was incorporated into the system. Nb and Sn rates were calibrated immediately prior to growth, and the appropriate conditions were selected for each growth.

To reach temperatures above 930 °C more consistently and safely, and to grow large wafers, the resistive heater was exchanged for a radiative heater. This was used to heat a Mo block, to which (10-12) (R-plane) Al_2O_3 substrates were mounted with silver paint. Homogeneity of Nb and Sn flux across the film area was ensured by rotating the substrate azimuthally during growth.

In order to reach even higher growth temperatures, a hole was cut through the Mo substrate block and the substrate mounted inside of it, such that radiative flux from the heater could pass directly through the substrate, as shown in Figure 3-1. Al_2O_3 has a bandgap of 6.9 eV [34], and the majority of the heater radiation is in the infrared range. Sputtered Nb and Sn deposits onto the substrate and absorbs the heat from the radiation directly, leading to much higher growth temperatures.

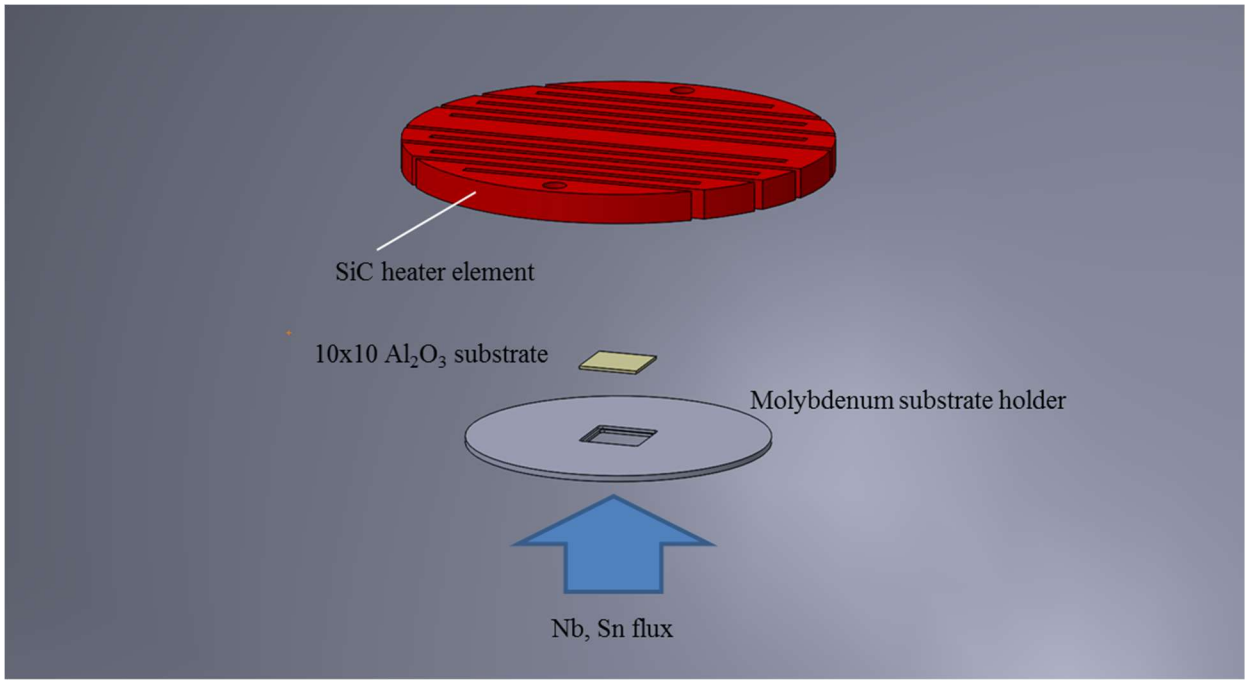

Figure 3-1: Close-up schematic of the heater configuration. Substrate is exposed to heater radiation from above, while Nb and Sn is sputtered from below through a hole in the Mo substrate holder.

Temperature monitoring in this setup proved to be complex. A K-type thermocouple mounted behind the heating element proved to be too fragile; it was heated beyond its specifications, and the junction failed. After several film growths, it did not provide consistent readings.

An optical pyrometer (Chino Corp., model IR-CAQ, $\lambda = 0.9$ μm), mounted to the bottom of the chamber and peering through a CaF_2 window, was pointed at the substrate. Since Al_2O_3 is transparent to infrared rays, this effectively monitored the temperature of the heating element during growth, until the Nb_3Sn film grew thick enough to fully absorb all the radiation. The value of the emissivity was chosen to be $\varepsilon = 0.35$, based on emissivity data on Nb from [35,36]. Though this likely does not match the true emissivity of Nb_3Sn, the value of monitoring with the pyrometer is in being able to compare the behavior of T_p between samples. With this goal, the emissivity was chosen and maintained between all samples.

This provided more consistent temperature information, but the behavior of the pyrometer reading T_p proved to be complex over the course of growth. Figure 3-2a shows T_p over the course of a growth on a 10x10 mm substrate. Only the heater voltage was regulated for this growth. Rotation of the heater starts at the point labeled as 1, where oscillations appear in T_p. This is due to the rotation causing the heater element to travel across the pyrometer's viewing window, changing the observed temperature, as illustrated in Figure 3-2. Sputter guns are switched on at 2, and T_p immediately begins to drop as the film begins to obscure the heater element. Oscillations from rotation begin to dampen as the film becomes thicker, and at point 3 the oscillations have dampened considerably and T_p approaches a constant value. Power to the heater is switched off at point 4, and T_p declines rapidly.

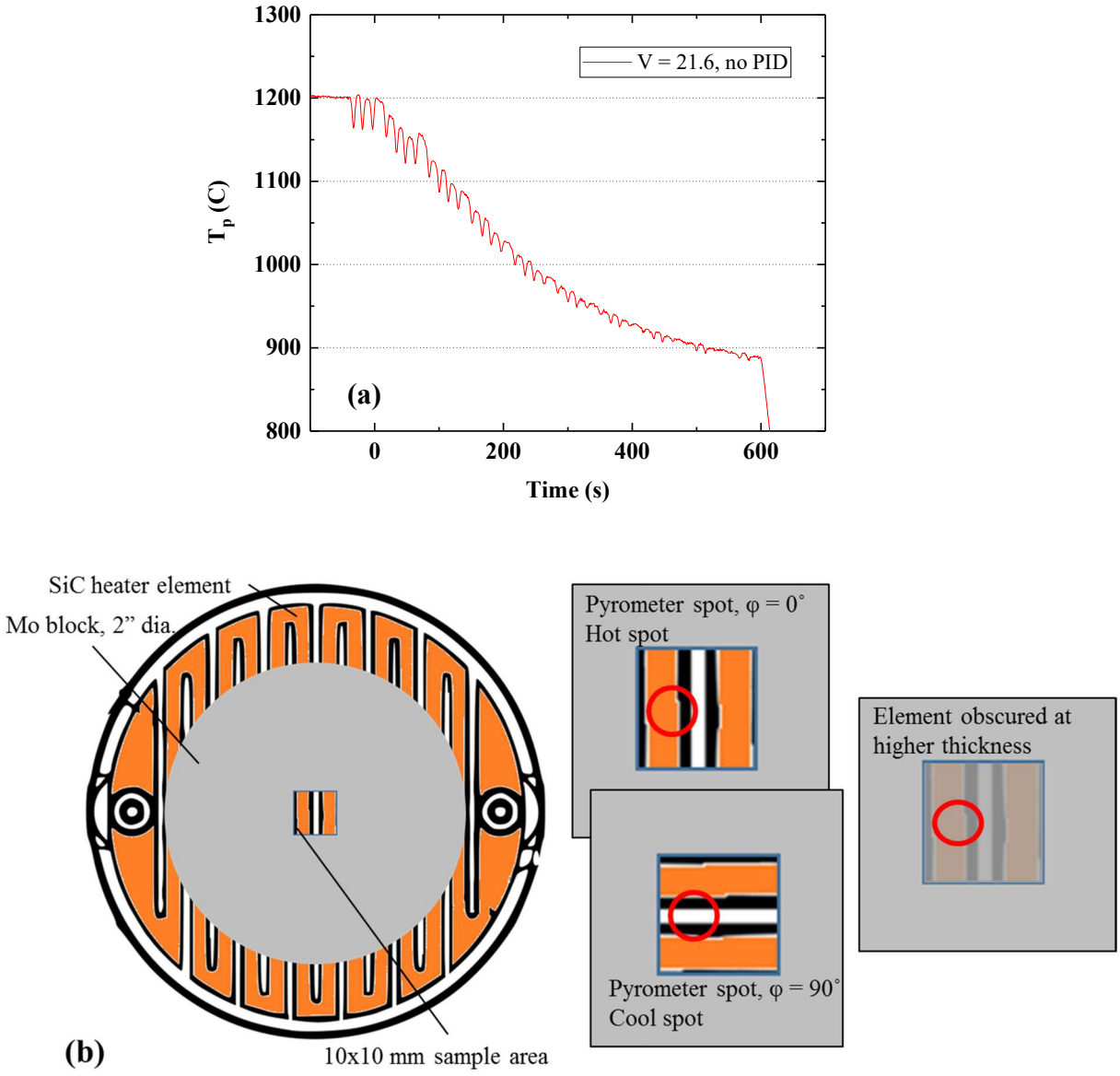

Figure 3-2: (a) the behavior of Tp during film deposition. (b) Schematic of the heater/sample configuration, visualizing the cause of oscillations in Tp and damping of oscillations during film growth.

It is difficult to reproduce this behavior from one film growth to the next, especially when the films can vary in composition. Changes in composition can contribute to small differences in emissivity, resulting in inconsistent T_p readings from which it is difficult to discern what conditions

have been kept constant. When growing films that are substantially thinner than the one in Figure 3-2, temperature does not saturate, leading to even higher uncertainty for thin films.

A hybrid method was adopted as a solution. The optical pyrometer was pointed at the substrate. In parallel, a small 0.5 mm K-type thermocouple was inserted into the Mo block to monitor the temperature of the block itself. Though the block is not tightly thermally coupled to the substrate, this is a way to monitor the total thermal energy flowing from the heating element. The reading from the thermocouple was fed into a PID loop controlled by an OMEGA CNi D16 temperature controller, which manipulated the duty cycle of the heater through a relay to maintain the Molybdenum block temperature (T_{Mo}) at a constant value. This setup is shown in Figure 3-3.

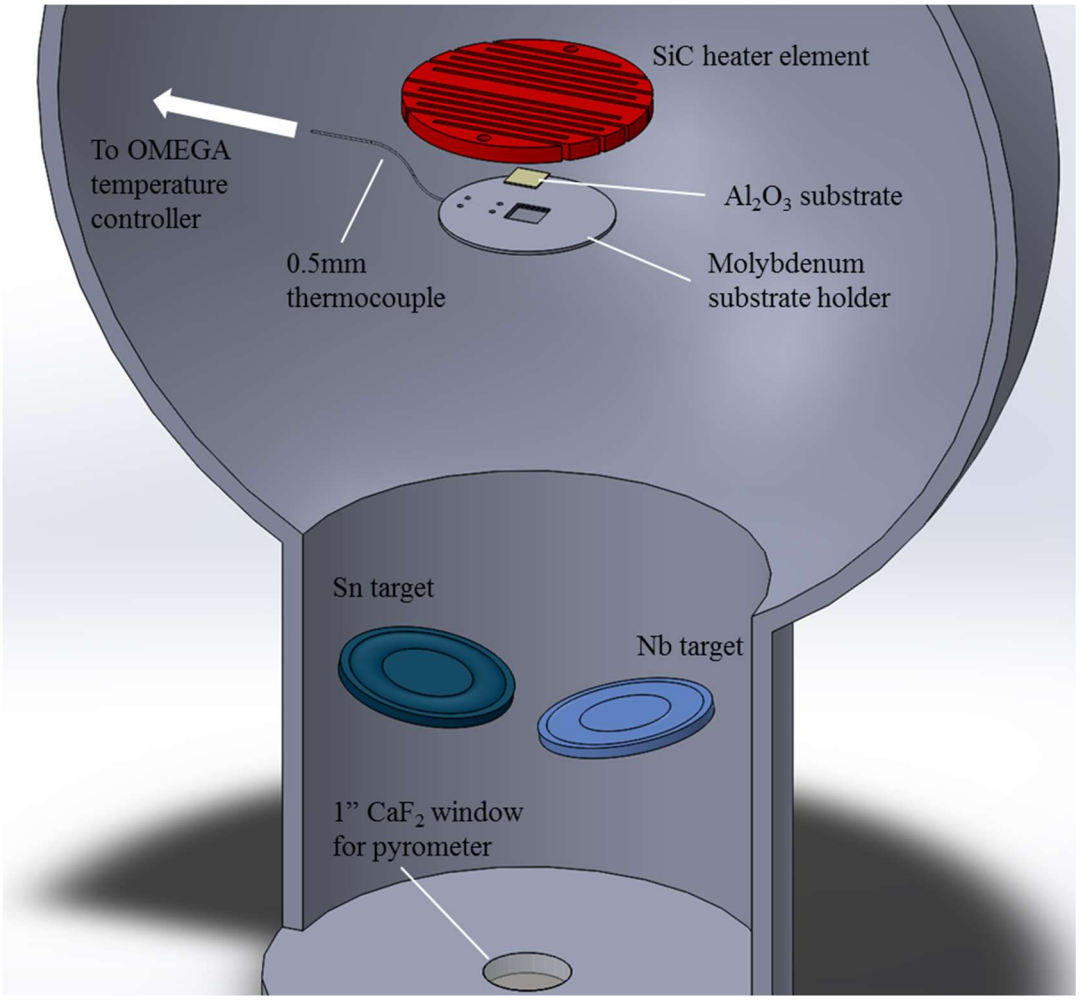

Figure 3-3: Chamber setup for monitoring both T_{Mo} and T_p.

With all other conditions fixed, Nb_3Sn films were grown at T_{Mo} = 800, 825, and 850 °C; this resulted in the T_p curves shown in Figure 3-4a. T_p curves follow the T_{Mo} setpoint, resulting in a final T_p at the end of 10-minute growth plotted in Figure 3-4b. This demonstrates that this method allows a degree of control over the heat transmitted to the film, even though T_{Mo} is not a direct reading of the substrate temperature.

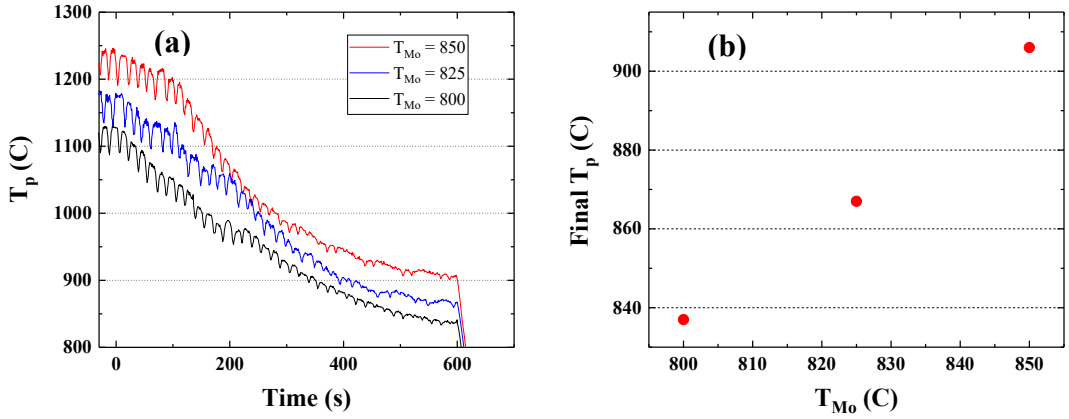

Figure 3-4: (a) T_p behavior for various setpoints of T_{Mo}. The ending T_p is plotted in (b), and appears linear with T_{Mo}.

When growing 2" wafers, this method presents some challenges. The wafer is situated where the Mo block would typically be. Because the block is no longer part of the system, there is no comparable place to situate the thermocouple; these films are grown with only a T_p reading as a way of regulating growth temperature. Because of this, they are necessarily different from the films grown with T_{Mo} regulation. The specifics and challenges of wafer growth are detailed in Chapter IV.

Armed with a method to tightly control growth conditions, we explored the effects of substrate choice and Sn flux on film composition and morphology. A variety of 10x10 mm samples were grown before any 2" wafer growths were undertaken.

3.1 Epitaxial relationship with Al_2O_3 and $LaAlO_3$

At the beginning of this project, the goal was to grow single-crystal films of Nb_3Sn on low-loss dielectric substrates. We experimented with several substrates and orientations in pursuing this goal. All of the films in this section on substrate orientation were grown at the same conditions, with T_{Mo} = 870 ˚C, Sn flux (r_{Sn}) = 1.5 Å/s, and Nb flux (r_{Nb}) = 0.7 Å/s.

3.1.1 R-plane Al_2O_3

The films grown using the radiative heater method have shown a high degree of crystallographic texture. When grown on R-plane Al_2O_3 substrates, these films are oriented with the (023) planes parallel to the substrate. XRD patterns on a 2-dimensional detector are shown in Figure 3-5a. The (012) reflections are present on either side of the q_{normal} line with equivalent intensity, revealing that two distinct in-plane orientations of (023) grains are present, with the [100] film direction oriented along the $[\bar{1}011]$ substrate direction. Equivalent intensity in (012) and $(0\bar{1}2)$ indicate that there is no preference in the system between these two directions. Figure 3-5b and Figure 3-5c show schematics of this epitaxial relationship from two different perspectives.

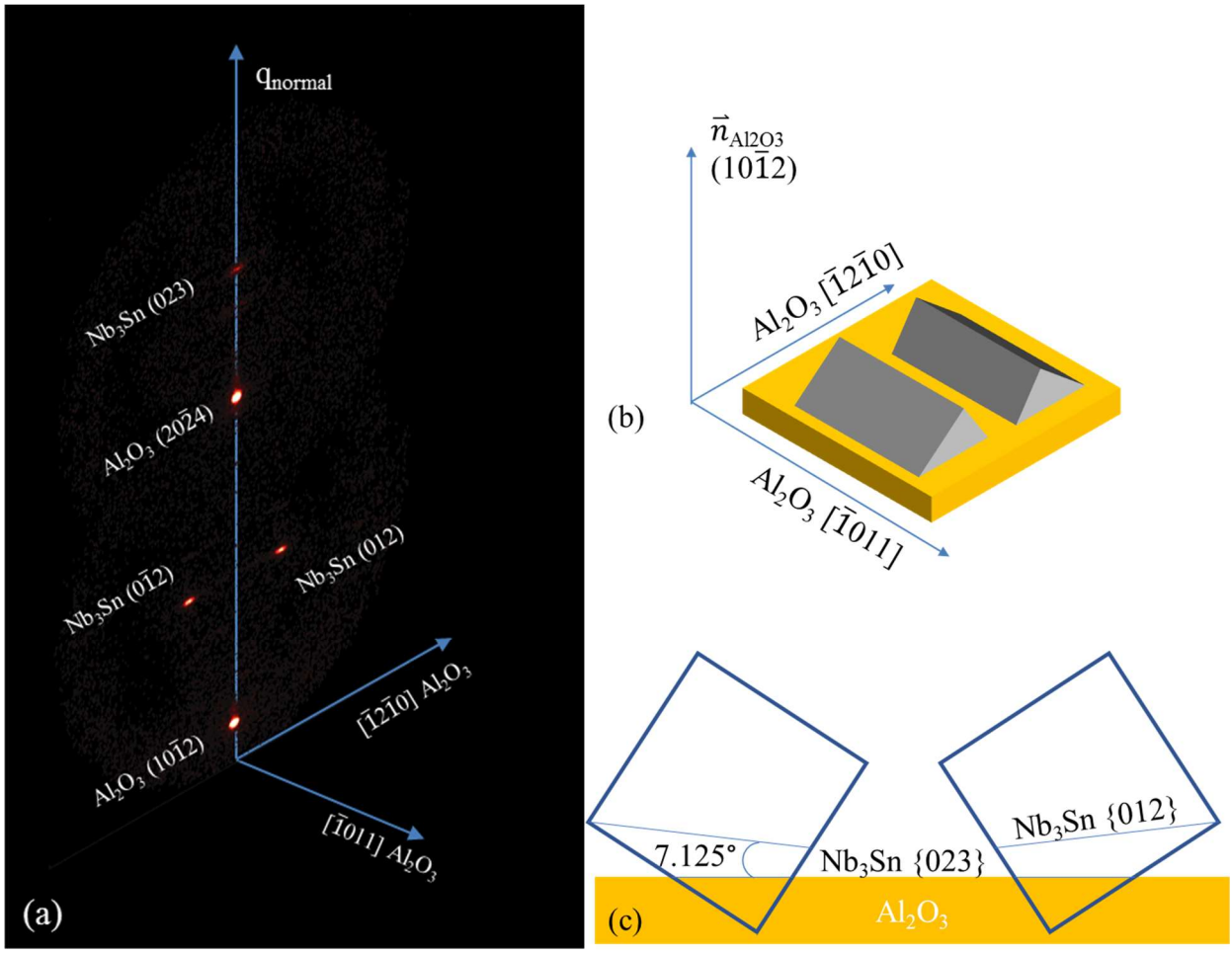

Figure 3-5: (a) 2D-XRD data on Nb_3Sn/R-Al_2O_3, visualized as a reciprocal space map. Nb_3Sn (012) peak is split, with each peak at $\chi = \pm 7.125$ degrees from q_{normal}. (b) 3D schematic of the epitaxial relationship between Al_2O_3 and Nb_3Sn in this system. Both possible grain orientations are represented. (c) 2D schematic, with blue boxes indicating the cubic unit cell of Nb_3Sn.

AFM images reveal that the grains are ridged, with the long axis of the grains aligned along the [100] direction of the Nb_3Sn, as shown in Figure 3-6. Sections of these images show that the faces of the grains are angled at ~7° relative to the substrate. This suggests that the faces are (012) planes, which are at an angle of 7.125° to the (023) plane around the [100] zone axis.

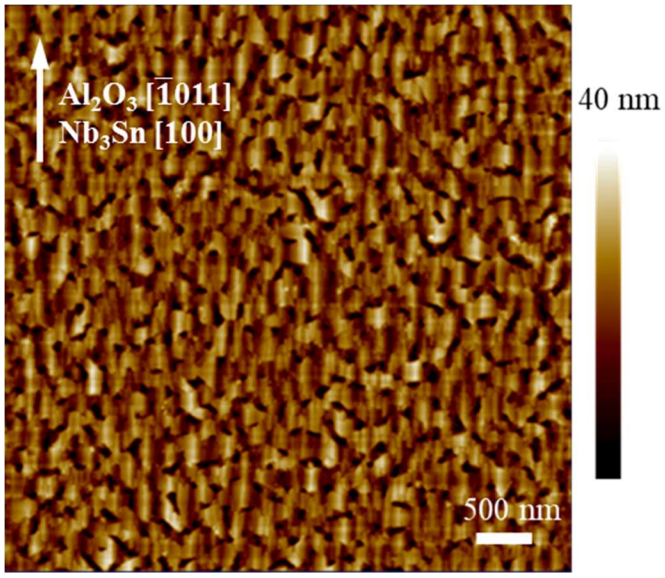

Figure 3-6: AFM image of Nb_3Sn/R-Al_2O_3. Ridged grains are aligned with [-1011] direction of Al_2O_3.

This is consistent with literature information on the R-plane surface of Al_2O_3 [37,38], visualized in Figure 3-7. The surface of the R-plane is composed of rectangular cells with periodicity of 4.76 Å in the [$\bar{1}2\bar{1}0$] direction and 5.13 Å in the [$\bar{1}$011] direction. The (001) spacing of Nb_3Sn is 5.29 Å, matching with the [$\bar{1}$011] spacing of Al_2O_3 with a 3% mismatch; this relationship of [100] Nb_3Sn to [$\bar{1}$011] Al_2O_3 matches what we see in the XRD and AFM data. The periodicity in the [032] direction of Nb_3Sn is 4.77 Å, leading to a remarkably small lattice mismatch of 0.3% in this orientation.

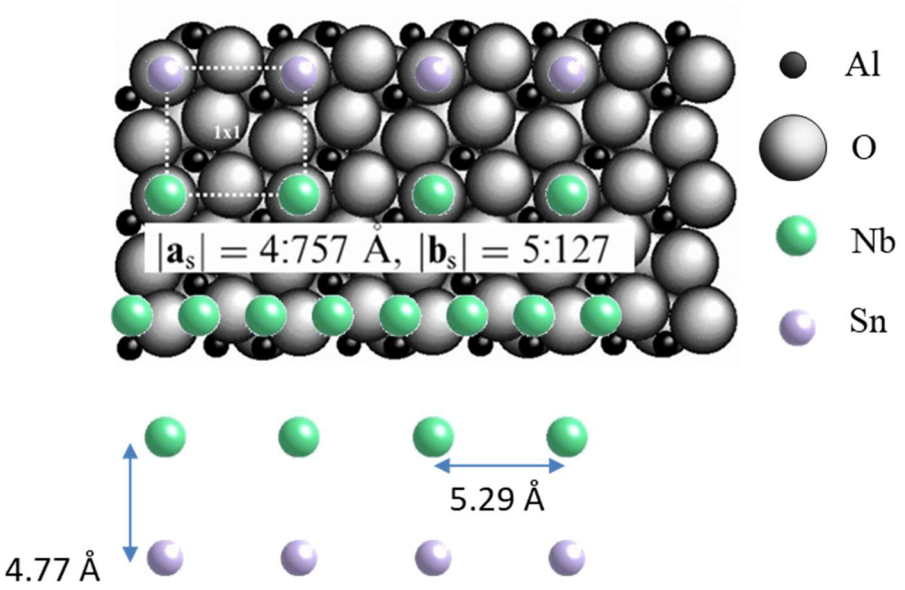

Figure 3-7: R-plane surface of Al_2O_3 and epitaxial relationship to Nb_3Sn (023). Al ions are represented in black, and O ions are light; overlaid Nb atoms are green, and Sn atoms are purple. Surface unit cell and lattice parameters are indicated. Figure adapted from [38].

This ridged structure of the grains leads to a high surface roughness, depending on the size of the grains, making true thickness of the film difficult to discern. Depending on growth conditions, roughness could range from 3.5 to 26 nm for superconducting films. For SRF and SIS applications, rougher films are not ideal, especially when the thickness of the film is a critical parameter in determining the vortex penetration field of the structure.

3.1.2 7 degree miscut R-plane Al_2O_3

We attempted to eliminate one of the two (023) crystal directions during growth by growing on Al_2O_3 with a large miscut. These substrates were R-plane oriented, with a 7.5 ˚ miscut toward $(11\bar{2}0)$. Ideally, this would increase the nucleation energy of $(0\bar{1}2)$ to the point where only (012) grains would form, leading to a single crystal film with no chasms between grains.

These expectations were only partially realized. Figure 3-8 sets low- and high-miscut films next to one another, and it is clear that miscut grains lead to much flatter surfaces without ridges,

suggesting that one of the (012) domains has been eliminated. However, there are still some large gaps between grains, suggesting the film is not a single crystal. This is confirmed by the XRD pattern (Figure 3-9), which again shows both (012) and ($0\bar{1}2$) domains present in the crystal, though the ratio in brightness is now 8:1.

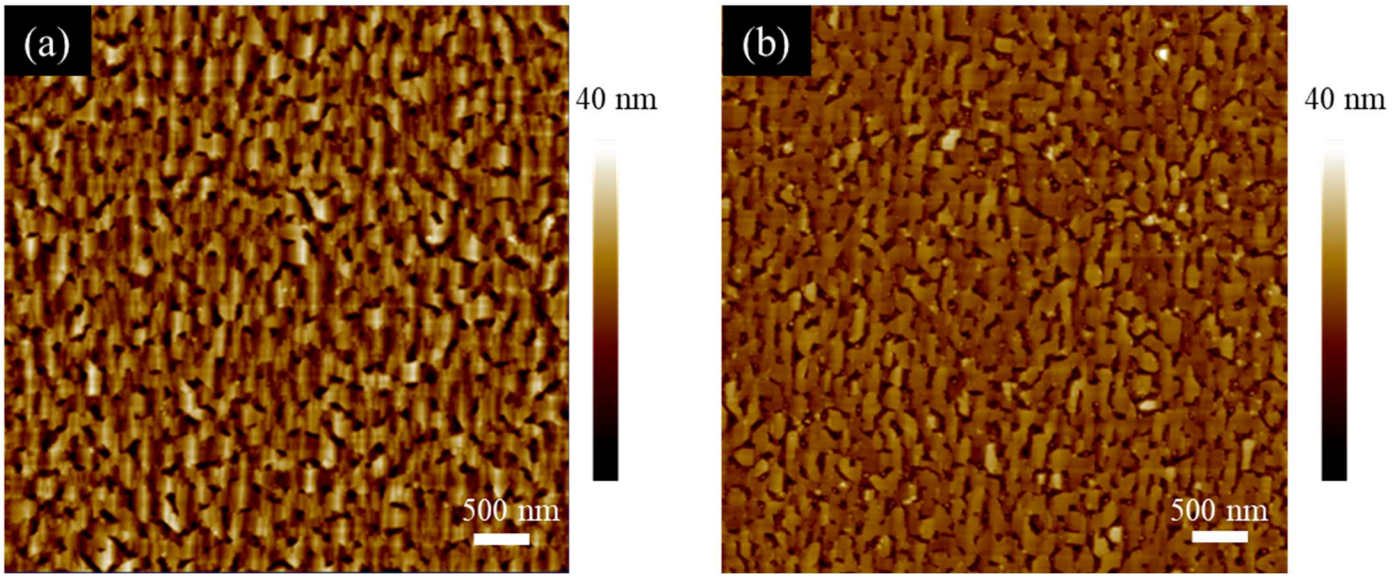

Figure 3-8: (a) Nb_3Sn film on low-miscut R-plane Al_2O_3. (b) Film grown under identical conditions on Al_2O_3 7-degree miscut from R-plane.

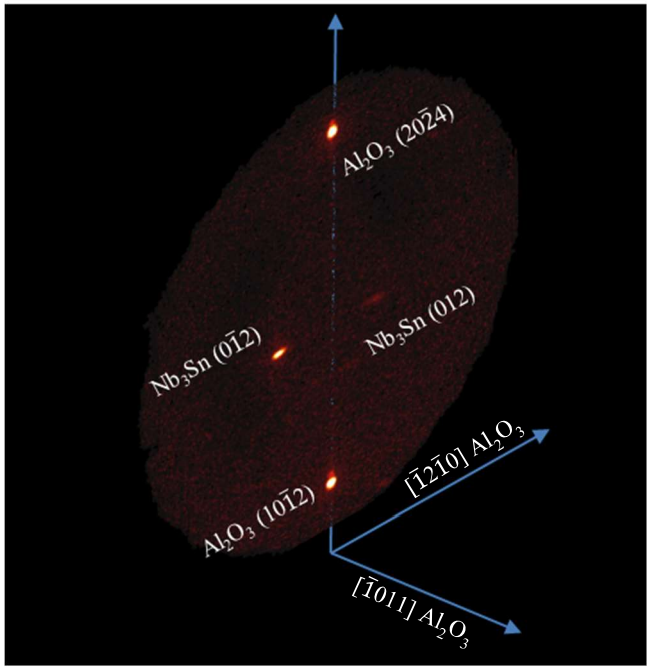

Figure 3-9: 2D-XRD scan of Nb_3Sn film on miscut R-plane Al_2O_3. One Nb_3Sn {012} orientation is clearly favored, but the other is not eliminated.

When comparing the transport properties two samples, one grown on low-miscut and one grown on the high-miscut R-plane, there is a clear difference. Both samples were grown at the same conditions, with T_{Mo} = 870 °C, r_{Sn} = 1.5 Å/s, and r_{Nb} = 0.7 Å/s. Their low-temperature DC sheet resistance is compared in Figure 3-10. The film grown on low-miscut Al_2O_3 has a much higher T_c and sharper transition width compared to the high-miscut substrate. This suggests two possibilities. The first is that the high-miscut film has a lower Sn content. This could be caused by a change in the rate at which Sn could react with the Nb during growth; since the surface morphology is different, this is a possibility. The more likely possibility is that the slightly different relationship between the substrate and the film leads to a coherent interface, which transfers strain into the film more efficiently in the high-miscut sample. Nb_3Sn is sensitive to strain, and many of the superconducting properties degrade with strain (e.g. critical field, critical current, DoS) [33,39].

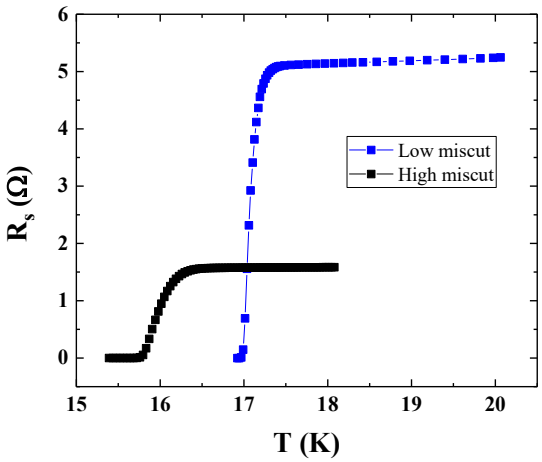

Figure 3-10: Superconducting transitions for films on low- and high-miscut R-plane substrates.

3.1.3 $(11\bar{2}0)$ Al_2O_3

We also grew Nb_3Sn films on $(11\bar{2}0)$ oriented Al_2O_3 substrates at the same conditions. This also led to textured films, with the (012) orientation parallel to the surface. This still leaves two possible grain orientations; the X-ray scans in Figure 3-11 show that the (023) peak has split into two, at a 7.125° angle from the substrate normal. This is the reverse of the orientation found in R-plane Al_2O_3. Since the brightest film peak lies in the same plane as the substrate, this orientation lends itself to point-detector scans much more easily.

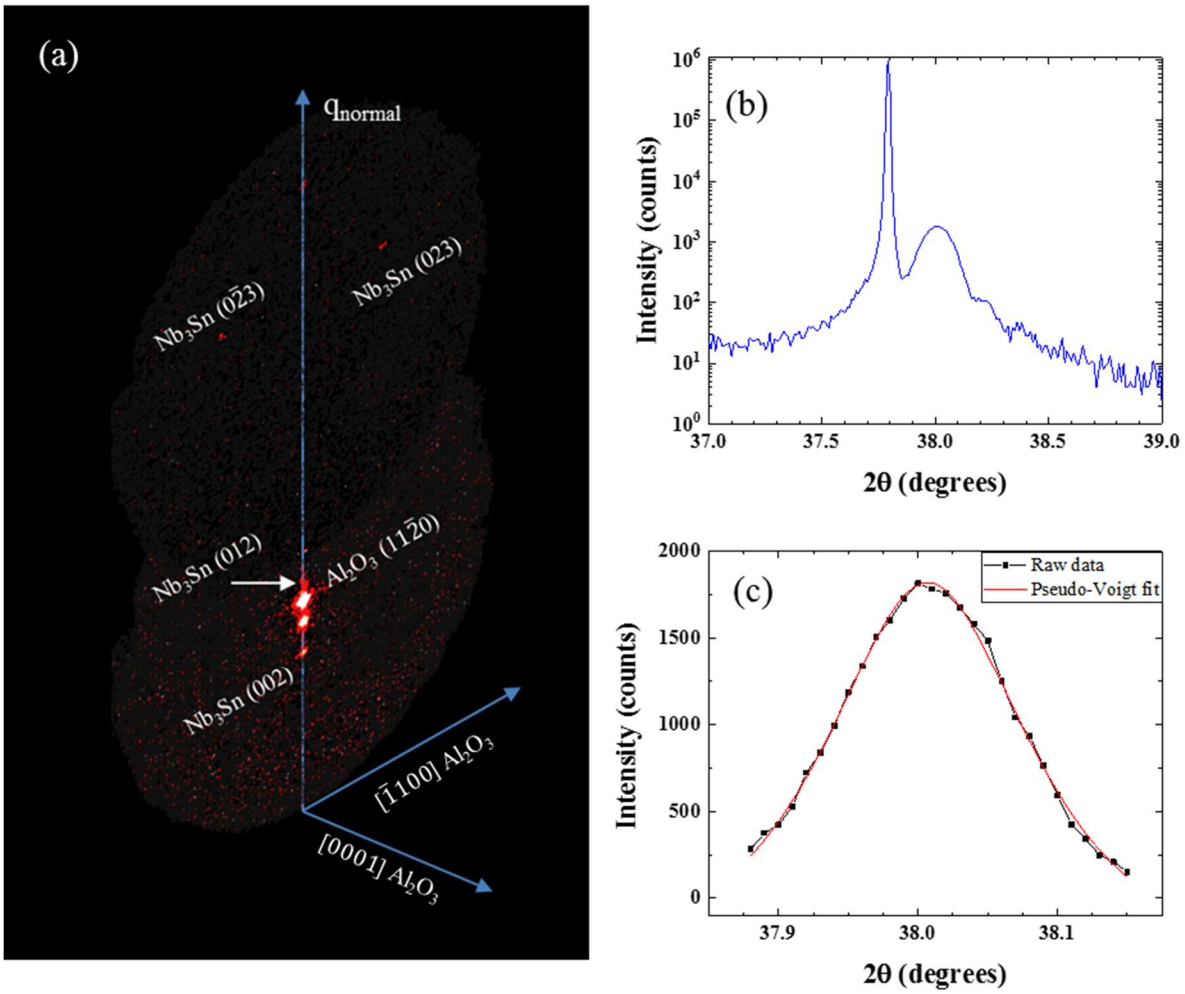

Figure 3-11: (a) 2D-XRD of Nb_3Sn on A-plane Al_2O_3. (012) plane is now a single point, and the (023) peak has split in turn. (b) point-detector scan of this sample around the (012) peak of Nb_3Sn, which is fit with a pseudo-Voigt peak function in (c).

Figure 3-11b shows such a scan, with the film peak immediately next to the substrate peak. The film peak is at 2θ = 38.007 °, which gives a plane spacing of 2.366 Å, or a lattice parameter of 5.2896 Å. The literature value of the bulk lattice parameter is 5.29 Å at 25% Sn, and decreases continuously across the single-phase region to 5.281 Å at 18% [33,40,41]. This indicates that, if strain plays a minimal role in shifting this peak position, these films are very close to stoichiometric.

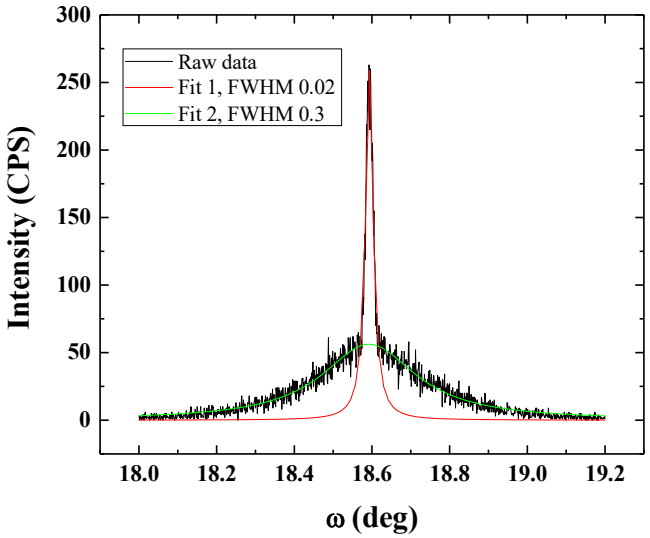

Figure 3-12: Rocking curve of the (012) peak of Nb_3Sn on A-plane Al_2O_3. It was fitted with two Gaussian peak functions, showing two clear contributions.

A rocking curve of the film peak (Figure 3-12) shows two contributions: a broad, low peak, fitted with a FWHM of 0.3 °, and a sharp peak with a FWHM of 0.024 °. This suggests that there is a strained layer at the interface between the Al_2O_3 and Nb_3Sn, and the film relaxes to the bulk value above this layer.

3.1.4 LAO (001)

$LaAlO_3$ (LAO) was the only cubic substrate we tested with these films. The (100) plane spacing of Nb_3Sn is roughly twice that of the (110) of LAO, making it a good candidate for (001)-oriented epitaxy of Nb_3Sn on an oxide. A film without grain boundaries and chasms would be ideal for studying the intrinsic properties of Nb_3Sn unhindered by the coupling and scattering that happens across grains; however, LAO has high dielectric losses compared to Al_2O_3, so it is unlikely to be used for SRF purposes. As such, it was only investigated here as a way to explore new possibilities for studying Nb_3Sn films.

As LAO is optically not transparent, the transmission of energy from the heater element to the film may not be identical to that of Al_2O_3. T_p for LAO samples begins at a slightly lower value

than in Al_2O_3 samples with identical T_{Mo} (Figure 3-13), suggesting some amount of radiation is filtered out by LAO. However, the ending T_p is identical, indicating that the heat transferred to the film is identical in both substrates when the film is present.

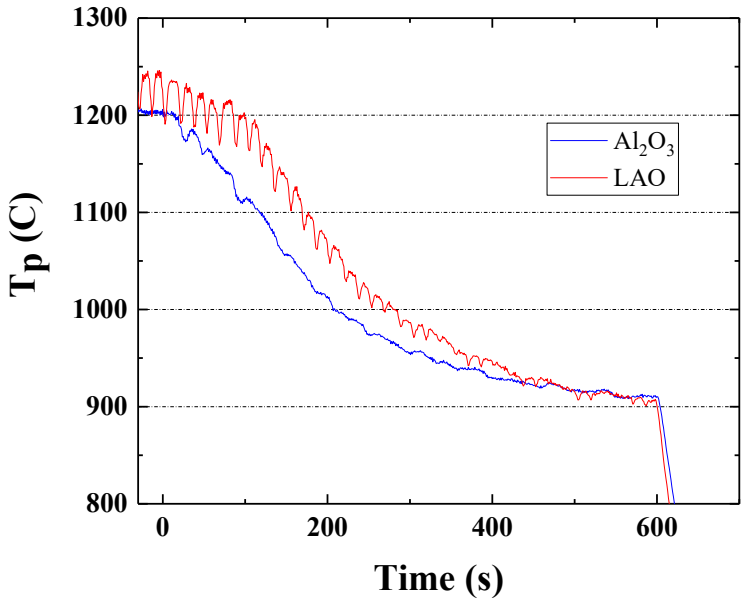

Figure 3-13: T_p during growth on LAO compared with growth on Al_2O_3. Starting Tp is lower due to some opacity in LAO, but ending T_p is identical.

These films are also highly textured, but are dominated by (001) oriented grains, as reflected in the 2D and 1D x-ray scans (Figure 3-14). (012) grains are also present, though at a lower intensity than the (001) grains, and a faint trace of (112) reflections are visible. These results suggest that, with tighter control, purely (001) single-crystal films could be achieved, in which

intrinsic properties could be studied. Given the constraints of this project, however, this was not pursued further.

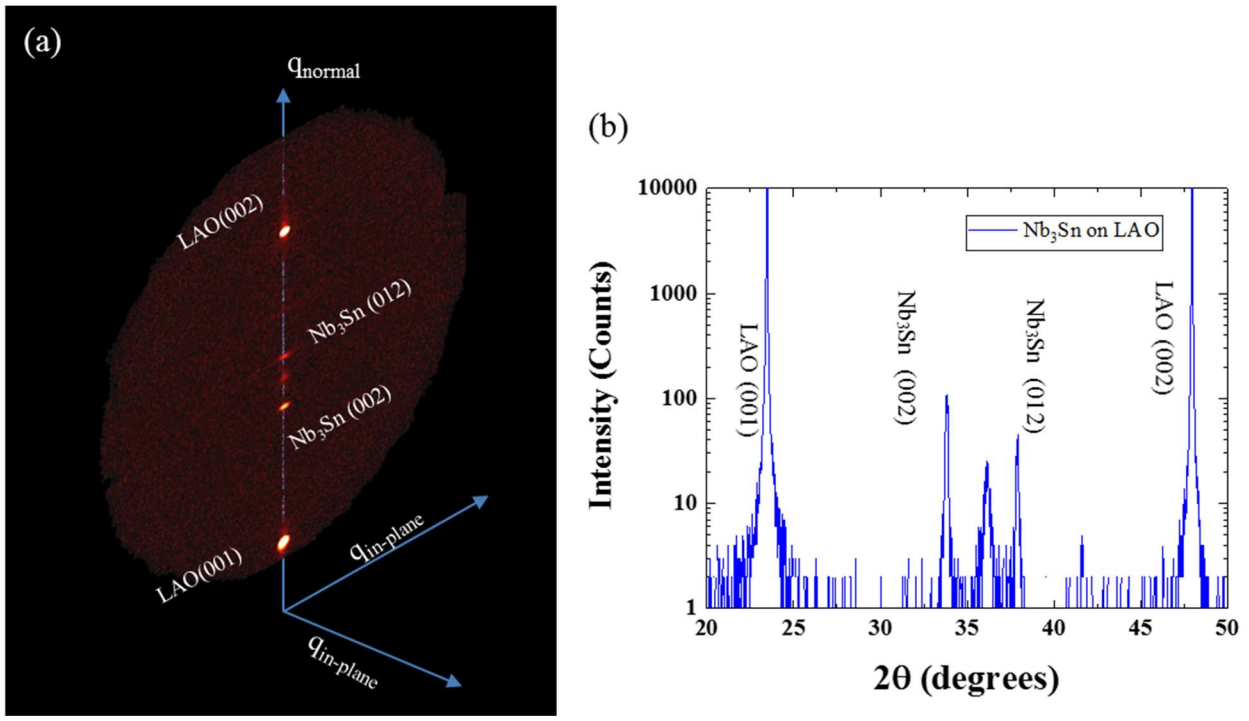

Figure 3-14: (a) 2D-XRD of Nb_3Sn on LAO(001). Nb_3Sn (002) is the strongest peak, but (012) is also present, along with a peak between the two that does not belong to either LAO or Nb_3Sn. (b) Point-detector scan of the same sample.

3.2 Parasitic phase

The peak that appears between the Nb_3Sn (002) and (012) peaks does not belong to either LAO or Nb_3Sn, and appears in films grown on A-plane Al_2O_3 as well. Figure 3-15a superimposes the XRD scans of films grown on these two substrates, showing that the peaks align, and are likely the same phase. One possibility is that O is diffusing into the Nb from the substrate, forming Nb_2O_5.

However, when Nb_3Sn is grown on CaF_2 substrates, this peak is still present (Figure 3-15a,b), ruling out the possibility of O supply from the substrate. This indicates that it is more likely that the parasitic phase is growing with the film, incorporating only Nb and Sn. $NbSn_2$ is a possible candidate.

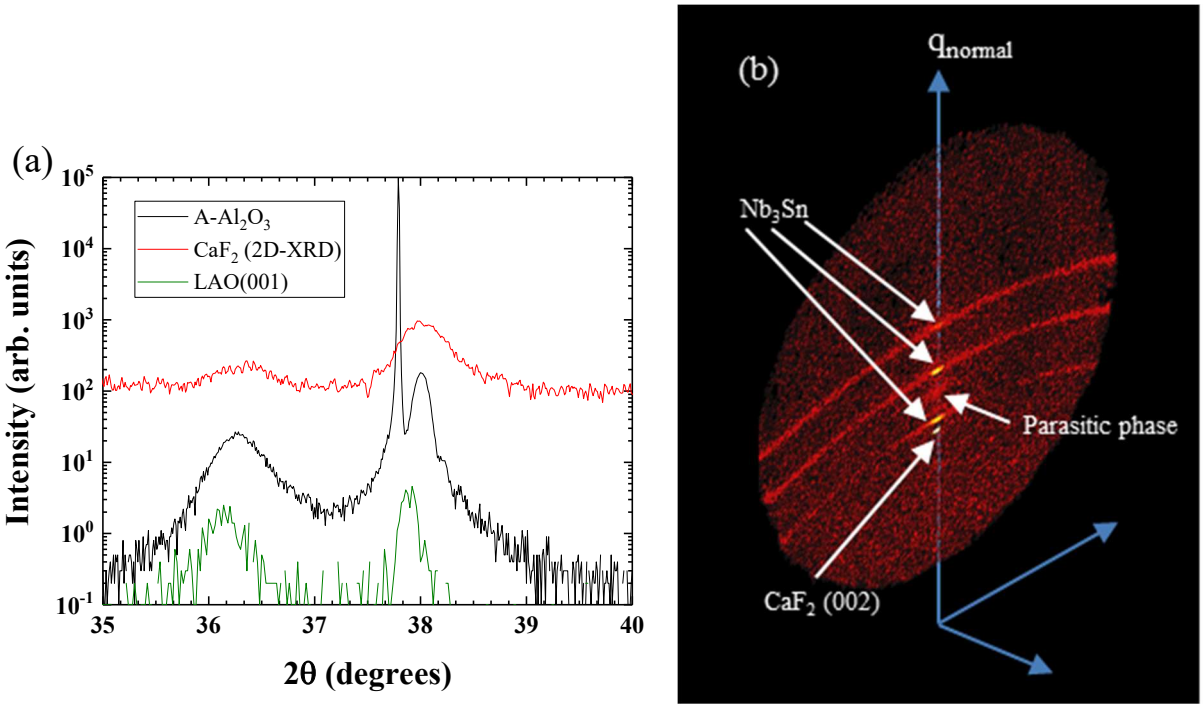

Figure 3-15: (a) XRD patterns of Nb_3Sn grown on A-Al_2O_3, LAO(001), and CaF_2(001), all of which show the parasitic phase peak. (b) 2D-XRD of Nb_3Sn on CaF_2(001). Parasitic phase between Nb_3Sn (002) and (012) is still present, ruling out the possibility that oxygen diffuses from the substrate into the film during growth to form the parasitic phase.

However, when Nb_3Sn is grown on R-plane Al_2O_3, parasitic peaks do not appear, as evidenced in X-ray scans in Figure 3-9 and Figure 3-5. It is possible that the grains of this phase chooses a different direction to point in, and simply do not appear in the 2D-XRD images. With this information, films were optimized and measured on R-plane substrates.

CHAPTER 4

Stoichiometry Control of Films

R-plane substrates were used for the bulk of the detailed work done on Nb_3Sn films. As superconducting properties are strongly dependent on Sn content [39], we conducted a study on the dependence of the DC and RF properties of these films on the Sn flux during growth.

4.1 The "Phase-Locking" Approach to Growth

A previous study detailed e-beam evaporation of Nb_3Sn films and the tendency of Sn-excess films to "lock on" to the Nb_3Sn phase boundary at high temperatures [25,26]. This is due to the nature of the two-phase region in the Nb_3Sn phase diagram (Figure 4-1) at temperatures above 930 ˚C and Sn in excess of 25%, where the only stable phases are solid Nb_3Sn and liquid Sn. At these temperatures, pure Sn has an extremely high vapor pressure (Figure 4-2), which equates to an erosion rate on the order of 1-10 Å/s. In these conditions, the growth process can be conceptualized with the equation

$$r_{sputter} = r_{reaction} + r_{evaporation} \qquad \text{[Eqn. 5]}$$

Where $r_{sputter}$ is the rate at which sputtered Sn flux is delivered to the film, $r_{reaction}$ is the rate at which deposited Sn reacts with Nb, and $r_{evaporation}$ is the rate at which unreacted Sn re-evaporates from the film surface. As long as $r_{sputter} - r_{reaction}$ is lower than the erosion rate at a given temperature (8 Å/s at 930 °C), the film composition cannot be higher than 25% Sn, where pure Sn segregates from the Nb_3Sn matrix.

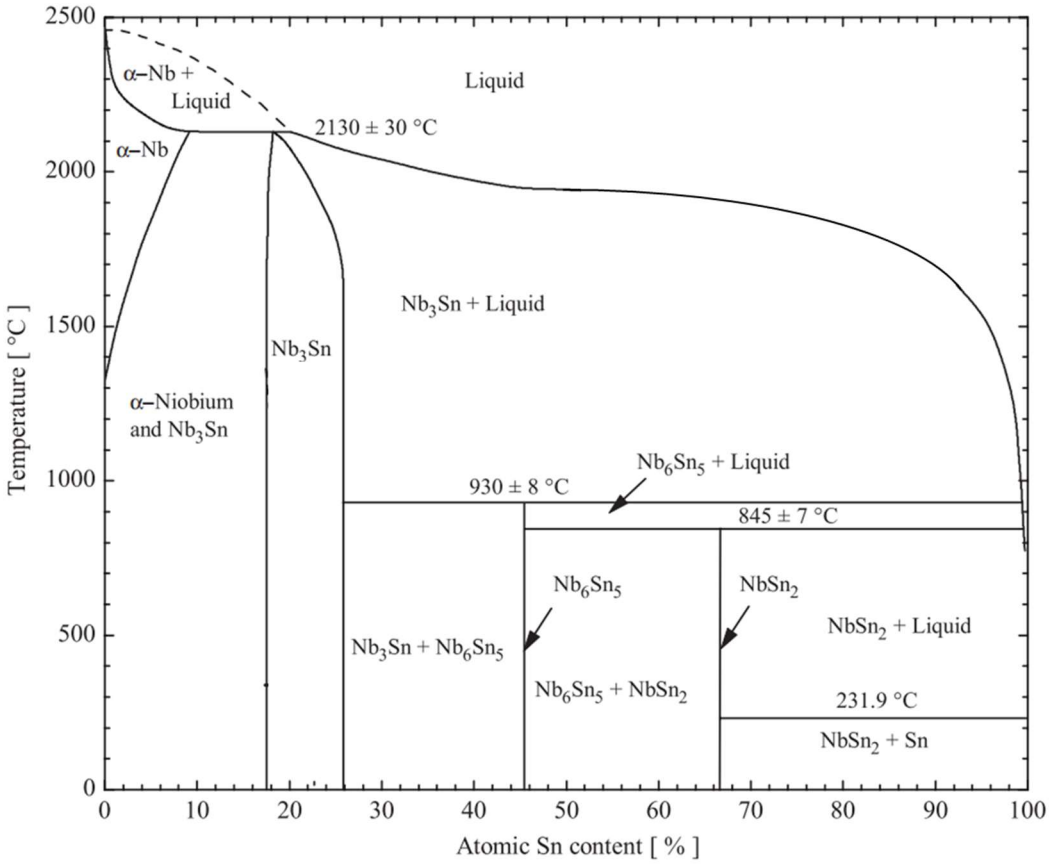

Figure 4-1: Phase diagram of Nb-Sn system. Above 930 ˚C, only Nb_3Sn and liquid Sn are stable.

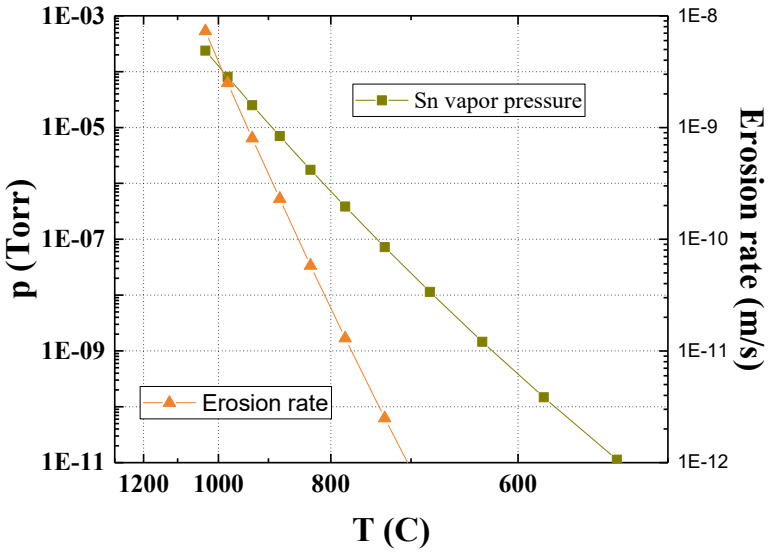

Figure 4-2: Vapor pressures and the corresponding erosion rate of Sn. At temperatures above 900 ˚C, Sn evaporates at rates close to 10 Å/s.

This makes it theoretically possible to grow stoichiometric Nb_3Sn over a wide growth window of Sn flux. This also leaves open the possibility of manipulating Sn content continuously within the single-phase region of Nb_3Sn, a goal which was not pursued in past studies. Sn-deficient Nb_3Sn can produce Nb_{Sn} defects, which increase normal-state scattering in the metal and reduce the mean free path l_{mfp}. Some theoretical calculations show that a local minimum in R_s can be found at $l_{mfp} \sim 0.5\xi_0$ [42]; if adjusting Sn content has a strong effect on l_{mfp}, we may be able to test these calculations and the suitability of Nb_3Sn for SRF cavity coatings. For these films, Nb flux was fixed at 0.7 Å/s, while Sn rate was varied according to the values in Table 4-1. Target thickness of all films was 60 nm.

Table 4-1: Growth conditions for films explored in this section. r_{Nb} and T_{Mo} are kept constant while r_{Sn} is varied across a wide range.

Nb rate	Sn rate	T_{Mo}	Nominal at% Sn
0.7	0.4	870	22
0.7	0.8	870	46
0.7	1.0	870	59
0.7	1.5	870	68
0.7	2.0	870	74
0.7	2.5	870	78

4.1.1 Surface roughness

Surface morphology of films grown at various Sn flux rates was strikingly different. Figure 4-3 shows the AFM images of samples grown at 0.8 and 1.5 Å/s Sn. The scales (both in-plane and vertically) are identical, emphasizing the dramatic change in roughness at higher Sn flux.

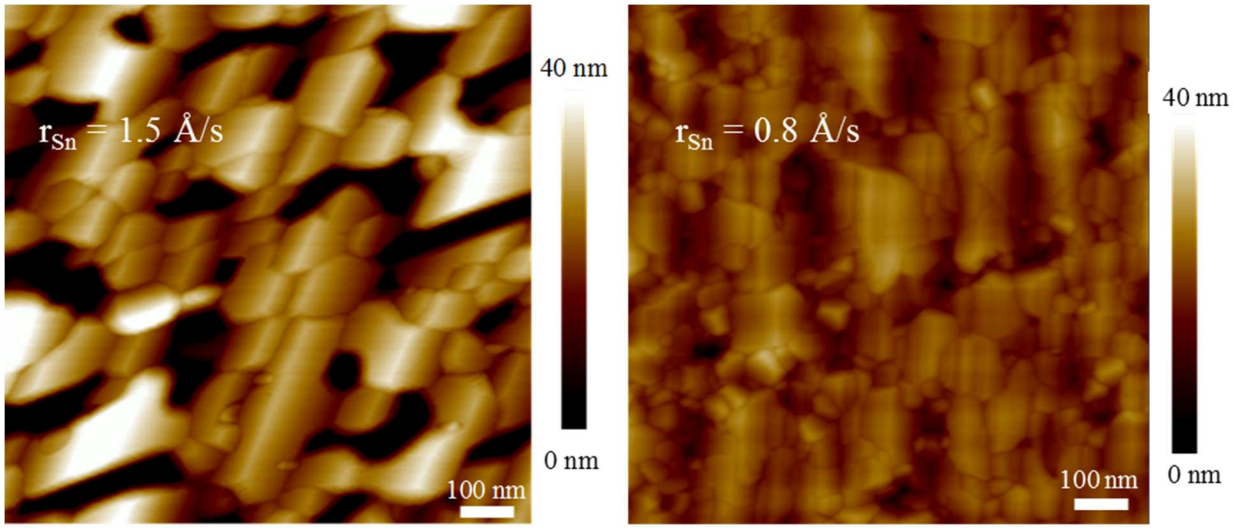

Figure 4-3: AFM images of films grown at r_{Sn} = 1.5 Å/s (left) and 0.8 Å/s (right). Height scales and in-plane scales are identical.

Figure 4-4 plots RMS roughness of films against the Sn flux. There appear to be two regimes: at low flux (under 1.0 Å/s), roughness is below 4 nm, and the films do not have large gaps in them. However, at higher r_{Sn}, roughness increases dramatically to 10-15 nm, and appears to increase monotonically with Sn flux. This jump in roughness coincides with a saturation in T_c as plotted in the same figure, suggesting that Nb_3Sn is stoichiometric in the high-Sn films and excess Sn re-evaporates. The mechanism for how excess Sn contributes to surface roughness has not been studied in these films.

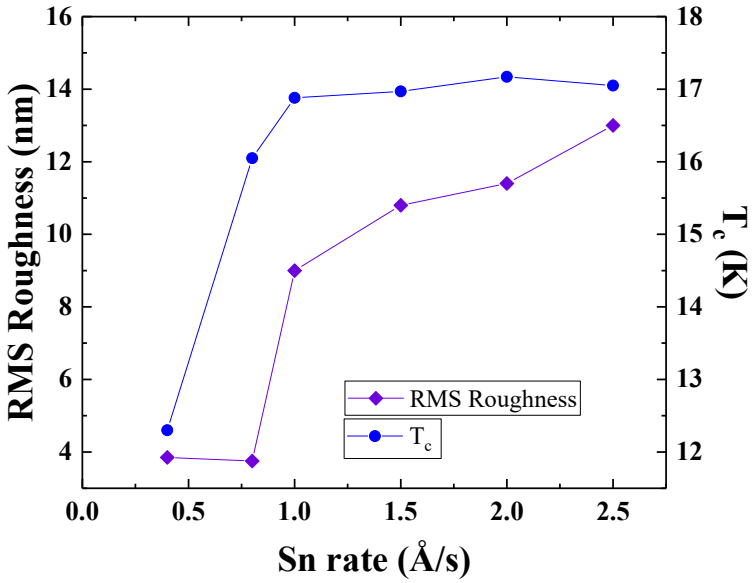

Figure 4-4: T_c and RMS roughness of films vs. r_{Sn}. At low r_{Sn}, roughness is low, but above r_{Sn} = 1.0 Å/s, roughness increases monotonically.

4.1.2 DC Properties

The sheet resistance of these films was measured by a 4-point probe in a cryostat. A sample curve is given in Figure 4-5. T_c is taken as the temperature at which the sheet resistance R_s first crosses 1% of the value at 18 K; ΔT_c is the distance between T_c and the intersection of the lines formed by the normal state and the transition. T_c and ΔT_c are plotted against Sn flux in Figure 4-6. At low flux, T_c is far below the bulk value of Nb_3Sn, but well above that of Nb. ΔT_c is sharp, at 0.4 K; this suggests that this film is homogeneous, with a Sn content somewhere between 17 and

25 %. With increasing Sn content, T_c rises rapidly and saturates at around 1.0 Å/s. ΔT_c follows this trend, decreasing from 0.4 K at low flux and saturating at 1.0 Å/s. Further Sn flux does not seem to strongly affect T_c or ΔT_c. This suggests that this is the "phase-lock" or absorption-controlled region explored by Allen et al., where excess Sn simply re-evaporates from the film surface during growth.

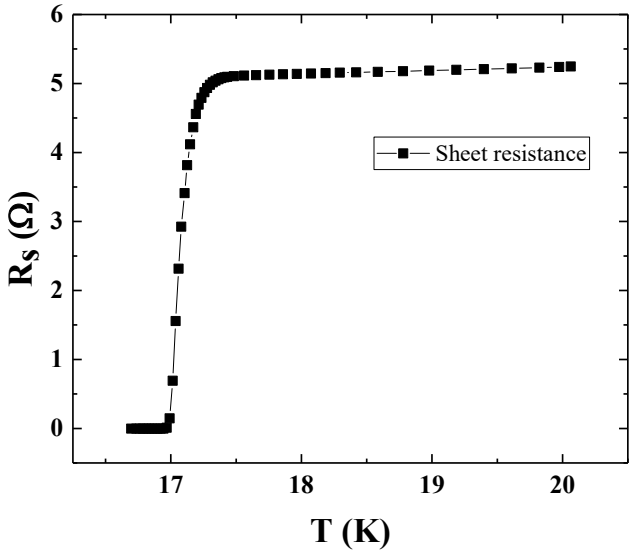

Figure 4-5: a sample superconducting transition curve for Nb_3Sn. T_c, ΔT_c, and RRR are determined from these curves.

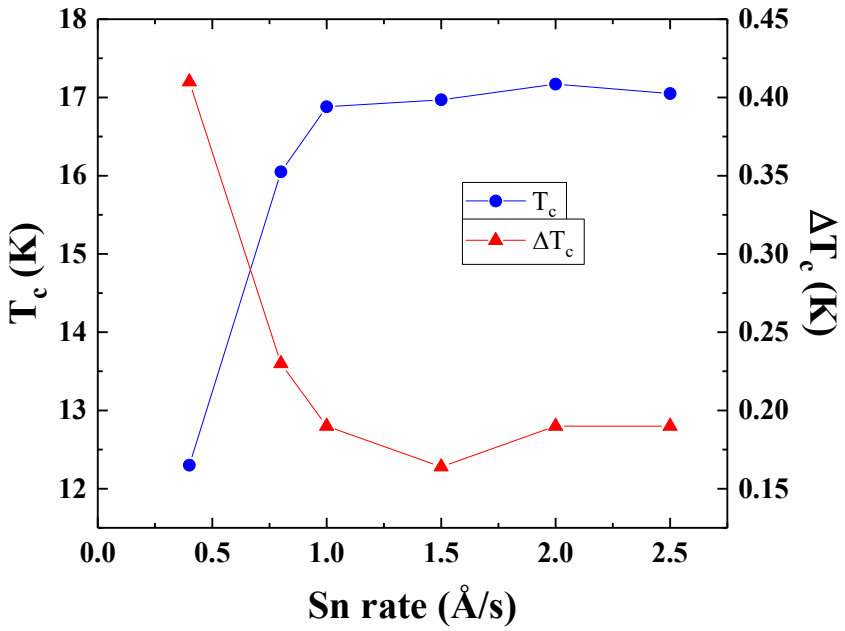

Figure 4-6: T_c and ΔT_c plotted against r_{Sn}. Saturation in both seems to occur above $r_{Sn} = 1.0$.

The residual resistivity ratio (RRR), calculated as $R_s(300K)/R_s(18K)$, gives a picture of the quality of the metallic state of the films. Thermal scattering is reduced between room temperature and 18 K; if thermal scattering is a large contribution to resistance in the metallic state, this is reflected in a larger RRR. On the other hand, if temperature dependence of resistance is small and RRR is small, this indicates that scattering is dominated by crystalline defects or impurities.

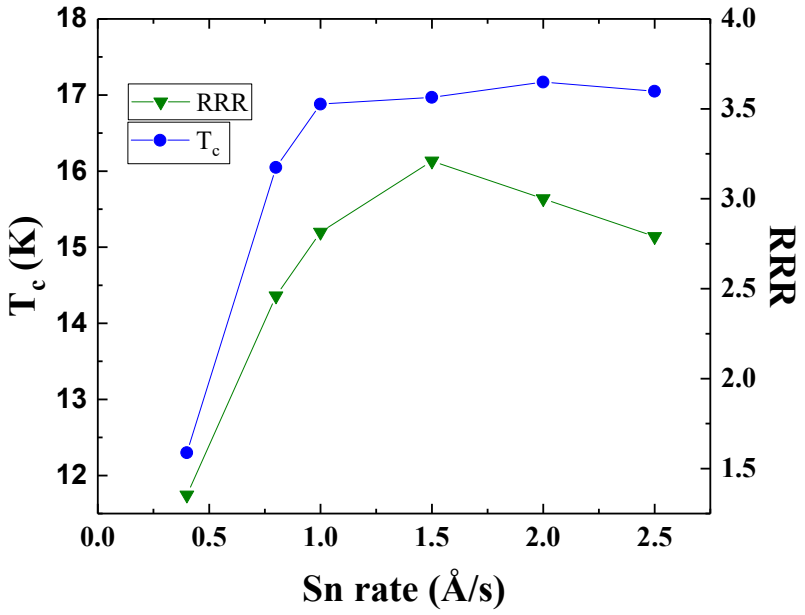

Figure 4-7: T_c and RRR plotted against r_{Sn}. Unlike the other properties, RRR does not saturate, instead reaching a peak around r_{Sn} = 1.5, and declining at higher flux. This could be due to impurities in the Sn affecting the Nb_3Sn more strongly at high r_{Sn}.

RRR of the Nb_3Sn films is predictably low at low Sn flux, where we expect a large number of Nb_{Sn} substitutional defects to cause scattering. RRR rises with r_{Sn} up to 1.5 Å/s, where it seems to reach a peak. At higher flux, there seems to be a slight dropoff. This could be due to a number of factors. One possibility is tied to the roughness of the film: at higher flux, film roughness rises monotonically, as presented above. When roughness is high, some parts of the film thickness sampled by the 4-point measurement is lower, leading to the possibility that surface scattering contributes to sheet resistance proportionally more.

Alternatively, it is a possibility that trace non-Sn impurities in the Sn flux are being left behind in larger quantities when Sn flux is higher. The Sn target is 99.99% pure, but all excess Sn evaporates and leaves behind the contaminants. At higher Sn flux, more total material is deposited, but the same amount of Sn is incorporated into the film, leaving a higher amount of contaminants to act as scattering sites. In this scenario, non-thermal scattering is dominated by Nb_{Sn} defects at

low Sn content, and by a higher concentration of impurities at high Sn flux. The 1.5 Å/s sample seems to be the optimum point, where Nb_{Sn} defects and impurity scattering sites are both at their minimum.

4.2 STM Density-of-States Measurements

To provide a complementary set of data to the electrical measurements, a film with r_{Sn} = 1.5 Å/s was measured with scanning tunneling microscopy (STM). The primary expected result of these measurements is to extract a density of states (DoS) spectrum for these films. According to BCS theory, the DoS of a superconductor below T_c can be described with [6]

$$N(E) = Re\left[{|E|}/{\sqrt{(E^2 - \Delta^2)}} \right] \qquad \text{[Eqn. 6]}$$

However, finite quasiparticle lifetime effects and other nonidealities introduce a distortion to this shape described by the Dynes parameter Γ modifying the BCS formula [43,44]:

$$N(E) = Re\left[{E - i\Gamma}/{\sqrt{(E - i\Gamma)^2 - \Delta^2)}} \right] \qquad \text{[Eqn. 7]}$$

When $\Gamma = 0$, this returns the BCS formulation for DoS. This distribution is plotted for various values of Γ/Δ in Figure 4-8.

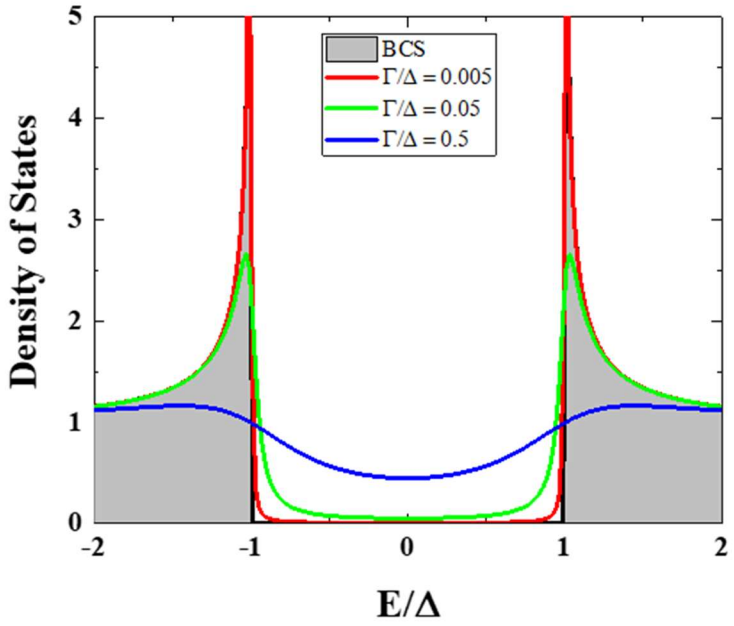

Figure 4-8: Density of states near E_F, as predicted by BCS theory, for various values of the modifying Dynes parameter Γ.

R_s is determined in part by the quasiparticles thermally excited above the superconducting gap; in ideal superconductors, this can be mathematically determined by using the BCS DoS and the Fermi distribution. However, the distorted DoS introduces quasiparticles into the gap. This leads to an additional contribution to R_s that is not described by the BCS theory. By probing the DoS directly through STM, it is possible to correlate any temperature-independent portion of R_s from RF characterization to the presence of quasiparticles in the gap.

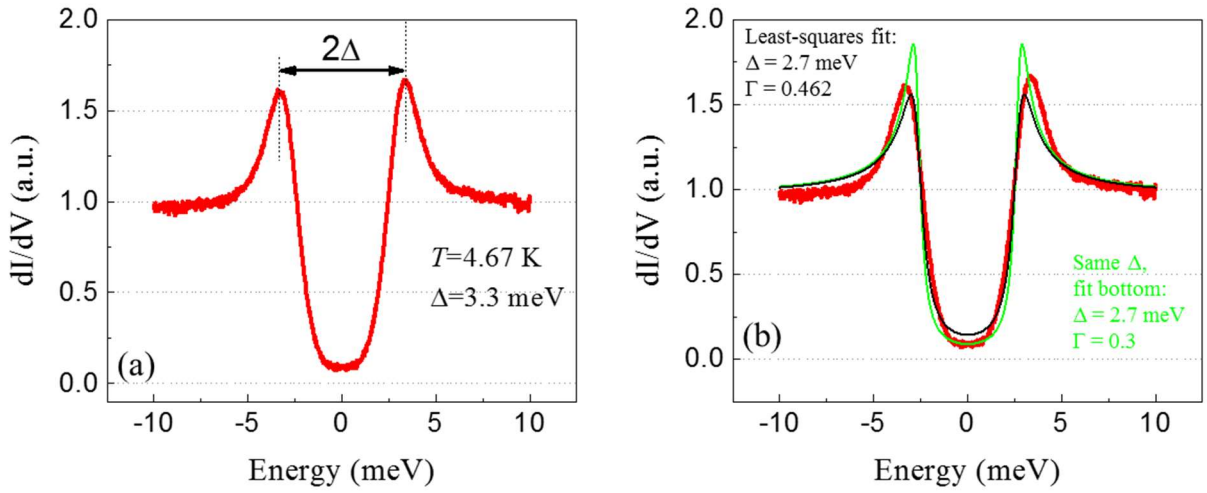

Figure 4-9: Raw data from STM DoS measurement (a), with peak-to-peak gap of 3.3 meV. Data is fit in (b), where least-squares fitting to the Dynes formula gives Δ = 2.7 meV and Γ = 0.462. Γ = 0.3 (green) fits the bottom of the curve more closely.

Figure 4-9 shows the fits to a dI/dV measurement by STM for the center of a Nb_3Sn grain. The peak-to-peak size of the gap in the raw data appears to be 3.3 meV, but fitting to the Dynes model reveals the true gap is somewhat smaller, at 2.7 meV. There appears to be an additional contribution to the shape that is not fully described by the Dynes formula, as least-squares fitting (shown in black, Γ = 0.462 meV) does not match the shape of the raw data near the peaks, and overestimates the number of states in the middle of the gap. Using the same gap size and changing Γ to 0.3 meV brings the fit curve through the raw data in the middle of the gap, at the expense of the fit everywhere else.

For temperatures $k_BT \ll \Delta$, it can be shown that the contribution of the in-gap to the residual surface resistance R_i at low temperatures is

$$R_i = \frac{\mu_0^2 \omega^2 \lambda^3 \Gamma^2}{2\rho_n(\Delta^2 + \Gamma^2)} \qquad \text{[Eqn. 8]}$$

Where μ_0 is the permeability of free space, ρ_n is the normal-state resistivity, and ω is the operating frequency of the cavity (1.3 GHz in most applications) [42]. λ for Nb_3Sn is estimated at 120 nm in the dirty limit, and ρ_n is 3.0×10^{-7} Ω-m in films grown at $r_{Sn} = 1.5$. For $\Delta = 2.7$ meV and $\Gamma = 0.462$, this gives $R_i = 8.6$ nΩ, and for $\Gamma = 0.3$ $R_i = 3.7$ nΩ. This compares well with $R_i \approx 10$ nΩ for large-grained Nb cavities [45]. There are other possible contributions to R_i in RF cavity geometry measurements, but the contribution from in-gap states is comparable to that measured in the best Nb cavities.

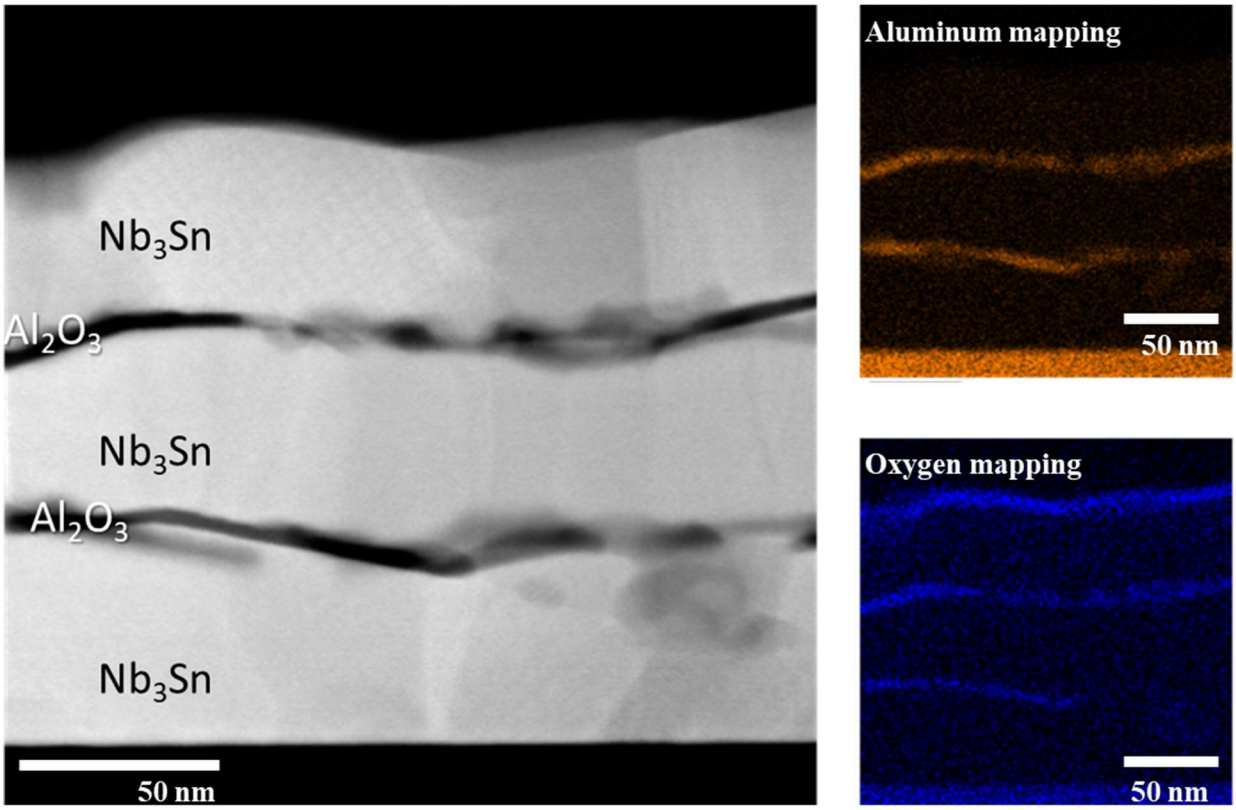

Figure 4-10: Cross-sectional TEM micrograph and EDS compositional mapping of Al and O from a multilayer heterostructure (described in Ch. 6). The oxide layer is evident on the surface, and does not correspond to Al_2O_3 as the rest of the oxide layers do.

Compositional data from TEM measurements on multilayer heterostructures show that there is an oxide layer ~5 nm thick at the surface of these films, as shown in Figure 4-10. Previous STM studies on Nb conclude that oxides on the surfaces of cavities can give rise to magnetic

scattering of the quasiparticles, degrading the surface resistance [13,46,47]. A similar mechanism could be a contributor to the deviation from a DoS that is described by the Dynes formula in the Nb_3Sn films. Furthermore, the DoS measured by STM only samples this surface oxidized region. Below the oxide layer (but well within $\lambda \approx 120$ nm of the surface), it is likely that the DoS is much sharper. As such, the R_i estimate calculated above is likely an upper bound for these films.

STM work done on thick Nb_3Sn films grown by reacting vapor-phase Sn with Nb cavities show considerably lower Γ/Δ ratios averaging 0.035, compared to $\Gamma/\Delta = 0.11\sim0.17$ in our films [48]. This could be due to the much higher reaction time and temperature used in the Sn vapor diffusion method, which leads to better stoichiometry and fewer scattering sites. However, the Γ/Δ ratio in our films compares favorably with that seen in Nb.

4.3 RF properties

To characterize the RF properties of these films, each was patterned by contact lithography and Ar ion milling into a co-planar waveguide (CPW) with resonant frequency ~3 GHz, using the mask shown in Figure 4-11a. These were diced into 6.25x6.25 mm dies and wirebonded to leads and a measurement box, shown in Figure 4-11b. By measuring the transmitted energy S_{21} on RF excitation at 3 K around the resonant frequency with a network analyzer, it is possible to extract the loaded quality factor Q_L for the resonators. This was used to estimate the surface resistance in Nb_3Sn at each composition.

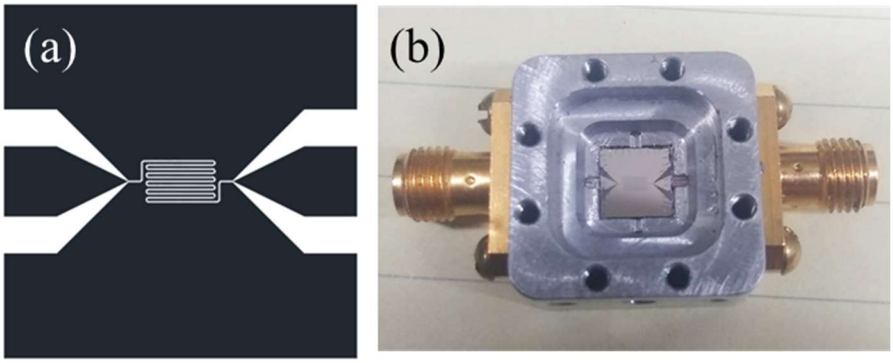

Figure 4-11: (a) RF co-planar waveguide mask used for characterizing these films. Dark regions represent Nb_3Sn. Pads at either end are capacitively coupled to the resonator in the center. (b) Resonator, diced and wirebonded to an aluminum characterization box equipped with SMA leads.

Of the six samples, only three showed resonant peaks when measured. This is probably due to errors in processing in some samples; see Figure 4-12 for a resonator in which the transmission line has largely been etched away at some point in the process. In other samples, some part of the connection between the SMA cables and the Nb_3Sn sample was broken, resulting in no transmitted signal.

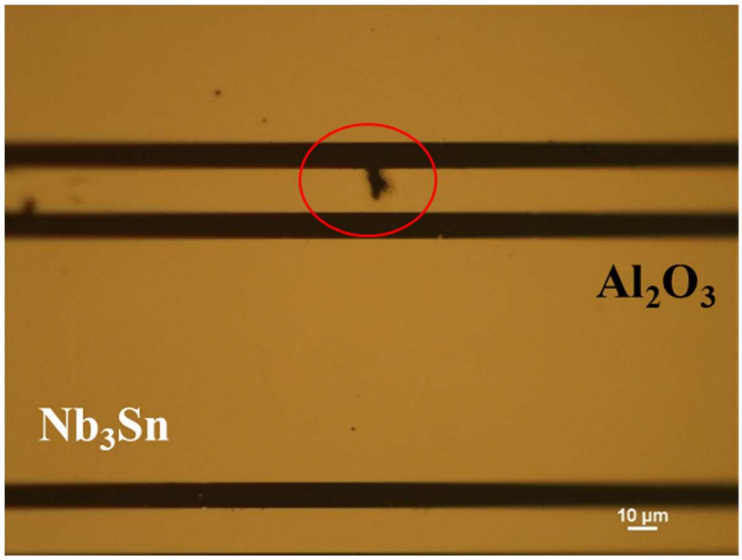

Figure 4-12: resonator strip under an optical microscope. Light regions are Nb_3Sn, dark regions are Al_2O_3 substrate. A large piece of the center strip has been etched away during the process.

The samples for which S_{21} data is available were grown at r_{Sn} = 0.8, 1.5, and 2.5 Å/s, offering information on some range of growth flux. The resonant peaks are shown and fitted in Figure 4-13.

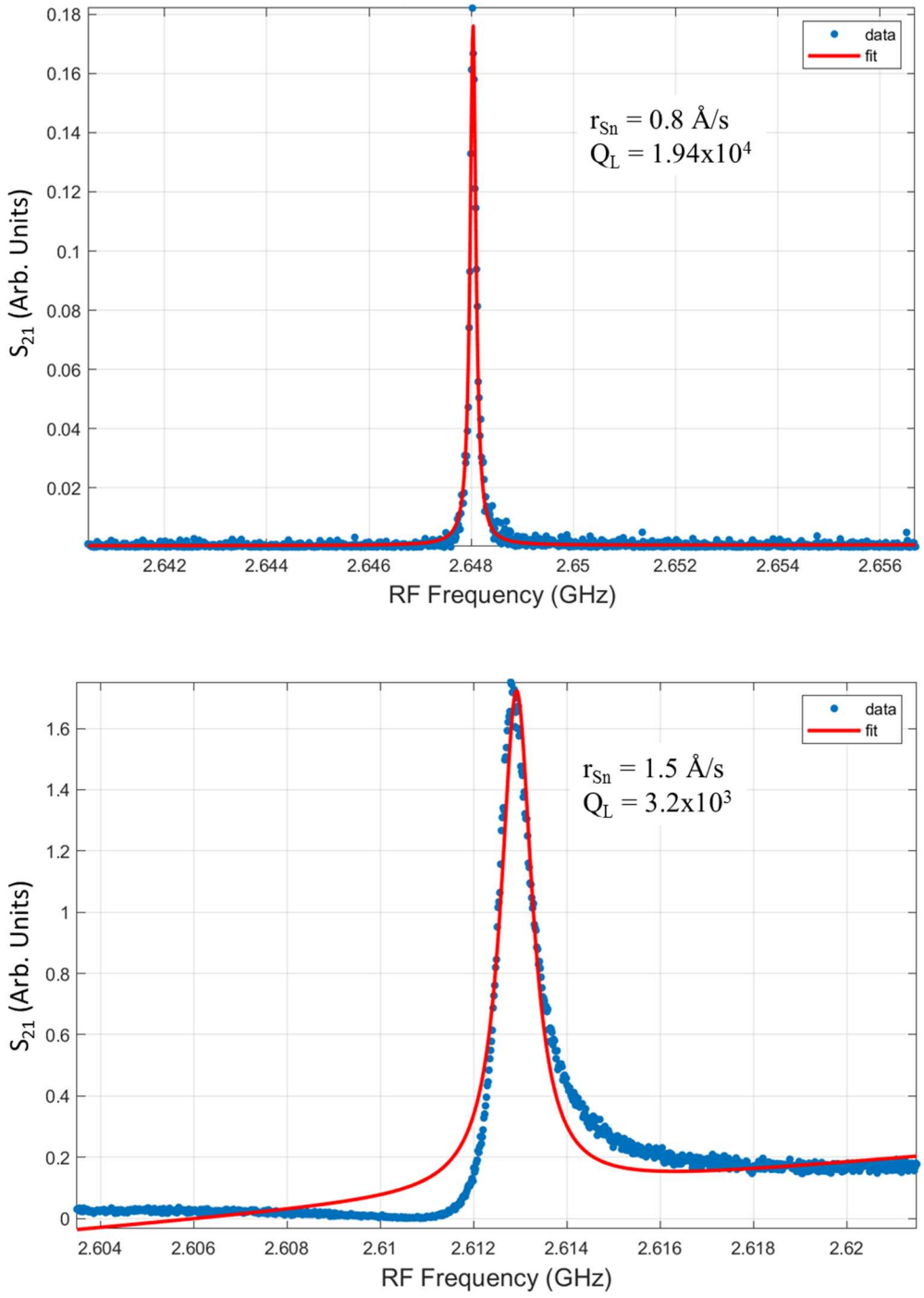

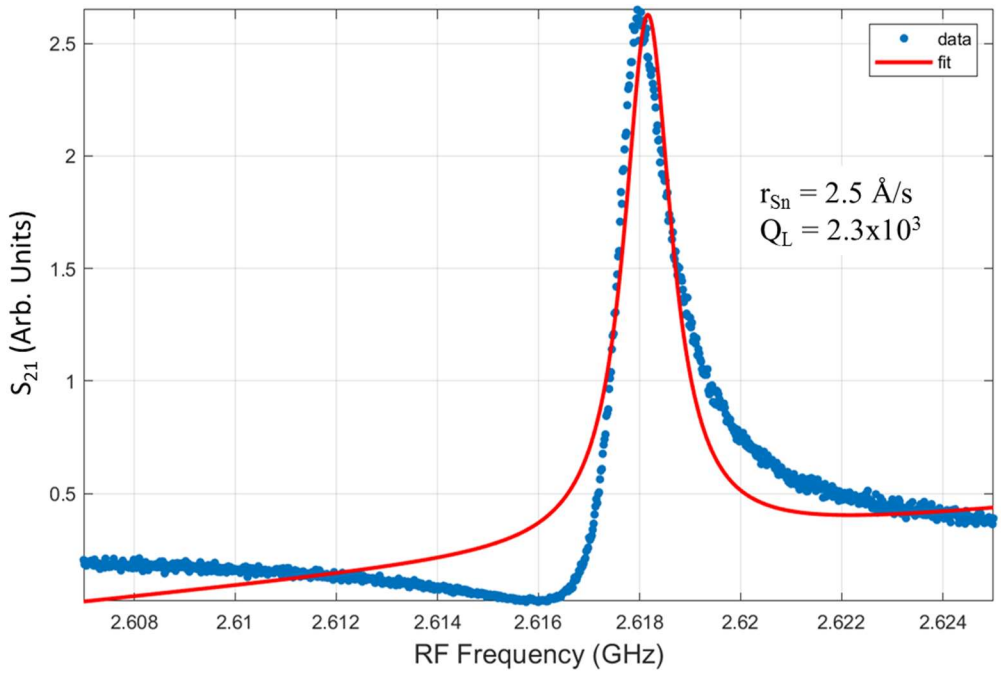

Figure 4-13: S21 plotted against RF frequency for three samples, with r_{Sn} = 0.8, 1.5, and 2.5.

Surprisingly, the film with r_{Sn} = 0.8 Å/s has the highest Q_L, at 1.94x10^4. It is also the film with the most symmetric resonance peak. Samples with r_{Sn} = 1.5 and 2.5 Å/s have strongly asymmetric peaks, with a large dip in S_{21} at lower frequencies. The asymmetric peaks appear to have Fano resonance shapes, characteristic of a dissipative parallel path in the RF circuit [49]. The exact nature of the parallel path is difficult to determine.

If this is an intrinsic effect, it could indicate that the sample grown at r_{Sn} = 0.8 Å/s has the optimal composition for minimizing surface resistance, or that the surface roughness somehow contributes to a normal conducting channel in the resonator. It is possible that this effect originates in the configuration of the measurement boxes. All three samples were measured in identical aluminum boxes, but variation in wire bond height could affect the strength of the coupling between the RF input/output lines and the lid of the box.

The resonance frequency f_0 of these resonators is also noteworthy. Samples with high r_{Sn} have f_0 around 2.615 GHz, while the sample with r_{Sn} = 0.8 Å/s has f_0 = 2.648 GHz, a shift of ~1.2%. Shift in resonance can come simply from variations in length in the resonator; however, this is unlikely, as the size of the capacitive gap is 3.0 µm ±10% in each of these samples, while the resonator itself is ~16 mm long (Figure 4-14).

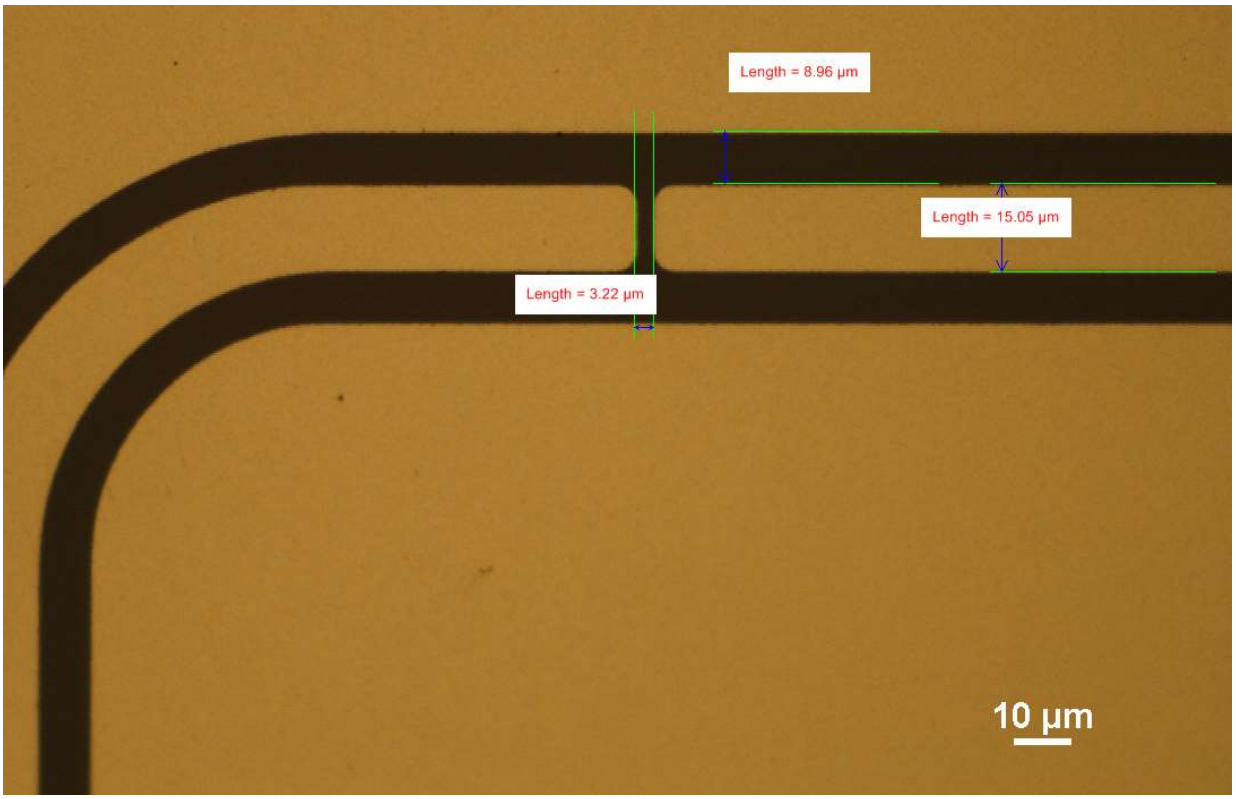

Figure 4-14: Microscope image of the capacitive gap between the RF input and resonator. The gap is always between 2.8 and 3.3 µm, indicating that the length of the resonator is very consistent.

This leaves the possibility that the kinetic inductance is responsible for the difference in f_0. Lower penetration depth λ in r_{Sn} = 0.8 could cause this, which could arise from differences in roughness, or the presence of defects in films with higher r_{Sn}. The asymmetric resonance shape and f_0 shift could provide further insight into the effects of roughness and stoichiometry on the RF properties of these films.

CHAPTER 5

Novel Phase Found by THz Pump-Probe Spectroscopy in Nb_3Sn Thin Films

For further characterization of single-layer Nb_3Sn thin films, a single film was sent for THz time-domain spectroscopy (THz-TDS) pump-probe measurements at Iowa State University, in Dr. Jigang Wang's lab. THz-TDS consists of analyzing amplitude and phase shifts in a wave that is transmitted through a medium to extract electronic and optical properties of the medium. This chapter describes the equilibrium state THz-TDS of Nb_3Sn, as well as an unexpected phase discovered under resonant excitation of the superconducting phase.

5.1 Equilibrium State

For this technique, films were grown 20 nm thick on 1 mm R-plane Al_2O_3 substrates, with both sides polished smooth. Both the thickness of the film and the polishing maximize transmission through the sample, and the substrate was 1 mm thick to sufficiently separate the signal from any reflections that would travel to the detector from the backside of the sample. To characterize the ground state of the samples, THz spectroscopy was performed at cryogenic temperatures without a pump pulse. The complex conductivity $\sigma_1+i\sigma_2$ is plotted against frequency in Figure 5-1.

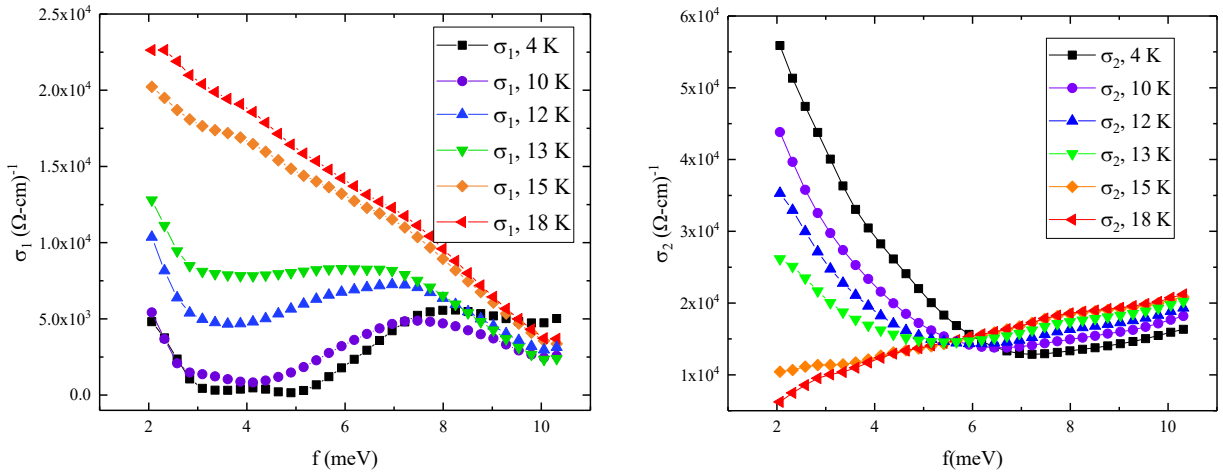

Figure 5-1: Real and imaginary parts of the temperature-dependent optical conductivity of 20 nm thick Nb3Sn. Real part shows the gap open at low temperatures, and is accompanied by a 1/ω response in the imaginary part.

At low temperatures, a gap opens in the σ_1 spectrum, corresponding to the depletion of charge carriers at these energies as they condense to form Cooper pairs at lower energies. A peak can be seen at low frequencies, corresponding to the Cooper pairs with infinite conductivity. The gap size is $2\Delta \approx 5.1$ meV, which aligns well with the BCS prediction of $2\Delta/k_BT_c = 1.75$. Above the gap, quasiparticles present at equilibrium conditions conduct current, and σ_1 takes on a nonzero value. As the temperature rises from 4 K to 18 K, the gap appears to fill in due to a large population of quasiparticles above the gap that can absorb photons at subgap frequencies. Above T_c, the conductivity takes on a shape comfortably described by the Drude model for a normal metal, with a peak at $\omega = 0$. The corresponding inductive response at low temperature follows the Drude model for a conductor with infinite scattering time $\tau \rightarrow \infty$. The $1/\omega$ response of σ_2 aligns well with expectations of superconducting behavior at low temperatures.

Though other superconducting films have been studied with this method [50], the steep slope of the normal-state σ_1 of the Nb_3Sn film indicates that the scattering time τ is quite high. From

fitting σ_1 to the Drude model $\sigma_1 = \frac{n_n e^2 \tau}{m(1+\omega^2\tau^2)}$, τ = 0.54 ps is extracted. The BCS coherence length is $\xi_0 = \hbar v_F/\pi\Delta$. The mean free path l_{mfp} can be estimated from $v_F\tau = l_{mfp}$, making it possible to correlate l_{mfp} to ξ_0 through $\hbar/\tau \approx 2\Delta$, with $\xi_0 = v_F\tau/\pi = l_{mfp}/\pi$. This puts this sample in the crossover between the clean and dirty limits and very close to the regime of $l_{mfp} = 0.5\ \xi_0$, where we expect to see a minimum in R_s [42]. Though not extraordinary in itself, this makes it possible to see some features of the superconductor under excitation that would otherwise be obscured by scattering.

5.2 Pump-probe measurements

Observing a meaningful signal transmitted through an optically pumped superconductor has historically been difficult [51,52]. At pump energies larger than the gap size 2Δ, Cooper pairs are broken, and the probe pulse can measure the behavior of the quasiparticles as they recondense into pairs. Any excess energy provided to the film is absorbed by the quasiparticles, and they must relax to the edge of the gap before they can recombine. They shed the energy in the form of phonons as they collide with the lattice. These phonons in turn break more Cooper pairs, complicating the return to the superconducting ground state.

The process is described by the Rothwarf-Taylor model, which describes the temporal evolution of the density of excess quasiparticles and phonons injected into a superconductor [53,54]. The coupled Rothwarf-Taylor equations are written as

$$\frac{dn}{dt} = \beta N - Rn^2 - 2Rnn_T \qquad \text{[Eqn. 8]}$$

$$\frac{dN}{dt} = \frac{1}{2}[Rn^2 - \beta N] - \frac{(N - N_0)}{\tau_P}$$

Here, n is the excess quasiparticle density, n_T is the thermal quasiparticle density, N is the excess density of phonons with energies greater than 2Δ, R is the bare quasiparticle recombination rate, β is the rate of pair breaking by phonons with energy $>2\Delta$, and τ_P describes the relaxation time of the phonons either by anharmonic decay to energies $<2\Delta$ or through phonon escape from the sample. Of this set of processes (pair breaking, quasiparticle relaxation, pair re-formation, phonon diffusion), the phonon lifetime is the longest, resulting in what is known as the *phonon bottleneck* when measuring nonequilibrium superconductors. The quantity R is difficult to determine, and phonon decay τ_P is the dominant factor in the measurement. This can be circumvented by providing a pump pulse with a tuned photon energy $\hbar\omega \approx 2\Delta$, minimizing excess energy absorbed as phonons (N). This makes it possible to see features of the quasiparticle conductivity without being hindered by the phonon bottleneck, and reveals some interesting features of the Nb_3Sn films.

After thoroughly characterizing the ground state, the excited state was produced and examined. A single-cycle pump pulse with a frequency centered at 4 meV and a field strength of up to 620 kV/cm was passed through the film, followed by a probe pulse after a time interval Δt_{pp}. The frequency spectra σ_1 and σ_2 of the excited state for various pump field strengths are shown in Figure 5-2. As is expected, the gap in σ_1 closes as Cooper pairs are broken and repopulate the film with normal conducting states; this coincides with a downturn in σ_2 near the Fermi level, moving away from a $1/\omega$ behavior and resembling the normal state. However, a sharp peak in σ_1 persists in the excited state. Even at high pump fluences of 620 kV/cm, when the σ_2 shows that the inductive response of the sample is identical to that of a normal metal, σ_1 of the excited state has a peak at low frequencies that deviates from the normal state. The integrated spectral weight of the excited sample is ~10% higher than that of the ground state of the normal metal.

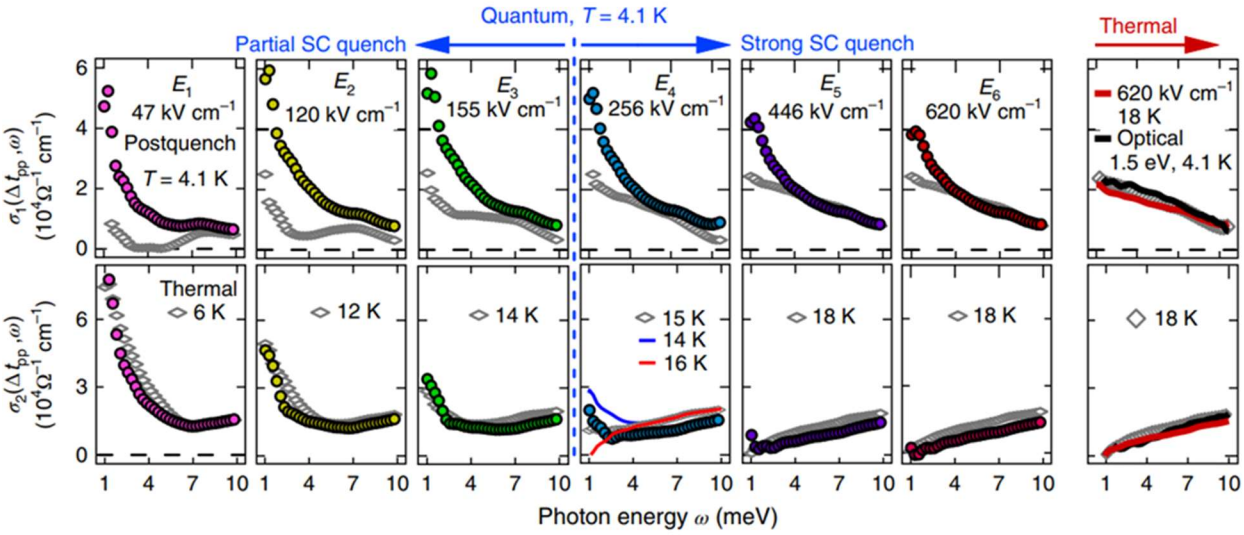

Figure 5-2: Optical conductivity of Nb3Sn after a single-cycle THz pump at increasing fields. A quench using optical frequencies is compared on the right. Reproduced from [55].

Figure 5-3 shows the relaxation from the excited state back to the ground state by plotting the change in the electrical field of the probe pulse, $\Delta E/E_0$, against time, Δt_{pp}. At low quench fields, the decay from the excited state to the ground state is characterized by a smooth recovery with a relaxation time $\tau_{fast} \sim 0.6$ ns. However, at high quench fields > 256 kV/cm where the condensate is depleted, this behavior changes to a much longer-lived state characterized by a relaxation time $\tau_{slow} \sim 7$ ns.

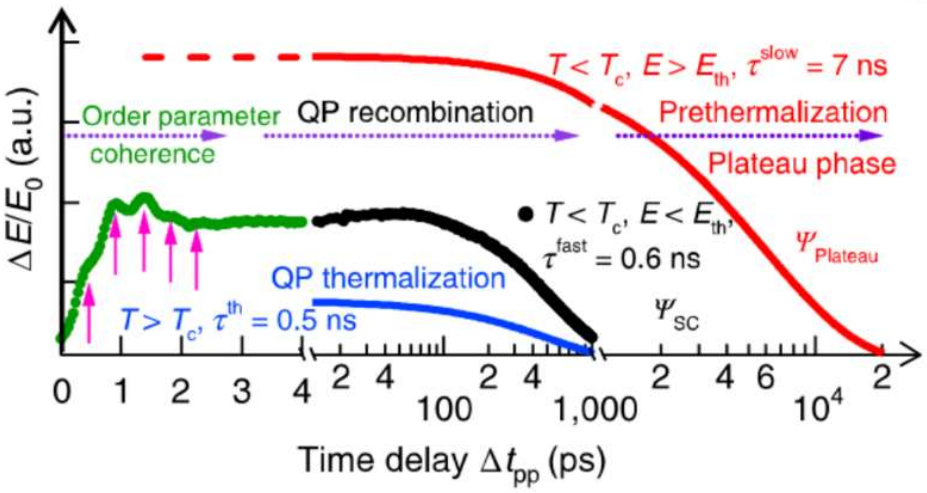

Figure 5-3: Relaxation timescales for low-field quench (green, black, blue) and high-field full quench (red). These two regimes are distinguished by relaxation times that differ by an order of magnitude. Reproduced from [55].

To show that these features arise uniquely from a pump pulse resonant with the gap, the quench was also performed with an optical pulse with energy 1.5 eV, much larger than the superconducting gap at 5.5 meV. The resulting conductivity appears identical to that of the normal state even at 4 K, lacking the sharp peak in σ_1 close to E_F. These distinct features could arise from order-parameter fluctuations in a gapless quasiparticle quantum phase that emerges after non-thermal superconducting condensate depletion. This is distinct from what has been observed in resonant pumped superconductors in the past, where an inhomogeneous mixed SC/normal state was found [50], or in cases where the superconductor is in the dirty limit, where the normal and pumped states would be indistinguishable from one another.

5.3 Origins of enhanced conductivity

To explain how the gapless QP phase arises, the group at ISU turned to a mean-field model introduced by Bilbro and McMillan [56], which theorized that the coexistence of a larger CDW gap Δ_W along with the superconducting gap Δ_{SC} affected the superconducting properties of the metal.

This CDW phase is driven by strong electron-phonon coupling that leads to a martensitic Peierls transition to a tetragonal unit cell for Sn compositions around 25% and T ~ 40 K.

With the THz quenches, the equilibrium CDW gap size $\Delta_{w,0}$ is reduced, transferring some of its spectral weight to lower frequencies and leading to a peak in σ_1. This is demonstrated in Figure 5-4, where Δ_w is set to a laser-decreased value of 0.8 and $0.9\Delta_{w,0}$, and σ_1 shows a sharp peak near zero frequency compared to the equilibrium value.

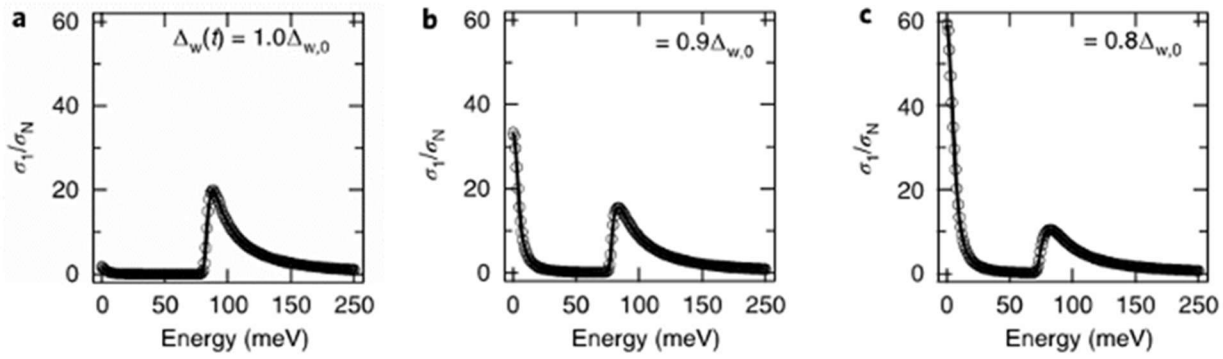

Figure 5-4: Model of the conductivity σ_1 using theory developed in [56]. As the CDW gap size Δ_w is changed, conductivity near the Fermi energy rises sharply.

To further confirm this, 3 cases of Δ_w and Δ_{SC} are compared (Figure 5-5): (1) No pump has been applied, and $\Delta_{SC} = \Delta_{SC,4K}$; in this case, the free energy minimum lies at $\Delta_w = \Delta_{w,0}$, which corresponds to equilibrium in the superconducting state. (2) The system is above T_c = 18 K, and $\Delta_{SC,18K} = 0$. The equilibrium value of $\Delta_{w,0}$ now lies at a slightly higher value, since it does not compete with the superconducting gap. This also corresponds to quenching of the superconducting state via optical pump. (3) In the pumped state, $T < T_c$ while $\Delta_{SC,4K} = 0$. The free-energy landscape is qualitatively different, with a local minimum developing at $\Delta_w \sim 0$. The system can become trapped in this local minimum with sufficient pump fluence, resulting in a long-lasting state with a slow decay time to the equilibrium state.

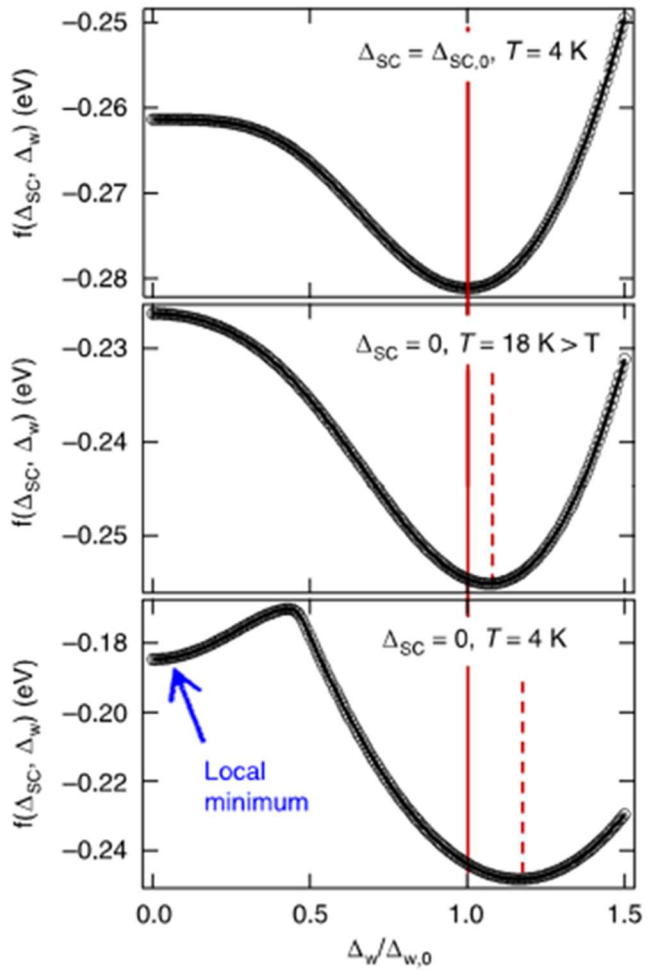

Figure 5-5: Free energy of nonequilibrium states of Nb_3Sn for various values of Δ_{SC} and Δ_w.Reproduced from [55].

This discovery has implications for further discoveries in nonequilibrium superconductivity, where competing orders may be extended to access hidden density-wave phases and quantum criticality under the SC dome in high-T_c materials.

CHAPTER 6

Growth and Properties of SIS Multilayer Structures

This section describes the steps taken to scale from the successful control over Nb_3Sn film growth to SIS multilayer growth on 2" diameter wafers, and the resulting RF properties of these wafer-scale films in cavity geometries.

6.1 Nb_3Sn layer

The purpose of the S (Nb_3Sn) layers is to screen out magnetic field from the interior of the cavity, while also resisting vortex formation. These films were made with thickness $d < \lambda$ to decrease the thermodynamic stability of vortices parallel to the surface. With $\lambda \sim 85$ nm in stoichiometric clean bulk Nb_3Sn, λ in these films is expected to be 100~120 nm at 4 K. The S layer was grown with a target thickness of $d = 60$ nm for some samples, and $d = 120$ nm for others.

In initial growths, these multilayers were grown with Sn flux of 0.8 Å/s, as these provide the smoothest surfaces and lend themselves to convenient layering. However, on growing an S-I structure (Nb_3Sn/Al_2O_3) and holding it at $T_{Mo} = 870$ °C in vacuum to emulate growth conditions for another Nb_3Sn layer, it was found that the T_c of the S layer decreased drastically after this process to 9.2 K, with a superconducting transition that begins at around 16 K, as shown in Figure 6-1. This is consistent with segregation of the film into Nb_3Sn and Nb. This makes it clear that Sn-deficient Nb_3Sn, while providing an avenue into discovering properties of nonstoichiometric Nb_3Sn, is not well-suited for the purpose of growing SIS multilayers at sustained high temperatures. All S layers in multilayers were grown with Sn flux of 1.5 Å/s, which resulted in optimal T_c and RRR for films in Chapter 4.

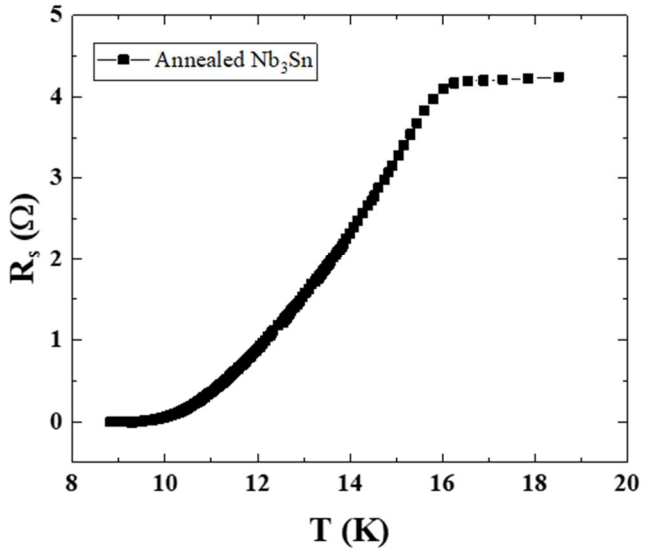

Figure 6-1: Superconducting transition for film grown at r_{Sn} = 0.8, then annealed with Al_2O_3 cap for 50 minutes. Transition begins at 16 K, which is typical for Nb_3Sn, but the sample becomes fully superconducting only at 9.2 K, which is the T_c of Nb.

A Nb_3Sn single-layer film growth with Sn flux 1.5 Å/s was taken through the same process as the film grown with r_{Sn} = 0.8 Å/s. A 3 nm Al_2O_3 layer was grown on top at room temperature, then the sample was held at T_{Mo} = 870 °C to emulate growth conditions for the top Nb_3Sn layer. Where the r_{Sn} = 0.8 film segregated into two phases, this film remained in the Nb_3Sn phase. In addition, the superconducting properties improved noticeably compared to un-annealed films (Figure 6-2). T_c increased from 17 to 17.25 K without affecting the transition width, and most notably the RRR increased from 3.5 to 4.26. This improvement through thermal treatment suggests that the as-grown Nb_3Sn films are not fully reacted or retain structural distortions that are removed though annealing.

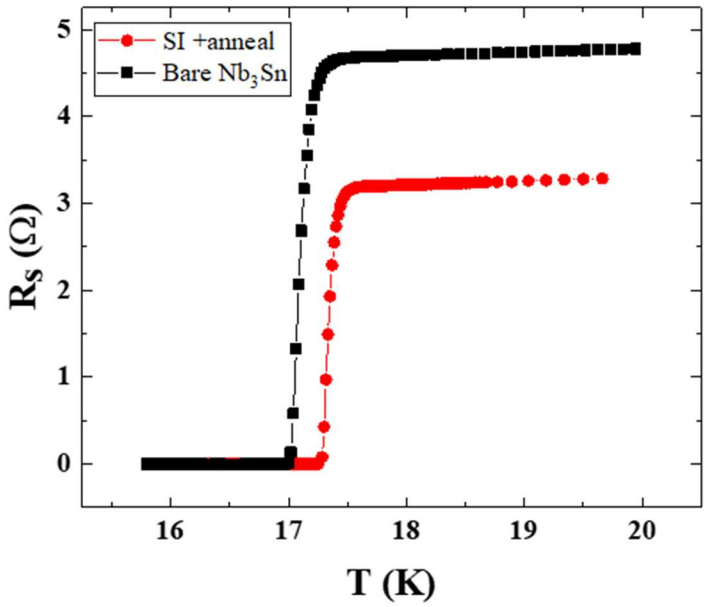

Figure 6-2: Superconducting transition for a film grown at r_{Sn} = 1.5, capped with Al_2O_3, and annealed at T_{Mo} = 870 for 10 minutes to simulate the conditions for another Nb_3Sn layer growth. T_c and RRR are both improved in comparison to films that do not receive the annealing treatment.

6.2 Al_2O_3 layer

The purpose of the insulating layer is to isolate the superconducting layers from each other to the extent that vortex currents are not stable in the S layers. Al_2O_3 was selected for the insulating layer, since it is already present in the system as the substrate, and we are familiar with its epitaxial relationship to Nb_3Sn. Ideally, it has the same RF properties as a thin film that lead to its selection as a substrate – high dielectric constant, and low loss tangent. Al_2O_3 is easily sputtered from a single-phase ceramic target using RF power. However, because the heater element is radiative, we cannot flow O_2 through the growth chamber while heating the sample, as this can rapidly degrade the heater element. Because of this, Al_2O_3 layers were grown using only Ar as a working gas.

To minimize any losses caused by RF dissipation in the Al_2O_3, these layers are grown as thin as possible. With 100 W supplied to the target in 3 mtorr Ar at 15.5 cm from the sample, the growth rate was measured as 0.3 Å/s using a QCM. 3 nm of Al_2O_3 was deposited onto a 60 nm

Nb_3Sn film (1.5 Å/s Sn) at room temperature without breaking vacuum using these growth conditions. AFM images of this sample are compared with a bare Nb_3Sn sample grown under the same conditions in Figure 6-3. There is no clear indication of the presence of Al_2O_3 in the SI sample; XRD is also inconclusive, showing only the Nb_3Sn and substrate peaks.

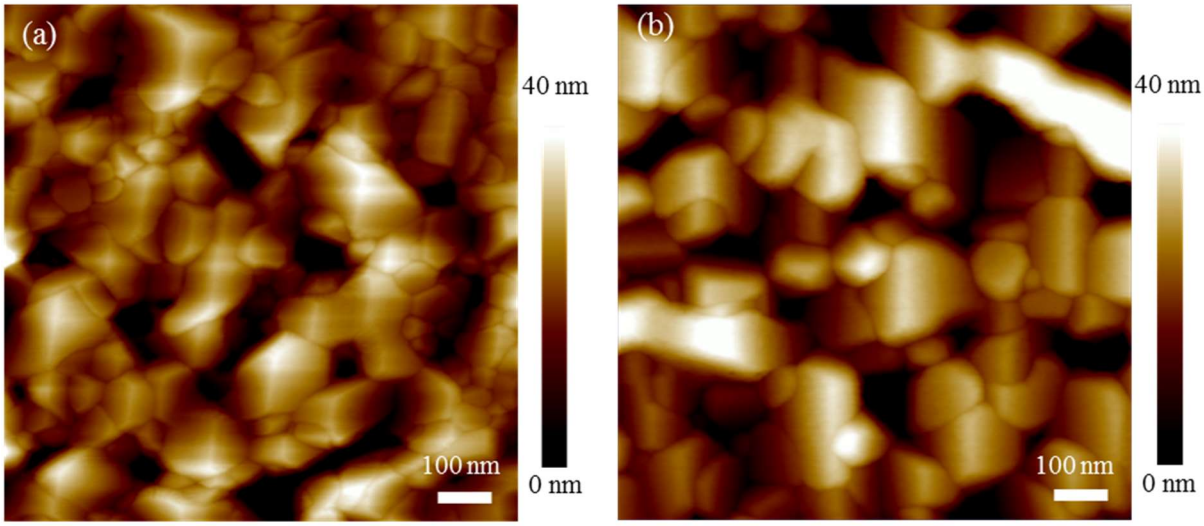

Figure 6-3: AFM images for (a) bare Nb_3Sn, and (b) Nb_3Sn coated with 3 nm Al_2O_3. There is no sign of islanding or segregation of Al_2O_3.

To confirm that Al_2O_3 is in fact arriving at the Nb_3Sn film surface, a bare Si (001) substrate was coated in Al_2O_3 under the same conditions, with a target thickness of 6 nm. XRR (Figure 6-4) of the Al_2O_3/Si and bare Si from the same wafer show that the Al_2O_3 is clearly present, and has the target thickness of 6 nm. The raw data is fit best with a film density of 4.22 g/cm^3, a density 6% higher than the 3.98 g/cm3 of α-Al_2O_3. This could simply be an instrumental or fitting error, but there is a possibility that the deposited Al_2O_3 film is deficient in O, leading to an overall higher density. This could result from the relatively lighter O atoms deflecting more during their travel from the target to the sample. An O deficiency in the Al_2O_3 film could manifest strongly as high losses under RF excitation.

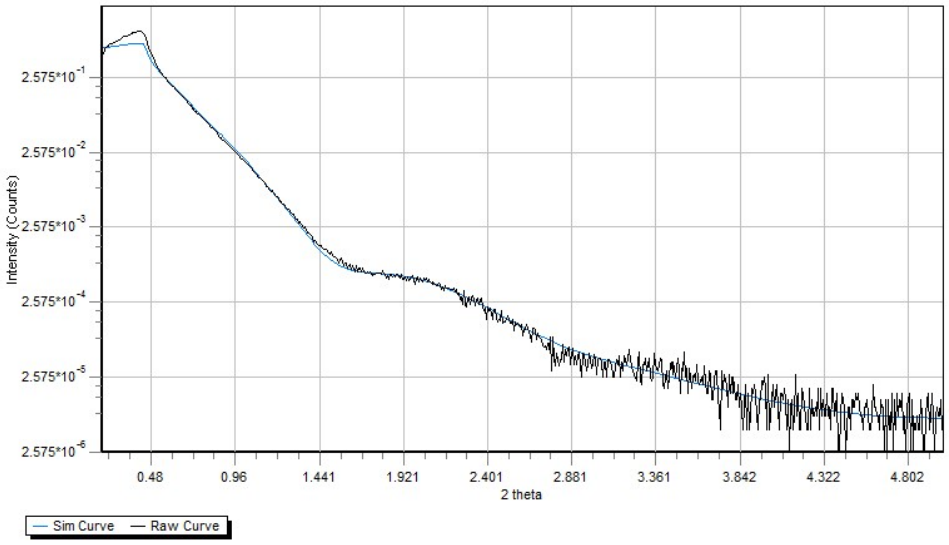

Figure 6-4: XRR of 6 nm of Al_2O_3 on Si, fitted using Bruker LEPTOS software.

AFM images of the Al_2O_3/Si (Figure 6-5) show that the Al_2O_3 layer is quite smooth, with roughness of 0.5 nm.

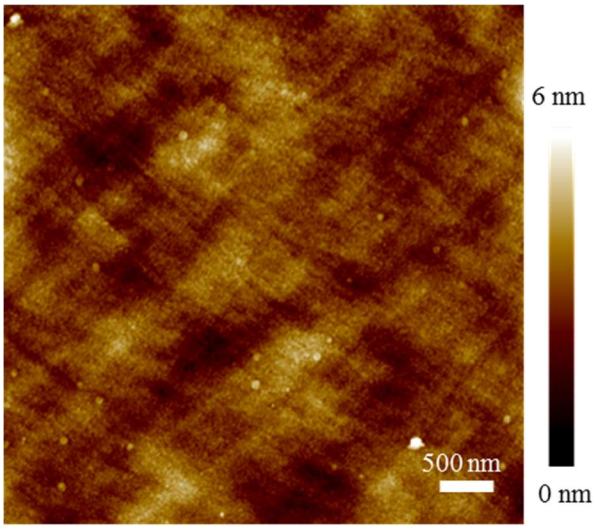

Figure 6-5: AFM of Al_2O_3/Si, showing a smooth surface with RMS roughness 0.5 nm.

6.3 3-Layer SIS Multilayer Sample

With confirmation that Al_2O_3 was depositing at the intended rate, a SIS structure was fabricated. A 60 nm Nb_3Sn layer was deposited first with T_{Mo} = 870 °C and r_{Sn} = 1.5 Å/s. This

layer was allowed to cool below T_{Mo} = 100 °C before 3 nm of Al_2O_3 was deposited, with 100 W power supplied in 3 mtorr of Ar. After deposition, the sample was re-heated to T_{Mo} = 870 °C over the course of 30 minutes, and another Nb_3Sn layer was deposited at the same conditions as the first. T_p remained constant during growth of this layer, and matched the T_p at the end of the first Nb_3Sn layer growth, confirming that both were grown at the same temperature.

AFM of the sample (Figure 6-6) shows that much of the (023) orientation of the first layer transfers into the top layer. However, other orientations are present at a larger proportion than in bare Nb_3Sn. XRD data confirms this – Figure 6-7 shows that the (012) peaks are still present and distinct, but polycrystalline rings are superimposed over these peaks. This suggests that the epitaxial relationship between the Al_2O_3 film layer and the first Nb_3Sn layer is complex, and the crystal directions are not maintained between the two Nb_3Sn layers.

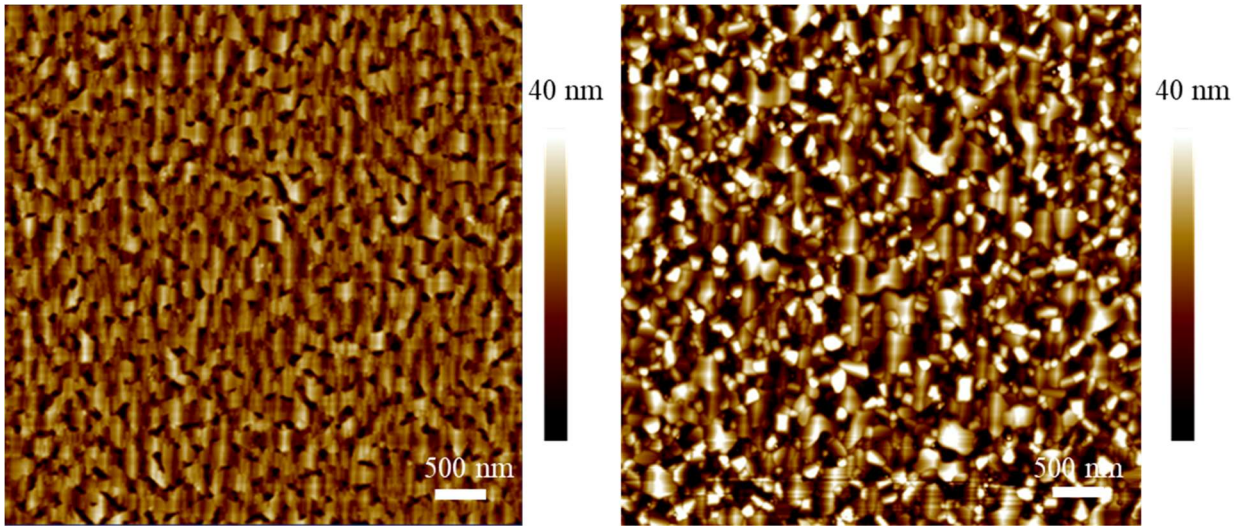

Figure 6-6: AFM images of bare Nb3Sn (left) and the SIS multilayer (right). (023) orientation is clearly preserved on the right, but a large number of polycrystalline grains are also present.

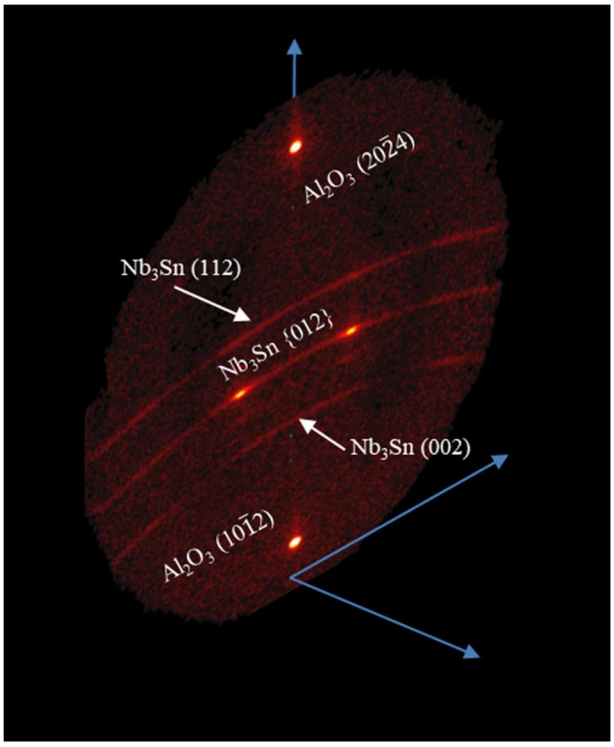

Figure 6-7: 2D-XRD of SIS sample. (012) peaks from first layer are present, as well as polycrystalline rings.

DC measurements of the sample are difficult to interpret. If the two Nb_3Sn layers are completely isolated from one another, we expect a sheet resistance R_s of ~15 Ω at room temperature, which corresponds to only measuring the top layer. However, when the SIS multilayer is measured, R_s is 7 Ω at room temperature. This suggests that the top and bottom layers are strongly connected to one another, and corresponds to a 120 nm thick Nb_3Sn film with roughly the same resistivity as the thinner films.

There are several possibilities that account for this. One possibility is that the probes that form the contact between the measurement system and the sample apply enough pressure to simply pierce through all 3 layers, and measures the sheet resistance of the overall sample (Scenario 1 in Figure 6-8). A second possibility is that the 3 nm film does not completely cover the Nb_3Sn film. Since the roughness of these Nb_3Sn films is ~10 nm, and the Al_2O_3 layer thickness is only 3 nm, some regions of the Nb_3Sn film may not be fully covered, and the bare regions connect to the

second Nb_3Sn layer (Scenario 2). Another possibility is that the Al_2O_3 layer diffuses into the Nb_3Sn layers upon heating (Scenario 3), and the two layers are electrically connected after growth.

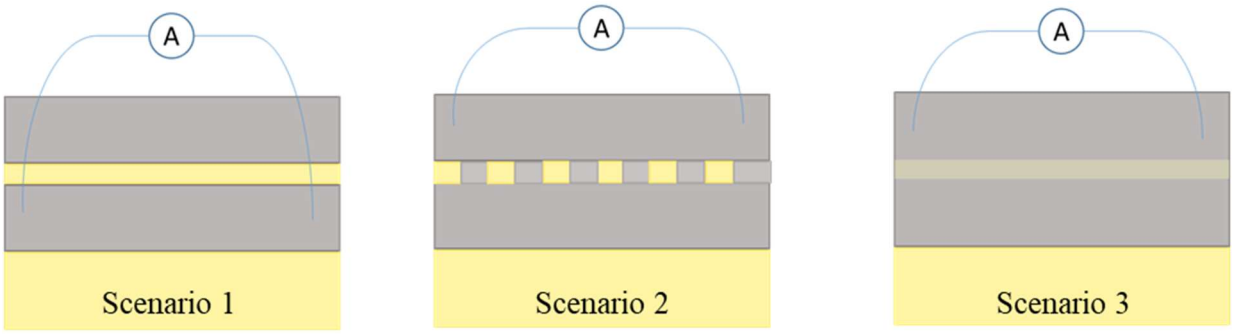

Figure 6-8: Three possibilities for low sheet resistance in SIS multilayer. 1: probes simply punch through all layers. 2: dielectric layer is not complete, allowing two S layers to connect. 3: dielectric layer has dissolved, and does not separate the two S layers.

It is difficult to distinguish between these scenarios with the tools available in our lab (AFM, XRD, DC transport). In order to get direct insight on the structure of the multilayer, a 5-layer (SISIS) multilayer was grown and characterized using cross-sectional TEM.

6.4 5-layer SISIS multilayer

A 5-layer sample was grown to quantify the effect of cooling and re-heating on the Nb_3Sn and Al_2O_3 layers. 60 nm Nb_3Sn layers were grown at T_{Mo} = 870 °C, and 6 nm Al_2O_3 layers were grown at T_{Mo} < 150 °C. Al_2O_3 layer thickness was doubled in an attempt to reduce contact between Nb_3Sn layers. As with the SIS sample, the 2nd and 3rd Nb_3Sn layers reached T_p = 905 °C at the beginning of growth. However, both exhibited an increase in T_p to 925 °C when Nb and Sn flux were switched on, while T_{Mo} remained constant. T_p subsequently decreased to 900 °C over the course of layer growth., as shown in Figure 6-9. Since T_{Mo} is controlled and remains constant, this suggests a shift in emissivity rather than a change in growth temperature. One possibility is that Al_2O_3 reacted with the impinging Nb and Sn atoms, forming a layer with slightly higher emissivity

at the beginning of growth. If there is a third material present in the structure, its properties could contribute strongly to RF resistance.

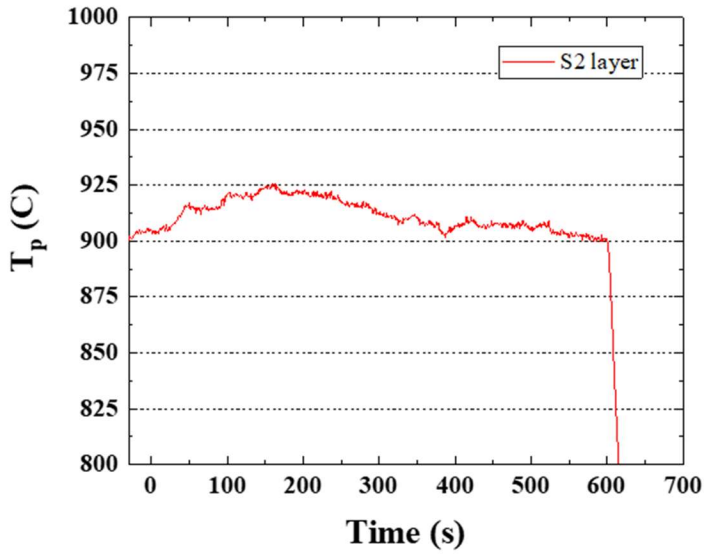

Figure 6-9: Shift in T_p during growth of Nb_3Sn on top of a sputtered Al_2O_3 layer. Tp climbs from 900 to 925 °C when Nb and Sn flux is switched on, then drops back to the starting T_p of 900.

AFM images show what appears to be pure Nb_3Sn as the surface layer, with some of the (023) texture preserved, though the layer appears largely polycrystalline (Figure 6-10). XRD confirms this, with strong (012) peaks overlaid with polycrystalline rings, as was the case with the SIS sample.

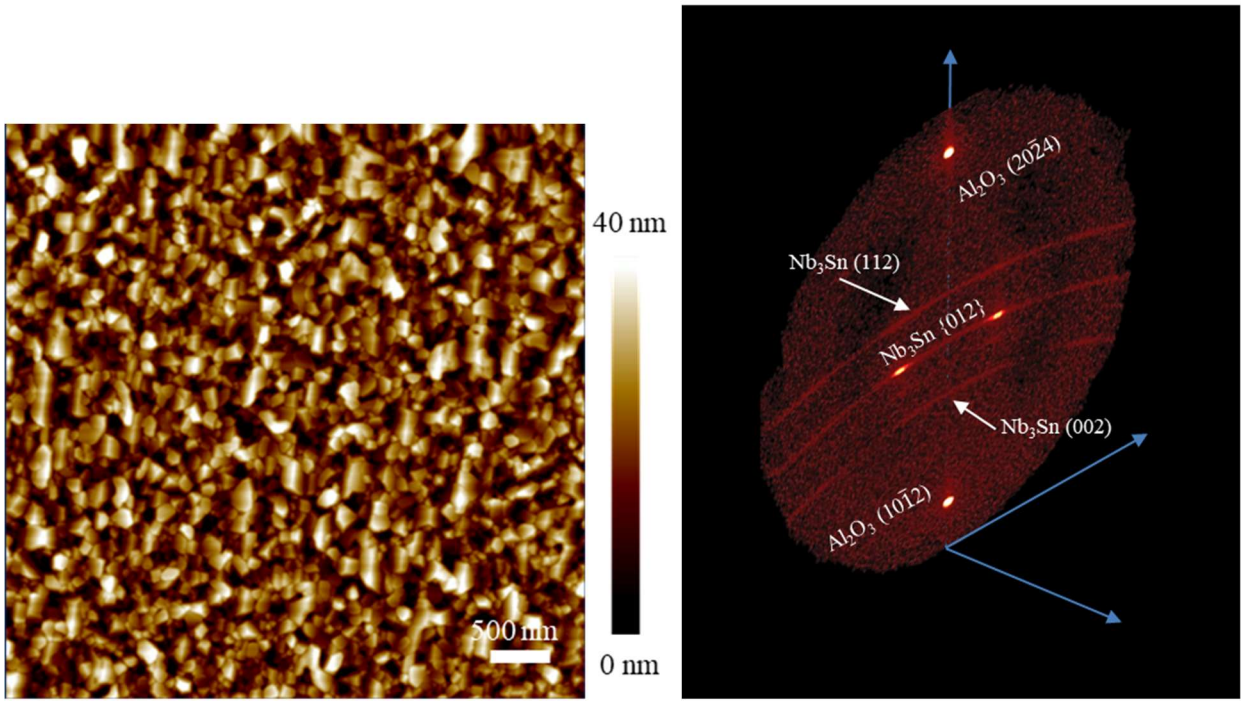

Figure 6-10: AFM image of SISIS sample, where some (023) texture is still discernible, and 2DXRD image confirming that a large proportion of the film is polycrystalline, while the first S layer remains in the usual orientation.

Cryogenic DC measurements show that the quality of the superconducting layers is consistent with single-layer Nb_3Sn films. T_c is 17.14 K, and RRR is 3.3, which compares well with a single-layer film grown at r_{Sn} = 1.5 Å/s. T_c is higher than the bare Nb_3Sn sample (17.05 K), but lower than the Nb_3Sn+Al_2O_3+anneal sample (17.27 K, RRR = 4.26). This suggests that simply annealing the Nb_3Sn layer improves the superconducting properties of the Nb_3Sn layer. The annealed sample has the highest T_c and RRR, which corresponds to the 1st and 2nd Nb_3Sn layers of the SISIS sample. The top Nb_3Sn layer is not annealed, leading to the slightly depressed superconducting properties. When the three layers are in contact, some convolution of the three is measured in DC measurements. Sheet resistance is ~4.7 Ω at room temperature, consistent with a single layer of thickness ~180 nm; this again suggests that the three superconducting layers are

strongly interconnected. Doubling the Al_2O_3 layer thickness from 3 nm to 6 nm seems to have had little effect on the connection between superconducting layers.

Cross-sectional TEM measurements were conducted to gain more insight into the structure of the multilayer. Figure 6-11a shows a magnified image at the interface of the Al_2O_3 substrate and Nb_3Sn film. Two grains are present, one of which is the (023) orientation (left). On the right, a different orientation is present. This grain corresponds to a BCC structure viewed along the (110) zone axis, with the [001] direction pointing up.

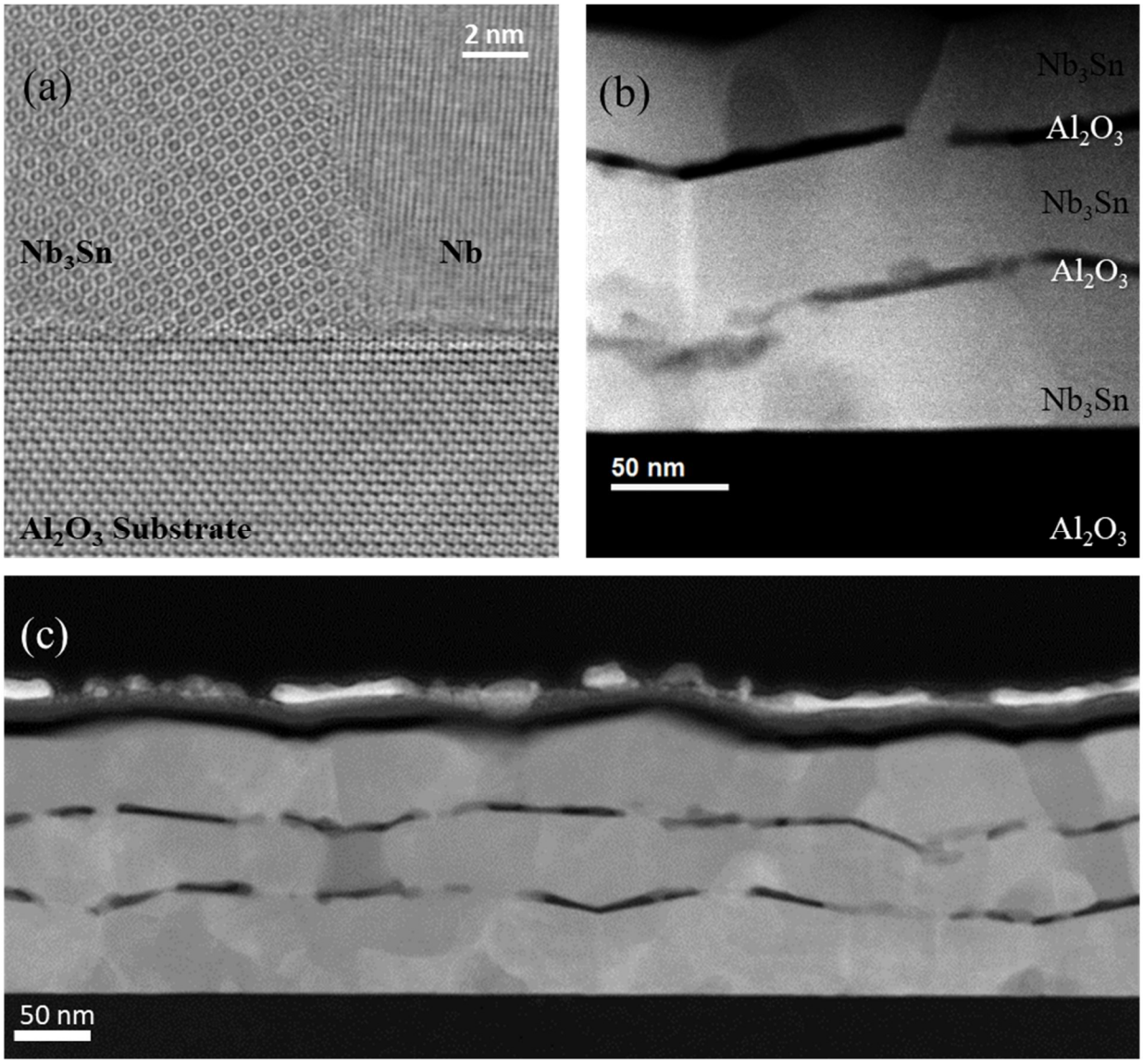

Figure 6-11: (a) High-magnification iDPC image of the interface, showing (023) Nb_3Sn orientation. (b) Image of the grain structure across the multilayer thickness. Al_2O_3 is present, but discontinuous, and cloudy in some areas. (c) low-magnification image shows that Al_2O_3 morphology is similar in both I1 and I2, but most gaps are smaller than λ_{Nb3Sn}

Composition mapping by EDS (Figure 6-12) indicates that there are regions with significant Sn deficiency in the Nb_3Sn layers. Nb is a BCC material, and the only stable phase in the Nb-rich portion of the Nb-Sn system is pure Nb. These results strongly suggest that elemental Nb grains exist in these films inside of the Nb_3Sn matrix. In high-field environments, these grains

could be weak points where magnetic field penetrates and causes quench at lower fields than expected.

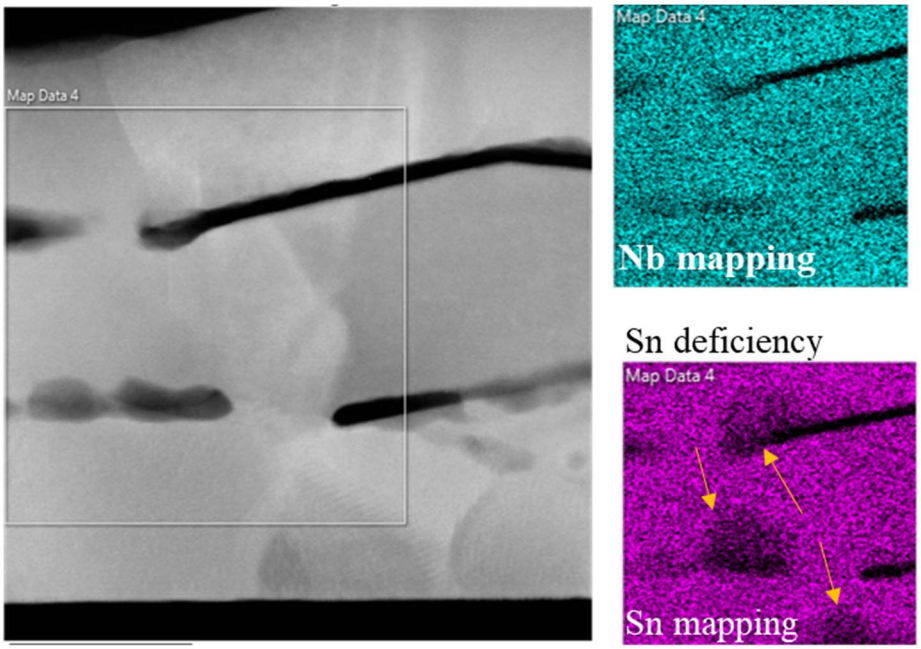

Figure 6-12: Cross-sectional TEM EDS compositional mapping of Nb and Sn. There are Sn-deficient regions that do not correspond to Al_2O_3 layers, providing further evidence that pure Nb grains are present in the films.

Upon zooming out (Figure 6-11b), it is clear that the Al_2O_3 layers are present and separate the Nb_3Sn layers, although not completely. A break in the upper Al_2O_3 layer (I2) connecting the two Nb_3Sn (S2 and S3) layers is clearly discernible. The crystal direction of S3 is set by the exposed S2 orientation in the vicinity of the gap. The lower Al_2O_3 layer (I1) appears murkier compared I2. However, on zooming out further (Figure 6-11c), discontinuities and "murky" regions appear at comparable rates in both the I1 and I2 layers. These are likely regions where the 70-90 nm thick TEM cross-section samples both Al_2O_3 and Nb_3Sn.

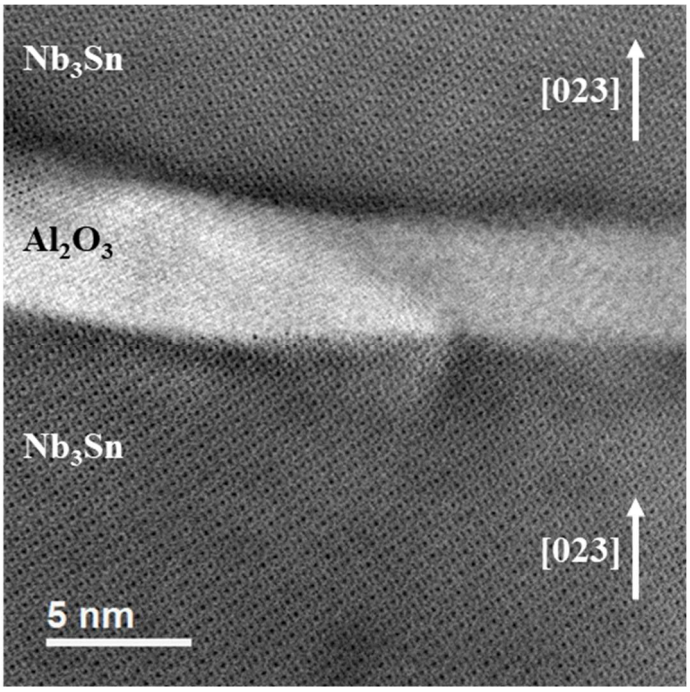

Figure 6-13: Image of Al_2O_3 layer, sandwiched by Nb_3Sn. Crystallographic direcion of Nb_3Sn is consistent on both sides of the I layer.

Figure 6-13 shows a magnified image of the SIS interface, where the (023) orientation of Nb_3Sn is clearly preserved across the Al_2O_3 layer. Though Al_2O_3 is deposited at room temperature, the process of bringing it to T_{Mo} = 870 °C imparts enough heat for it to crystallize with an epitaxial relationship to the S1 layer, presumably Al_2O_3 (10-12)//Nb_3Sn (023), and the S2 layer grows on top of it with the same relationship.

These images confirm that Scenario 2 from Figure 6-8 is the most likely case, explaining the low sheet resistance in the multilayers. A thicker (> 10 nm) Al_2O_3 insulating layer thickness may help to address the issue, possibly at the cost of increasing RF losses. The gaps that are observed in the Al_2O_3 layer are still smaller than the penetration depth λ of dirty Nb_3Sn (~110 nm), making it possible that these Al_2O_3 layers may serve the purpose of making the Nb_3Sn layers thermodynamically unfavorable for vortex penetration. In order to evaluate the properties of the

multilayer in high-power RF fields, a similar sample was grown on a 2” wafer. This challenge is described in the next section.

6.5 Wafer-Scale Films

The best measurements that can be made of Q_0 and R_s of these films must be in cavity geometry, where magnetic field is applied parallel to the film surface, with no perpendicular components. One way to do this is simply to grow the film or multilayer directly onto a Nb cavity, and measure the dissipation of energy of the cavity under continuous or pulsed operation [32,57,58]. Alternatively, a smaller sample of the film can be integrated into a cavity, and the dissipation can be measured from the heater power required to maintain a fixed temperature, or by measuring the change to the resonance of the cavity [59,60].

This second method does not require as much re-tooling of a deposition system as uniformly coating the inside of an entire cavity, and it is what we used for this stage of the project. 2”-diameter R-plane Al_2O_3 wafers were chosen for these growths. These were loaded into the same deposition system as the 10x10 mm samples were grown in. However, some crucial changes to the heating system should be noted.

6.5.1 Wafer-scale growth

Figure 6-14a shows the heater configuration for 10x10 mm square samples. The substrate sits on a shelf that is cut into a 2”-diameter Mo plate, which sits on a shelf on the wafer holder, and the assembly is held in front of the SiC heater element by Mo clips. A thermocouple is inserted into a groove in the Mo plate, and is clamped in place by Mo screws and another plate. Figure 6-14b shows the heater configuration for growing 2” wafers. The wafer is placed directly on the wafer holder, changing the thermal environment considerably.

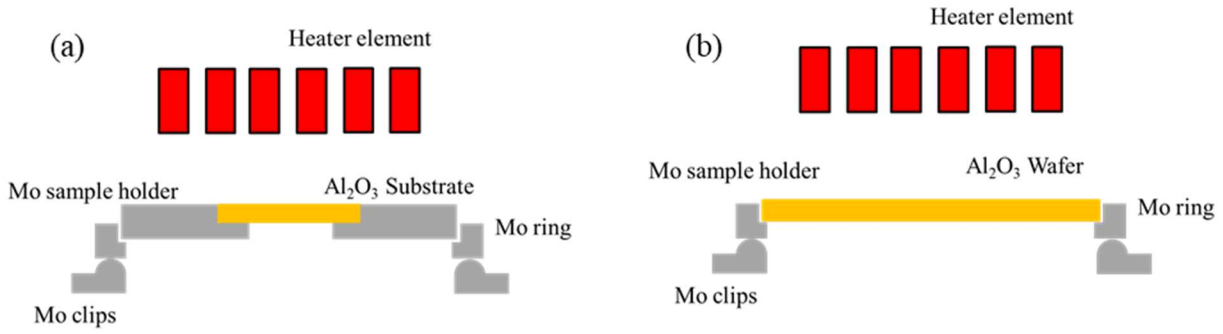

Figure 6-14: Heater configuration for (a) 10x10 mm samples, which sit inside of a Mo sample holder, and (b) 2" wafer, which is held directly by the outer ring.

Where the Mo plate reflected some of the heater radiation back into the heater body, the Al_2O_3 wafer is fully transparent to infrared radiation. T_p is lower at a given applied voltage to the heater in the wafer configuration than in the 10x10 mm configuration because of this difference in the thermal environment. Figure 6-15 plots the heater voltage against the T_p and T_{Mo} for the two configurations without any film present, showing that the T_p for the 2" wafer configuration is consistently lower than in the 10x10 configuration.

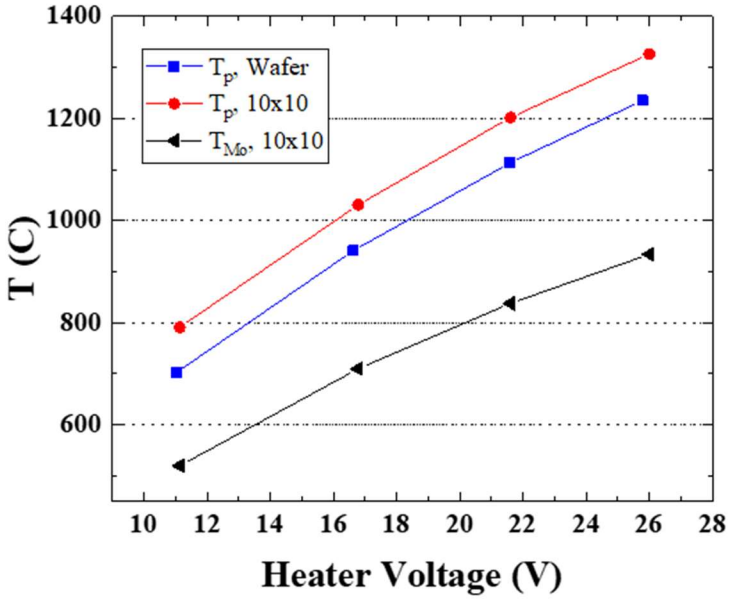

Figure 6-15: Temperature readings for various applied heater voltages in the wafer and Mo plate environments.

There is no place to insert the thermocouple, making it necessary to rely on T_p exclusively to control the growth temperature. The growth temperature of the wafer growth was determined by matching the T_p at the beginning of a wafer growth to that of a 10x10 mm growth. T_p was set to 1200 ˚C at the beginning of wafer growth, consistent with the starting temperature of most samples with T_{Mo} = 870 °C. The evolution of T_p for a wafer with film growth at r_{Sn} = 1.5 Å/s is shown in Figure 6-16, with the growth of a 10x10 mm sample for reference. The curves cross somewhere between 150-180 seconds into the growth, and T_p at the end is much higher for the wafer than for the 10x10 mm sample. At some point during film growth, the film reflects enough radiation into the heater to approximate the heater environment created by the Mo plate. This is accompanied by a higher heater voltage than that delivered for the 10x10 growths, resulting in the higher ending T_p of 930 °C.

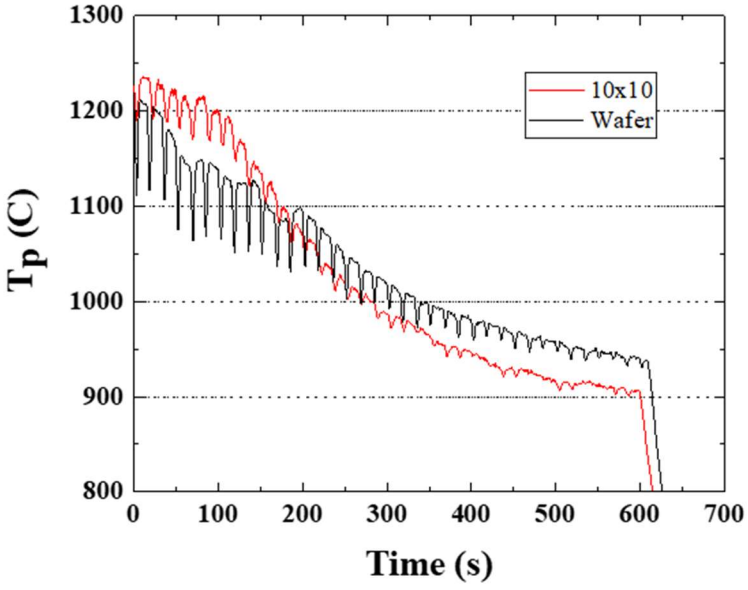

Figure 6-16: Evolution of T_p during growth for a 10x10 sample with T_{Mo} control (red) and a 2" wafer with no PID control (black). The growing film on the wafer reflects heat into the heater, raising the ending temperature.

This growth condition was maintained in the following films, in part to ensure that a high growth temperature was achieved over the entire wafer area. The heater element is only slightly larger than the wafer, making it somewhat difficult to deliver the full heater flux to the edges of the wafer (Figure 6-17). In films grown at lower starting T_p, the edges of the film are whitish in color and less reflective, likely due to high roughness from excess Sn failing to evaporate completely. Wafers grown at higher T_p, which does not have the gradient in reflectivity across the film.

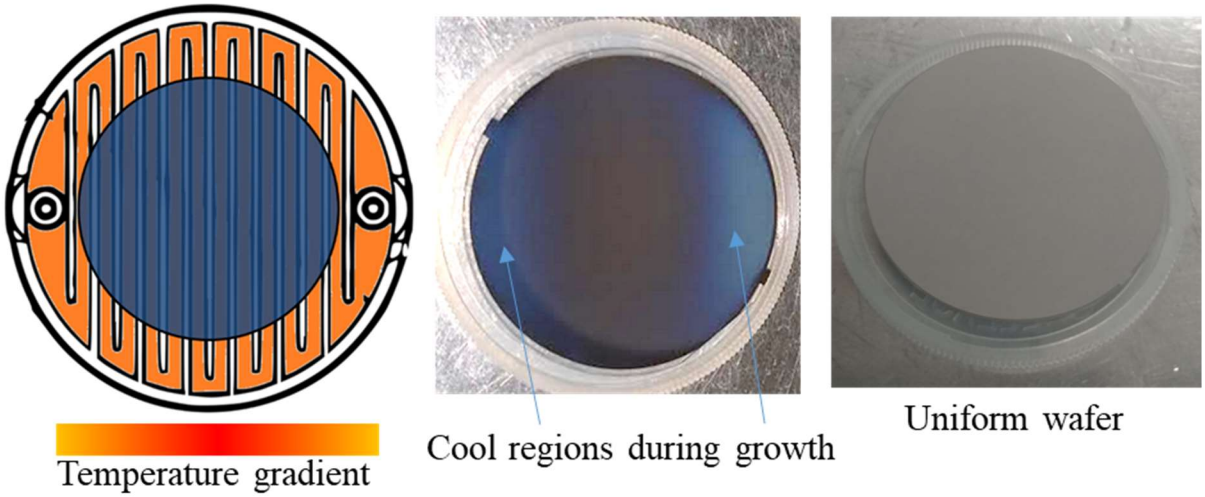

Figure 6-17: Position of 2" wafer with respect to SiC heater element. Element is coldest near the contacts, leading to inhomogeneous distribution of temperature across the wafer. When temperature is too low, Sn accumulates near the edges. At higher growth temperatures, wafer appears homogeneous (right).

Figure 6-18 shows the T_p reading for a wafer-scale SISIS sample growth. The behavior of the first Nb_3Sn layer closely follows that of the one in Figure 6-16, with an ending T_p of 940 °C. Al_2O_3 layers are grown at lower temperatures, and the sample is re-heated using the voltage at which the first layer was grown. This brings T_p back to 940 °C for S2 and S3 films, where the previous growth ended. Sputtering Nb and Sn again raises T_p to ~950 °C, where it peaks and gradually drops to 925 ˚C. The ending T_p of S2 and S3 is lower than that of S1 due to the thickness of the S1 layer (60 nm) being slightly smaller than the critical thickness at which the film becomes fully opaque.

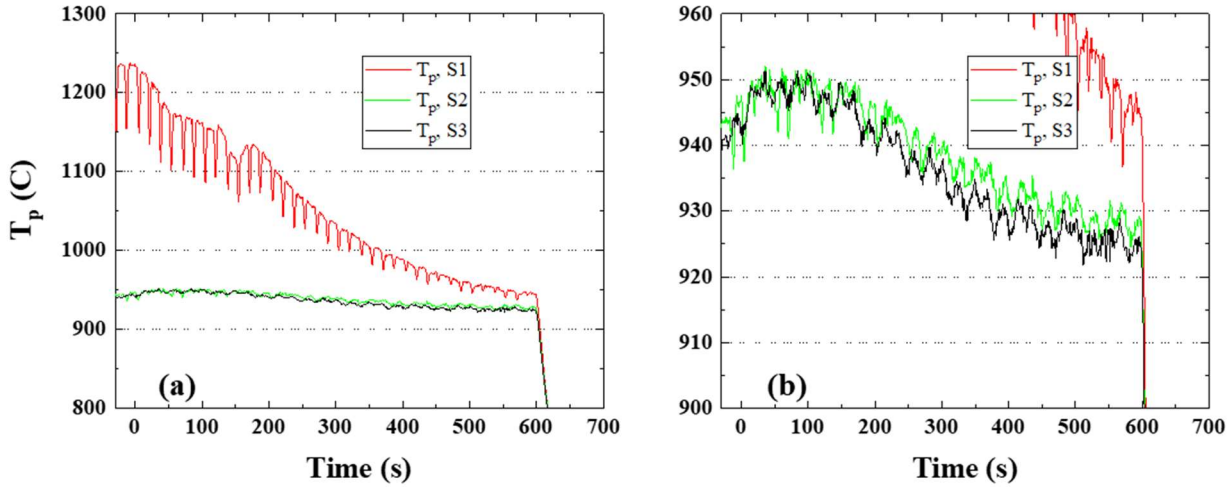

Figure 6-18: T_p evolution with the growth of each S layer. S1 follows the behavior of previous films. (b) S2 and S3 exhibit the behavior seen in the previous SISIS sample, in which Tp increased during growth on I layers.

Lastly, the back side of each wafer is coated with ~200 nm Nb, several times the penetration depth of Nb (λ_{Nb} = 40 nm). The final structure is shown in Figure 6-19. The Nb_3Sn layer is typically only 1~3 λ_{Nb3Sn} thick, resulting in some stray magnetic field propagation through the wafer. The Nb layer screens out this remaining field, preventing it from causing parasitic losses in the characterization chamber.

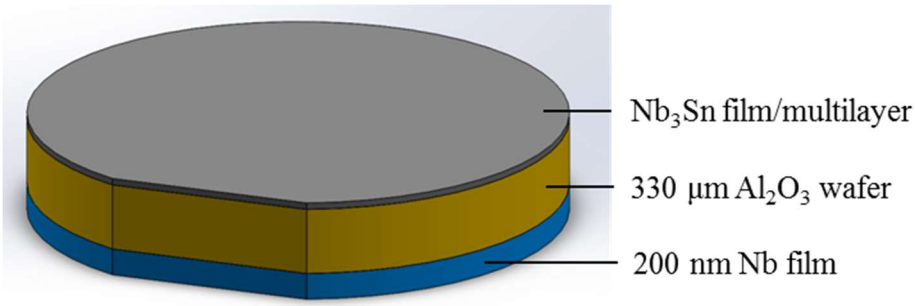

Figure 6-19: Schematic of wafer sample geometry for RF cavity measurements. The top layer is either Nb_3Sn or a SIS multilayer. Thick Nb on the back prevents stray fields from causing dissipation in the cavity.

6.6 DC Characterization of wafer cutouts

A 60-nm thick film was grown and diced for comparison to 10x10 mm samples. Sections of this wafer from the center and edges were cut out, as shown in Figure 6-20. Cutout 2, from the edge nearest the current lead, is where the growth temperature is expected to be lowest. T_c is not significantly different far from the center (17.2 vs 17.07 K), although the transition width seems to be affected (0.13 K at the center vs. 0.58 K at the edge); there is a variation in sheet resistance, which may be due to film thickness variation (film is thinner at the edges). RRR ranges from 3.23 to 3.71 over the three cutouts, confirming that the quality of the film does not vary significantly over the wafer area.

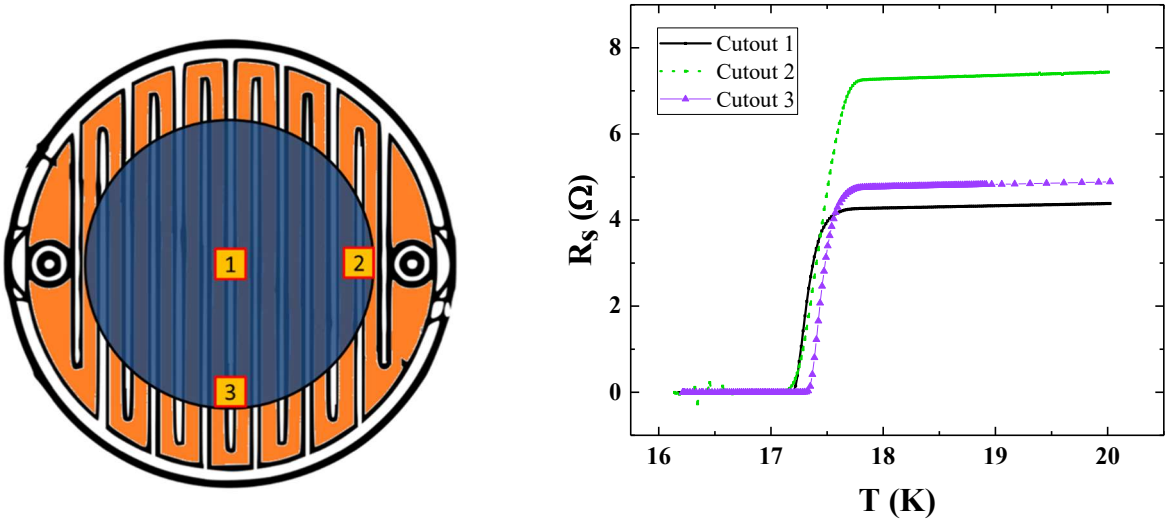

Figure 6-20: Superconducting transitions of pieces cut from a 2" wafer. Variation in T_c is <2%.

Interestingly, T_c at the edge in Cutout 3 was *higher* than the center (Cutout 1) by ~0.1 K. All regions at the edge of the wafer should receive equal Sn flux, since the heater rotates at a rate of ~2 rpm, which means this cutout is only differentiated from Cutout 2 by the heater flux it received. The combination of heater flux, Nb/Sn ratio, and total growth rate at Cutout 3 seems to

be optimal for producing higher T_c in these films, though the small variations in superconducting parameters should have minimal effect on the RF properties of the wafer.

6.7 RF characterization of wafers

These wafers were characterized by Paul Welander in a hemispherical RF cavity designed for this purpose at SLAC National Accelerator Laboratory [60,61]. A rendering of this cavity is shown in Figure 6-21. The cavity operates in a TE_{032}-like mode at 11.4 GHz, with a space on the surface to mount the 2" wafers. The overall cavity quality factor is measured, and the properties of the wafer can be extracted. The geometry of the cavity is engineered such that the magnetic field is strongest at the sample surface, limiting the contribution of the cavity material to the overall cavity loss. According to simulations, the participation factor is 0.33 for the wafer, and 0.67 for the cavity body. Crucially, magnetic field at the sample is parallel and radial to the sample surface, making it possible to measure RF properties of the sample without interference from the perpendicular component of the field.

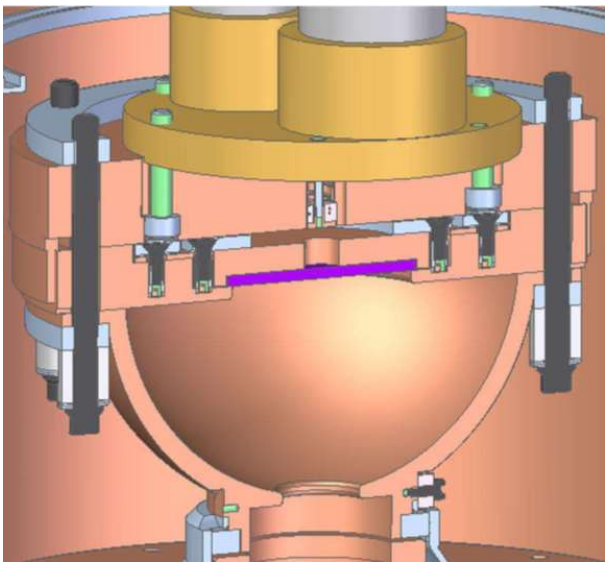

Figure 6-21: A rendering of the hemispherical cavity used at SLAC for surface resistance characterization. Wafer sample is depicted in purple. Reproduced from [60].

The facility has access to two hemispherical cavities. One is made of Cu and coated in a thick layer of Nb, which can measure fine details in Q_0 and R_s at low field. The other is made of bare Cu and can measure the properties of the sample at much higher fields. The Cu cavity does not have a critical magnetic field, making it possible to measure the quench field of the sample at fields higher than H_{quench} of Nb. Initially, two wafer samples were measured in the Nb cavity system: a 120-nm Nb_3Sn film, and a 5-layer SISIS multilayer with 60 nm Nb_3Sn and 6 nm Al_2O_3 layers. The Q_0 of these wafers at low RF power is plotted along with the Q_0 of a bulk Nb wafer in Figure 6-22.

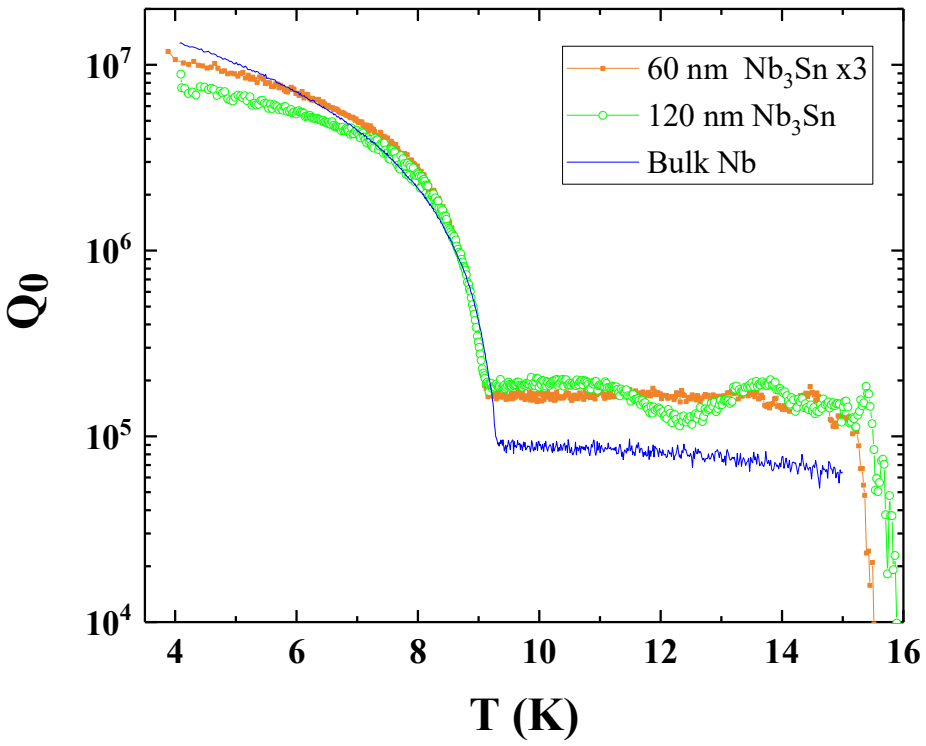

Figure 6-22: Q_0 vs. T for Nb_3Sn on Al_2O_3 wafers, compared against a bulk Nb sample. Measurements were conducted at low RF power.

At temperatures between 9 and 15 K, Q_0 of the Nb_3Sn wafers is higher than that of the Nb bulk coupon. This indicates that the surface of the wafer is superconducting and has a lower R_s

than the rest of the cavity. Above 15 K, Nb_3Sn is no longer superconducting and Q_0 drops off significantly.

Between 4 and 9 K, where the Nb cavity is in the superconducting state, Q_0 climbs dramatically with cooling. At 4 K, bulk Nb has the higher Q_0, followed closely by the SISIS multilayer, then finally by the 120 nm thick Nb_3Sn film. The high Q_0 of the multilayer is a strong indicator that the Al_2O_3 layers contribute minimally to RF losses. This is in spite of the Al_2O_3 layer being only 60 nm from the surface in the multilayer, where the single-layer film is 120 nm of uninterrupted superconductor.

The difference in Q_0 at 4 K in the Nb_3Sn wafers is possibly due to the total film thickness. At 120-180 nm of total Nb_3Sn, these films are only 1-2 λ_{Nb3Sn} thick, and cannot completely screen out the magnetic fields. Higher losses in the thinner film, in this scenario, come from the magnetic fields causing dissipation in the Al_2O_3 wafer or the Nb backing. The multilayer has a higher total thickness of Nb_3Sn, allowing slightly less RF magnetic field to leak into the wafer.

Two more films were grown to test for RF losses in the substrates. These films both have identical total Nb_3Sn thickness of 500 nm, which is 4-5 λ_{Nb3Sn}, allowing less field (~2%) to reach the substrate. One is grown in a single layer, and the other is split into four layers with 125 nm thickness each, separated by 6 nm Al_2O_3 layers. If Al_2O_3 layers contribute minimally to R_s of these films, they should have identical Q_0 behavior under low-power RF measurements, and should have higher Q_0 than the thinner films measured in the first round. Once this is confirmed, they can be measured in the Cu cavity at high power, and H_{quench} of each film can be measured.

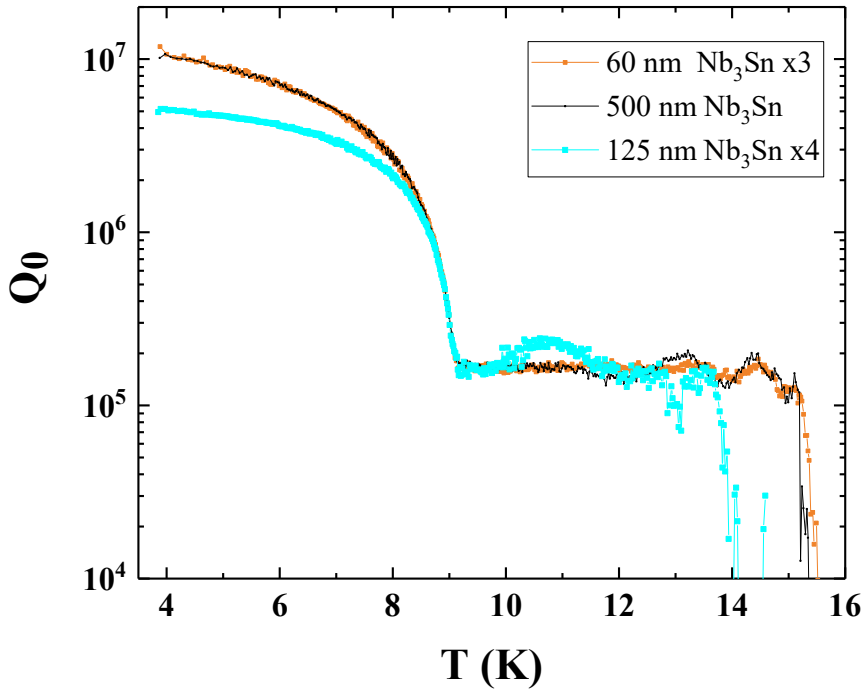

Figure 6-23: Q_0 vs. T for thick Nb_3Sn and equivalent-thickness multilayer, with previous 60 nm Nb_3Sn x3 sample for comparison.

The results of this measurement are presented in Figure 6-23. The 500-nm film behaves nearly identically to the thin multilayer, differing only in the region between 9-15 K. Q_0 at 4 K is still below the 1.3×10^7 value achieved by the bulk Nb. This strongly suggests that the substrate is not the limiting factor in these samples, and that the ceiling in the Q_0 is intrinsic to these films. This could result from the compositional inhomogeneity verified in TEM EDS measurements, or the oxide layer that forms on the topmost film. Some changes to the growth process will need to be made to improve Q_0 of Nb_3Sn to its predicted performance.

The multilayer with equivalent thickness had a dramatically lower Q_0 at 4 K than the rest of the samples, as well as the lowest T_c at ~14 K. This was not expected, and could result from lower growth temperatures. The T_p of these last two samples are plotted in Figure 6-24. T_p of the thick multilayer is ~900 °C at the end of the growth, which is considerably lower than the 500 nm

film (915 °C) or the thinner films. This strongly suggests that the R_s of the films depends strongly on growth temperature, and that tighter control of growth temperature for wafers is necessary.

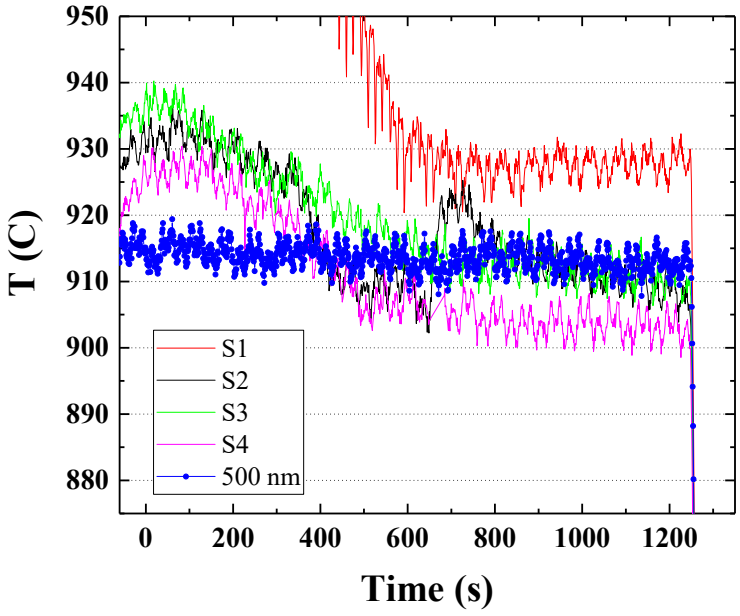

Figure 6-24: T_p of multilayer growth S1-S4, compared with 500 nm film growth. S4 layer ending Tp is considerably lower than the rest.

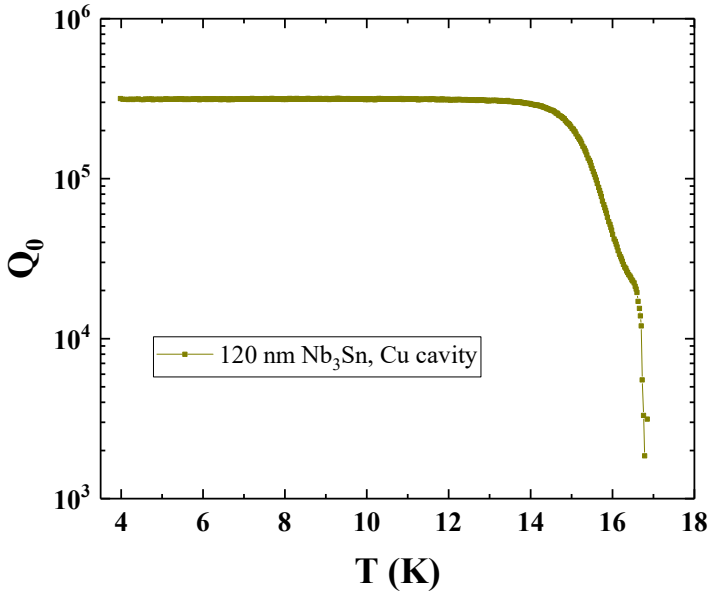

Figure 6-25: Low-power quality factor of 120 nm Nb_3Sn film measured in Cu cavity. Low-T Q_0 is limited by the Cu cavity. The differential in Q between normal and superconducting Nb_3Sn is stark, a promising indication that quench fields will be very clear in high-field measurements.

The Q_0 of the 120-nm Nb_3Sn film was also measured in the Cu cavity at low fields. The result is plotted in Figure 6-25. Q_0 saturates below ~13 K, where the Cu cavity dominates RF losses. At ~16.5 K, there is a hump in the Q_0 as the film transitions from normal to superconducting. This indicates some inhomogeneity in the film, which is to be expected when there are Nb grains coexisting with Nb_3Sn in the film. The most important feature of this measurement is the strong dependence of Q_0 on the surface resistance of the Nb_3Sn. Above T_c of Nb_3Sn, Q_0 drops by a factor of ~100. These preliminary data assure that the transition of the film from superconducting to normal during high-field quench experiments will be very clear.

CHAPTER 7

Conclusions and Outlook

The conclusions of this project are summarized in three parts: (1) the successful growth of high-T_c thin films of Nb_3Sn with strong texture, (2) the preparation of Nb_3Sn/Al_2O_3 multilayer heterostructures at 10x10 and 2" wafer scales, and (3) measurement of the relevant RF properties of these films and heterostructures. Future directions for each part are explored, as is the possibility of using the same growth technique for similar materials systems with interesting properties.

7.1 Growth of high-T_c, highly textured Nb_3Sn films

The first challenge of this project was producing consistent and high-quality Nb_3Sn films. The best way to control film stoichiometry (3:1) while maintaining high growth temperature (above 930 ˚C) was found to be co-sputtering of Nb and Sn onto radiatively heated substrates. A pyrometer and a thermocouple were both utilized in monitoring and maintaining consistency in growth temperature across samples.

Sn sputter rate (r_{Sn}) was varied while co-sputtering with a fixed Nb sputter rate, and superconducting properties of the films were found to be insensitive to Sn flux above r_{Sn} = 1.0 Å/s with r_{Nb} = 0.7 Å/s, as summarized in Figure 7-1. The film growth is self-regulating, as excess Sn vaporizes from the surface of the growth at higher rates than it is provided.

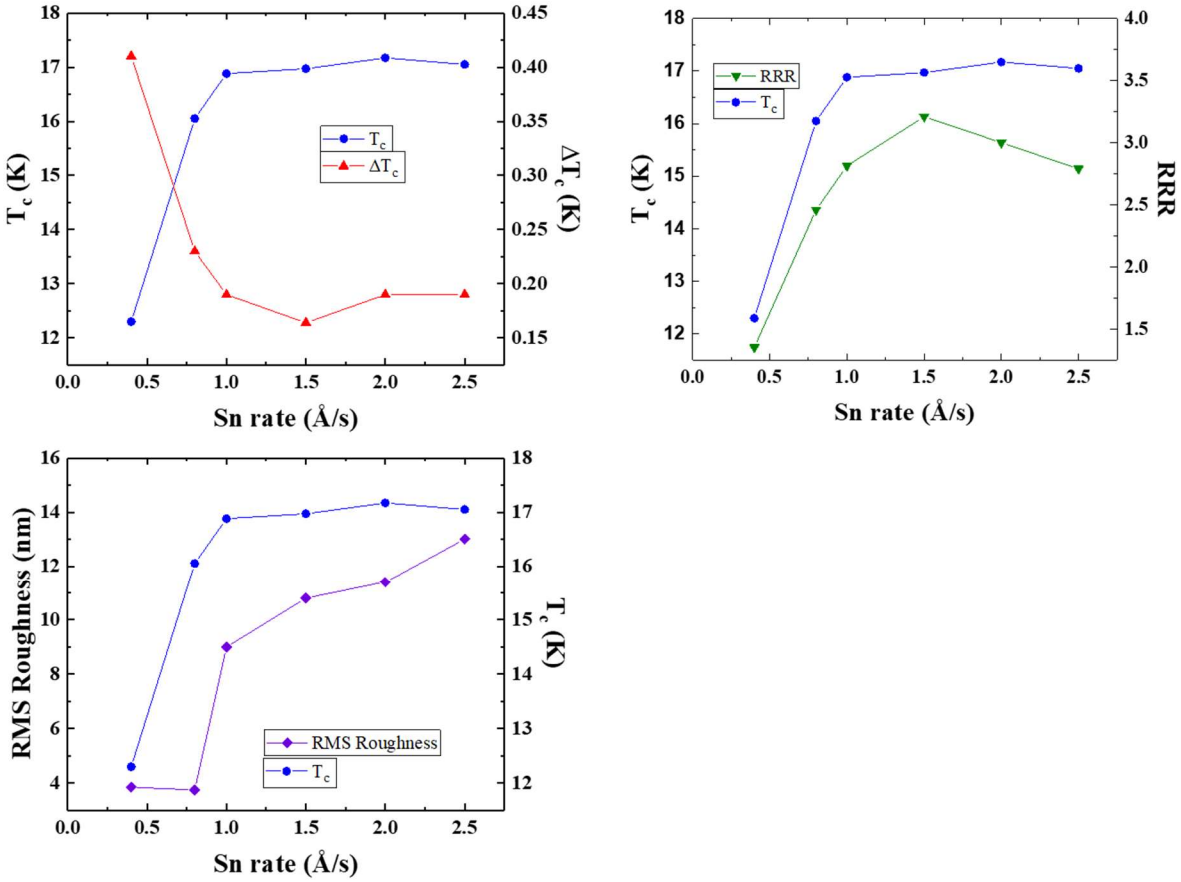

Figure 7-1: Dependence of T_c, ΔT_c, RRR, and film roughness with Sn flux. Above 1.0 Å/s, many properties saturate.

The RRR, sensitive to defects in the normal metallic state, peaked at r_{Sn} = 1.5 Å/s. Though excess Sn can evaporate freely during growth, impurities in the Sn flux may not have such high vapor pressures. This leaves an ever-increasing number of non-Sn impurities in the film at higher r_{Sn}, leading to the peak in RRR.

These films were studied using THz spectroscopy and STM. THz measurements at equilibrium conditions showed that the scattering rate of quasiparticles is somewhat low compared to other films that have been measured this way, which points to desirable RF properties. STM measurements showed a superconducting gap shape that includes a continuum of states inside the gap that can contribute to residual surface resistance. However, the contribution to R_s from these

states was calculated to be lower than what is actually measured in currently available Nb cavities, pointing again to the suitability of Nb_3Sn for SRF applications.

Growing single-crystal films of Nb_3Sn still proves elusive. A number of materials and orientations were used as substrates for these films. Growth on A- and R-plane Al_2O_3 reduces the number of orientations in polycrystalline films to 2, but without some mechanism to make one of these orientations more energetically favorable during the nucleation phase of film growth, it is difficult to move to a single-orientation film. Growth on cubic substrates, such as $LaAlO_3$, encouraged growth of epitaxial (001)-oriented grains, but other orientations were also present. The intended application of these films is in polycrystalline Nb cavities, and as such the crystalline quality of the films is secondary to the superconducting properties. However, growth of single-crystal Nb_3Sn films would make a novel form of the material available for study, making it possible to study the intrinsic properties without the effects of grain boundaries and complex angles at the interfaces of films. Growth of single-crystal films seem within reach with the appropriate selection of a cubic substrate and tuning of growth conditions.

7.2 Growing multilayer Nb_3Sn/Al_2O_3 heterostructures

The second challenge was to grow $Nb_3Sn/Al_2O_3/Nb_3Sn$ multilayers. In the initial phase of optimizing the conditions for these multilayers, it was found that a short period of annealing is beneficial for the Nb_3Sn films, raising T_c by ~0.2 K and increasing RRR from 3.2 to 4.3, an increase of over 30%, indicating some defects are present in the as-grown films that can be removed by thermal treatment.

Given the low dimensions of the Al_2O_3 films (~5 nm), it was difficult to determine their morphology (or even the presence) on the very rough Nb_3Sn films. AFM images and electrical

conductivity measurements both pointed toward the Al_2O_3 layer being absent. TEM images were required to clarify the situation.

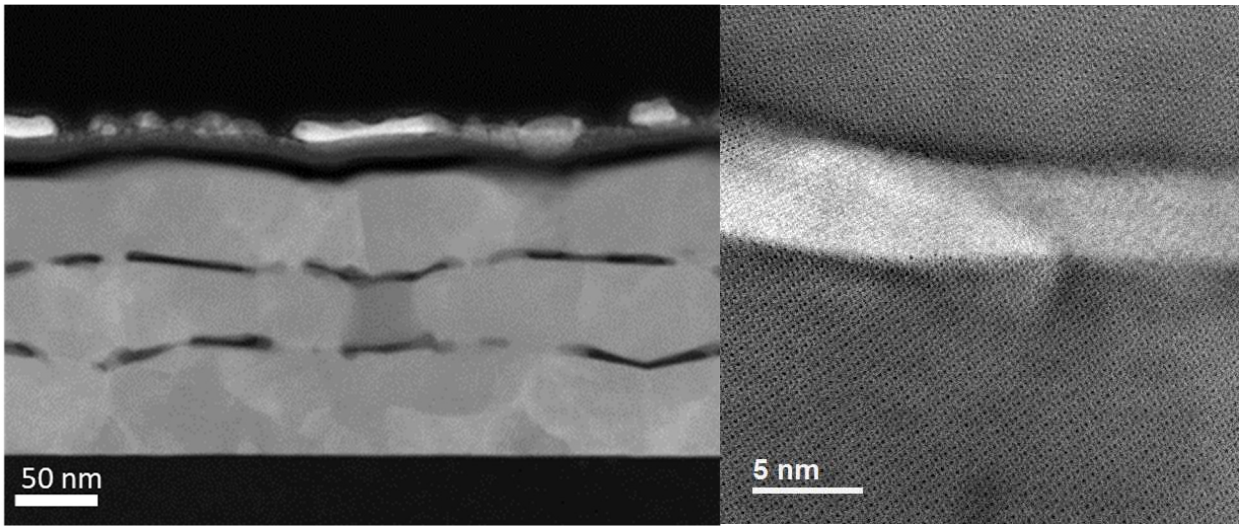

Figure 7-2: TEM images confirmed the presence of Al_2O_3 layers in the films, though they are discontinuous. Epitaxial relationships between the S1 and S2 layer can be preserved across the insulating layer.

These confirm that Al_2O_3 films are present, but discontinuous across the film area (Figure 7-2). Despite exposure to high temperatures during the growth of Nb_3Sn layers, these layers do not dissolve into the surrounding metallic film and maintain their shape over multiple heating cycles. Images show that, in some areas, Nb_3Sn orientation below and above the Al_2O_3 layer is identical, indicating that epitaxy across both interfaces is possible.

The holes in the Al_2O_3 film are a concern, and may require some attention. Within the sample region provided by TEM measurements, gaps in the Al_2O_3 layer are on the order of λ_{Nb3Sn} ~100 nm or smaller. The question remains as to whether this sufficiently separates Nb_3Sn layers from one another to prevent vortex nucleation at high RF fields. A possible research direction is in developing methods to control the morphology of these layers, as the morphology of the Al_2O_3 layer in coated Nb cavities may end up being discontinuous. Having the ability to predict the

effects of the morphology on high-field RF properties could be a powerful tool in later stages of research.

7.3 RF measurements

RF measurements in the cavity geometry were conducted at low RF fields on wafers of Nb_3Sn and SIS multilayers (Figure 7-3). The results of these measurements are encouraging, showing that the Nb_3Sn has very low R_s, and compares well to a bulk Nb sample measured in the same cavity. The SIS multilayer sample had a higher Q_0 than the single-layer film, confirming that the Al_2O_3 layer contributes very little to loss. This is in spite of being grown in an oxygen-free atmosphere, which could lead to a nonstoichiometric film with lossy defects. Interfaces between Nb_3Sn and Al_2O_3 do not lead to undesirable phases from intermixing.

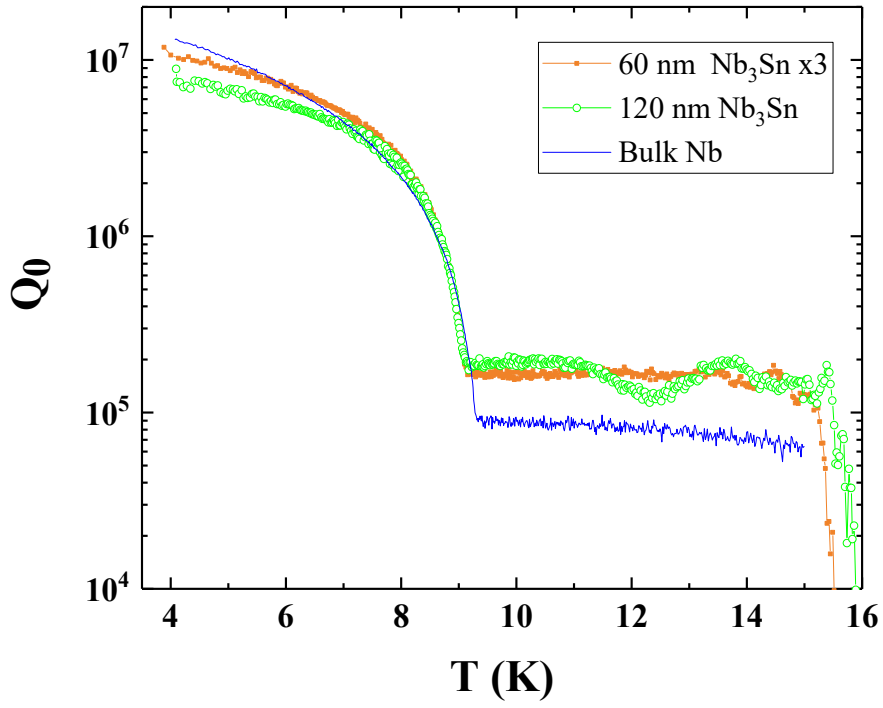

Figure 7-3: Quality factor of bulk Nb compared to bare Nb_3Sn and a 5-layer SIS multilayer.

The next step is to measure these samples at high RF fields. The copper RF cavity at SLAC has the capacity to measure at high magnetic fields. By measuring Q_0 at increasingly high fields, it is possible to measure the quench field at which flux penetration occurs and Q_0 drops sharply. These measurements are the key to the next stage of the project. If multilayer samples have significantly higher B_{quench} than the single-layer samples, there are a number of parameters that can be tuned to investigate this dependence. The effect of Al_2O_3 continuity across the wafer area is an open question. The effect of the film orientation, roughness, and grain size are not studied in the bare Nb_3Sn films. The hypothesis that the superheating field of Nb_3Sn can be exceeded in a $Nb/Al_2O_3/Nb_3Sn$ structure can be tested as well.

7.4 Application of High-Temperature Co-Sputtering to other systems

The Nb-Sn system has a very large growth window at high temperatures that results in stoichiometric Nb_3Sn films. This was due to the Nb_3Sn + Sn(*l*) phase region at high temperatures. There are other materials systems that are interesting which meet the same criteria as the Nb-Sn system, in which a stoichiometric single-phase region is bordered by a two-phase region in which the second phase has a very high vapor pressure.

The superconductors Ta_3Sn and Ta_3Pb meet these criteria; Ta is a refractory metal with a very high melting point, and Sn and Pb are metals with very high vapor pressures in their pure phases. Ta-Sn phase diagrams are readily available (Figure 7-4), showing that Ta_3Sn is bordered by the required two-phase region. Ta-Pb is far less studied [62], and no such phase diagram is available.

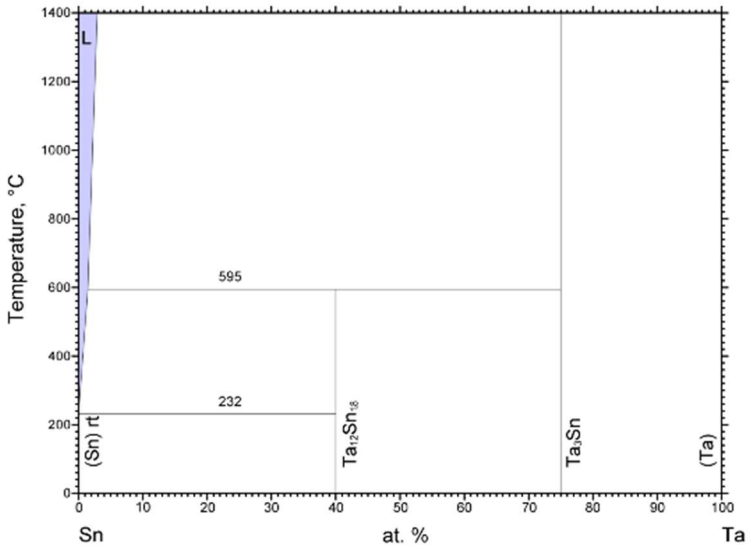

Figure 7-4: Ta-Sn phase diagram, showing a Ta_3Sn line compound bordered by a 2-phase region of Ta_3Sn and liquid Sn on the Sn-rich side. [63]

These are interesting materials, as the strong spin-orbit coupling in Ta is theorized to give rise to nontrivial band topology in the bulk band structure, leading to topological surface states near the Fermi energy [64]. If this is true, the proximity effect from the bulk superconductivity should induce topological superconductivity. This makes them promising candidates for the realization of topological superconductivity and observation of Majorana fermions.

CHAPTER 8

References

1. Weinstock, H. & Nisenoff, M. *Microwave superconductivity*. (Springer Science & Business Media, 2012).

2. Padamsee, H. *RF superconductivity: science, technology, and applications*. (John Wiley & Sons, 2009).

3. Guo, J. *et al.* Cryogenic RF Material Testing with a High-Q Copper Cavity. in *Advanced Accelerator Concepts: 14th Workshop* **330,** 330–335 (2010).

4. Cahill, A. D. *et al.* Rf Losses in a High Gradient Cryogenic Copper Cavity. *Phys. Rev. Accel. Beams* **21,** 061301 (2018).

5. Onnes, H. K. Further experiments with liquid helium. G. On the electrical resistance of pure metals, etc. VI on the sudden change in the rate at which the resistance of mercury disappears. *KNAW, Proc.* **14,** 818–821 (1912).

6. Tinkham, M. *Introduction to superconductivity*. (Courier Corporation, 2004).

7. Eisenmenger, W. *Nonequilibrium Superconductivity, Phonons, and Kapitza Boundaries*. (Plenum, New York, 1981).

8. Bardeen, J. Two-Fluid Model of Superconductivity. *Phys. Rev. Lett.* **1,** 399–400 (1958).

9. Turneaure, J. P. & Weissman, I. Microwave surface resistance of superconducting niobium. *J. Appl. Phys.* **39,** 4417–4427 (1968).

10. Bean, C. P. & Livingston, J. D. Surface Barrier in Type-II Superconductors. *Phys. Rev.*

Lett. **12,** 4–6 (1964).

11. Transtrum, M. K., Catelani, G. & Sethna, J. P. Superheating field of superconductors within Ginzburg-Landau theory. *Phys. Rev. B - Condens. Matter Mater. Phys.* **83,** 1–8 (2011).

12. Kittel, C. & others. *Introduction to solid state physics*. (Wiley New York, 2004).

13. Dhakal, P. *et al.* Effect of high temperature heat treatments on the quality factor of a large-grain superconducting radio-frequency niobium cavity. *Phys. Rev. ST Accel. Beams* **16,** 042001 (2013).

14. Grassellino, a *et al.* Nitrogen and argon doping of niobium for superconducting radio frequency cavities: a pathway to highly efficient accelerating structures. *Supercond. Sci. Technol.* **26,** 102001 (2013).

15. Ciovati, G., Dhakal, P. & Gurevich, A. the microwave field decrease of the surface resistance in superconducting niobium resonator cavities by the microwave field. *Appl. Phys. Lett.* **104,** 092601 (2014).

16. Romanenko, A., Grassellino, A., Crawford, A. C., Sergatskov, D. A. & Melnychuk, O. Ultra-high quality factors in superconducting niobium cavities in ambient magnetic fields up to 190 mG. *Appl. Phys. Lett.* **105,** 234103 (2014).

17. Sears, J. *et al.* Nitrogen-doped 9-cell cavity performance in a test cryomodule for LCLS-II. *J. Appl. Phys.* **117,** 023908 (2015).

18. Gurevich, a. Enhancement of rf breakdown field of superconductors by multilayer coating. *Appl. Phys. Lett.* **88,** 012511 (2006).

19. Abrikosov, A. A. On the lower critical field of thin layers of superconductors of the second group. *J. Exptl. Theor. Phys.* **19,** 988–991 (1964).

20. Posen, S., Catelani, G. & Liepe, M. Theoretical field limits for multi-layer superconductors. in *Proceedings of SRF2013* 794–799 (2013).

21. Gurevich, A. Maximum screening fields of superconducting multilayer structures. *AIP Adv.* **5,** 017112 (2015).

22. Antoine, C. Z. *et al.* Characterization of Field Penetration in Superconducting Multilayers Samples. *IEEE Trans. Appl. Supercond.* **21,** 2601–2604 (2011).

23. Antoine, C. Z., Villegier, J. C. & Martinet, G. Study of nanometric superconducting multilayers for RF field screening applications. *Appl. Phys. Lett.* **102,** 102603 (2013).

24. Tajima, T. *et al.* Studies on thin film MgB2for applications to RF structures for particle accelerators. in *AIP Conference Proceedings* **1435,** 297–304 (2012).

25. Allen, L. H., Anklam, J., Beasley, M. R., Hammond, R. H. & Turneaure, J. P. RF Surface Resistance in Nb3Sn Thin Films. *IEEE Trans. Magn.* **21,** 525–527 (1985).

26. Allen, L.H., Beasley, M.R., Hammond, R.H., Turneaure, J.P. RF Surface Resistance of Nb3Sn, NbZr, and NbN Thin Films. *IEEE Trans. Magn.* **23,** 1405–1408 (1987).

27. Rudman, D. A., Hellman, F., Hammond, R. H. & Beasley, M. R. A15 NbSn tunnel junction fabrication and properties A 15 Nb-Sn tunnel junction fabrication and properties. *J. Appl. Phys.* **55,** 3544 (1984).

28. Andreone, A. *et al.* Nonlinear microwave properties of Nb3Sn sputtered superconducting films. *J. Appl. Phys.* **82,** 1736 (1997).

29. Wu, C. T., Kampwirth, R. T. & Hafstrom, J. W. High-rate magnetron sputtering of high T_c Nb_3Sn films. *J. Vac. Sci. Technol.* **14,** 134–137 (1977).

30. Andreone, A. Microwave measurements of superconducting Nb3Sn films by a microstrip resonator technique. *IEEE Trans. Appl. Supercond.* **7,** 1772–1775 (1997).

31. Vandenberg, J. M., Gurvitch, M., Hamm, R. A., Hong, M. & Rowell, J. M. New phase formation and superconductivity in reactively diffused Nb3Sn multilayer films. *IEEE Trans. Magn.* **21,** 819–822 (1985).

32. Rossi, a a *et al.* Nb3Sn films by multilayer sputtering. in *Proceedings of SRF2009* 149–154 (2009).

33. Godeke, A. A Review of the Properties of Nb3Sn and Their Variation with A15 Composition, Morphology and Strain State. *Supercond. Sci. Technol.* **19,** R68–R80 (2006).

34. Miyazaki, S. Photoemission study of energy-band alignments and gap-state density distributions for high-k gate dielectrics. *J. Vac. Sci. Technol. B Microelectron. Nanom. Struct.* **19,** 2212 (2001).

35. Maglić, K. D., Perovic, N. L., Vukovic, G. S. & Zekovic, L. P. Specific Heat and Electrical Resistivity of Niobium Measured by Subsecond Calorimetric Technique. *Int. J. Thermophys.* **15,** 963–972 (1994).

36. Wang, Q., Xiao, P., Yu, J. & Dai, J. Measuring normal spectral emissivities of niobium by a pulse-heating technique: 1000 K to the melting point. *Chiese Opt. Lett.* **04,** 701 (2006).

37. Gillet, M., Al Mohammad, a., Masek, K. & Gillet, E. Influence of surface structure on the

growth of Au on αAl2O3 (1̄012). *Thin Solid Films* **374,** 134–141 (2000).

38. Trainor, T. P., Eng, P. J., Brown, G. E., Robinson, I. K. & De Santis, M. Crystal truncation rod diffraction study of the α-Al2O3 (1 1̄ 0 2) surface. *Surf. Sci.* **496,** 238–250 (2002).

39. Godeke, A., Hellman, F., Kate, H. H. J. T. & Mentink, M. G. T. Fundamental origin of the large impact of strain on superconducting Nb3Sn. *Supercond. Sci. Technol.* **31,** 105011 (2018).

40. Devantay, H., Jorda, J. L., Decroux, M. & Muller, J. The physical and structural properties of superconducting A15-type Nb- Sn alloys. *J. Mater.* **16,** 2145–2153 (1981).

41. Flukiger, R., Kuepfer, H., Jorda, J. & Muller, J. Effect of atomic ordering and composition changes on the R of Nb3Al, Nb3Sn, Nb3Ge, Nb3Ir, V3Si and V3Ga. *IEEE Trans. Magn.* **MAG-23,** 1596–1599 (1987).

42. Gurevich, A. Theory of RF superconductivity for resonant cavities. *Supercond. Sci. Technol.* **30,** 034004 (2017).

43. Dynes, R. C., Narayanamurti, V. & Garno, J. P. Direct measurement of quasiparticle-lifetime broadening in a strong-coupled superconductor. *Phys. Rev. Lett.* **41,** 1509–1512 (1978).

44. Dynes, R. C., Garno, J. P., Hertel, G. B. & Orlando, T. P. Tunneling study of superconductivity near the metal-insulator transition. *Phys. Rev. Lett.* **53,** 2437–2440 (1984).

45. Visentin, B., Barthe, M. F., Moineau, V. & Desgardin, P. Involvement of hydrogen-

vacancy complexes in the baking effect of niobium cavities. *Phys. Rev. Spec. Top. - Accel. Beams* **13,** 1–7 (2010).

46. Proslier, T. *et al.* Tunneling study of cavity grade Nb: Possible magnetic scattering at the surface. *Appl. Phys. Lett.* **92,** 212505 (2008).

47. Proslier, T. *et al.* Tunneling study of SRF cavity-grade niobium. *IEEE Trans. Appl. Supercond.* **19,** 1404–1408 (2009).

48. Becker, C. *et al.* Analysis of Nb3Sn surface layers for superconducting radio frequency cavity applications. *Appl. Phys. Lett.* **106,** 1–5 (2015).

49. Hornibrook, J. M., Mitchell, E. E. & Reilly, D. J. Superconducting Resonators with Parasitic Electromagnetic Environments. *arXiv:1203.4442* (2012).

50. Matsunaga, R. & Shimano, R. Nonequilibrium BCS state dynamics induced by intense terahertz pulses in a superconducting NbN film. *Phys. Rev. Lett.* **109,** 2–6 (2012).

51. Kabanov, V. V., Demsar, J. & Mihailovic, D. Kinetics of a superconductor excited with a femtosecond optical pulse. *Phys. Rev. Lett.* **95,** 1–4 (2005).

52. Beck, M. *et al.* Energy-gap dynamics of superconducting NbN thin films studied by time-resolved terahertz spectroscopy. *Phys. Rev. Lett.* **107,** 19–22 (2011).

53. Rothwarf, A. & Taylor, B. N. Measurement of recombination lifetimes in superconductors. *Phys. Rev. Lett.* **19,** 27–30 (1967).

54. Dexheimer, S. L. *Terahertz spectroscopy: principles and applications*. (CRC press, 2007).

55. Yang, X. *et al.* Terahertz-light quantum tuning of a metastable emergent phase hidden by superconductivity. *Nat. Mater.* **17,** 586–591 (2018).

56. Bilbro, G. & McMillan, W. L. Theoretical model of superconductivity and the martensitic transformation in A15 compounds. *Phys. Rev. B* **14,** 1887–1892 (1976).

57. Posen, S. & Liepe, M. Stoichiometric Nb3Sn in First Samples Coated at Cornell. in *Proceedings of the Fifteenth Conference on RF Superconductivity* 886–889 (2011).

58. Posen, S. & Hall, D. L. Nb3Sn superconducting radiofrequency cavities: Fabrication, results, properties, and prospects. *Supercond. Sci. Technol.* **30,** 033004 (2017).

59. Sosa-Guitron, S., Gurevich, A., Delayen, J., Eremeev, G., Sundahl, C.S., Eom, C. B. Measurements of Rf Properties of Thin Film Nb 3 Sn Superconducting Multilayers Using a Calorimetric Technique. in *Proceedings of SRF2015* TUPB060 (2015).

60. Welander, P., Franzi, M. & Tantawi, S. Cryogenic RF characterization of superconducting materials at SLAC with hemispherical cavities. in *Proceedings of SRF2015* 735–738 (2015).

61. Ni, Z. *et al.* Fabrication and radio frequency test of large-area MgB2 films on niobium substrates. *Supercond. Sci. Technol.* **30,** 45009 (2017).

62. Teleushev, A. Z., Volodin, V. N., Teleushev, Y. Z. & Zhakanbaev, E. A. Synthesis and properties of the Ta3Pb compound. *Phys. Met. Metallogr.* **97,** 269–272 (2004).

63. Wang, J. L., Tuo, B. Y., Hu, X. P. & Liu, Z. L. Thermodynamic Properties and Thermodynamic Assessment of Ta-Sn System. *Adv. Mater. Res.* **821–822,** 849–853 (2013).

64. Kim, M., Wang, C.-Z. & Ho, K.-M. Topological states in A15 superconductors. *arXiv:1807.03405* (2018).